SPIRAL CORONARY ARTERY WALL IMAGING:

NEW METHODS AND APPLICATIONS

A DISSERTATION

PRESENTED TO

THE FACULTY OF THE SCHOOL OF ENGINEERING AND APPLIED SCIENCE

UNIVERSITY OF VIRGINIA

IN PARTIAL FULFILLMENT

OF THE REQUIREMENTS FOR THE DEGREE

DOCTOR OF PHILOSOPHY IN BIOMEDICAL ENGINEERING

by

MEIHAN WANG

August 2013

Spiral coronary artery wall imaging, new methods and applications

---

A Dissertation

Presented to
the faculty of the School of Engineering and Applied Science
University of Virginia

---

in partial fulfillment
of the requirements for the degree

Doctor of Philosophy

by

Meihan Wang

August

2013

APPROVAL SHEET

The dissertation
is submitted in partial fulfillment of the requirements
for the degree of
Doctor of Philosophy

AUTHOR

The dissertation has been read and approved by the examining committee:

Craig H. Meyer
Advisor

John A. Hossack

Frederick H. Epstein

John P. Mugler

Brent A. French

Accepted for the School of Engineering and Applied Science:

James H. Ayl

Dean, School of Engineering and Applied Science

August
2013

Abstract

Magnetic resonance imaging (MRI) provides a safe and noninvasive method for detecting and diagnosing coronary artery disease (CAD). It can detect atherosclerotic plaque by visualizing the coronary artery wall. Changes in artery wall thickness may indicate the presence of CAD. Two-dimensional (2D) single-slice magnetic resonance (MR) coronary artery wall imaging studies have shown the thickening and occlusion of coronary vessel walls using 1.5T scanners [1]. Three-dimensional (3D) MR coronary artery wall imaging is a very challenging problem, because the resolution must be high enough to visualize the vessel wall and the blood signal must be suppressed in the entire imaging volume. The acquisition time is long for 3D, and artifacts caused by respiratory motion during the scan also need to be minimized.

This dissertation describes research focused on the following three goals related to 3D MR coronary artery wall imaging: 1) To test and develop parallel imaging techniques that can be used to shorten the acquisition time to a breath-hold to avoid respiratory motion artifacts; 2) To develop a novel black blood technique and compare its performance to traditional methods; and 3) To develop a 3D pulse sequence with black blood preparation and parallel imaging and test its performance in coronary artery wall studies using a 3T MR scanner.

Parallel imaging is a powerful tool for accelerating MR image acquisition by using the spatial encoding inherent in an array of receiver coils. When using large coil arrays, traditional coil-by-coil parallel image reconstruction requires significant computation. In this dissertation research, we tested and improved the synthetic target technique, a new parallel imaging reconstruction algorithm that requires significantly less computation. It uses a single step in the image reconstruction to form an unaliased

composite image, rather than generating an unaliased image corresponding to each coil. Array compression and parallel computing were incorporated to further reduce the required computation time. Both phantom and in-vivo studies using a Cartesian k-space trajectory were conducted, and the results were compared with GRAPPA, a standard parallel imaging technique. The synthetic target method was shown to be able to correct aliasing for brain and cardiac images with an undersampling rate up four times (4X) with a small decrease in image quality. The method can achieve up to a 30-fold computation time reduction for 32 channel data compared to GRAPPA.

We extended the synthetic target technique to non-Cartesian k-space trajectories. We added spatial weighting (PILS) masks to the original synthetic target method for constant spiral trajectories and tested the performance with in-vivo cardiac data. For radial trajectories, a zero phase map was added as a constraint on the training process. The performance was tested with phantom data. We also tested SPIRiT, an iterative parallel reconstruction technique on radial trajectories. The improved synthetic target technique removes artifacts for both spiral and radial trajectories better than the original method. For radial trajectories, the image quality of the synthetic target results was inferior to the image quality using SPIRiT, which demonstrated that the performance of the method is dependent upon the k-space trajectory. Thus, we chose to use the SPIRiT technique for subsequent coronary wall imaging studies that used non-Cartesian trajectories, because for that application image quality is more important than computation time.

The signal from blood is typically suppressed in MR coronary artery wall imaging, which makes it easier to visualize the wall and measure its thickness. One established method for suppressing blood signal is the double inversion recovery (DIR) technique, which relies on blood flowing out of the imaged slice during the inversion time (TI).

However, the DIR technique often cannot suppress the blood signal throughout a thick slab imaged using a multi-slice or 3D readout. Moreover, at a field strength of 3T, the longitudinal relaxation time (T_1) of blood is lengthened and thus the required inversion time for DIR is lengthened to over 600 ms, leaving a limited period during the heartbeat for placement of the readout module. In this work, a novel black blood technique called DANTE was implemented for coronary artery wall imaging. This technique was recently developed for ungated carotid artery wall imaging, but to our knowledge this is the first use of the DANTE technique for black blood gated cardiac imaging. This method enhances the contrast between blood and tissue in the entire volume of interest with less than 300 ms preparation time. We tested its performance with a 2D multi-slice spiral GRE sequence and compared the images to images acquired using the DIR technique. Because of the shorter preparation time, DANTE sequences have more flexibility in the placement of the readout model and DANTE images have comparable signal-to-noise ratio (SNR) to DIR images and higher contrast-to-noise ratio (CNR).

Free-breathing studies are commonly been for 3D coronary artery wall imaging. However, even with respiratory gating and motion compensation, respiratory motion can still lead to image blur in MR coronary artery wall imaging, causing overestimation of the wall thickness. Breath-held scans typically have less motion blur than free breathing scans, but require an efficient pulse sequence for 3D scanning. We implemented DANTE preparation, a 3D spiral readout and parallel image reconstruction to achieve 3D coronary artery wall imaging at 3T with high contrast within a breath-hold, thus minimizing motion blur. The sequence used a dual-density spiral k-space trajectory to collect parallel imaging training data and SPIRiT combined with off-resonance correction for parallel image reconstruction. Volunteer studies of right coronary artery wall imaging showed that our results have higher CNR than DIR

images. They also have comparable SNR and CNR to 2D single-slice images, which indicates that parallel imaging does not cause image quality degradation. The breath-hold images have better contrast than navigator-gated results in normal volunteers, demonstrating that future coronary plaque imaging studies may benefit from 3D breath-held coronary wall imaging.

Acknowledgements

I feel fortunate to have the opportunity to study at the University of Virginia for the last five years. Many people here have generously offered support to my studies. First of all, I would like to thank my advisor, Dr. Craig Meyer, who directed my research with much patience and encouragement. From him I also learned how devoted and passionate a researcher could be to his career. I appreciate very much his valuable advice, attention to details and the incredible understanding of all my problems.

I would like to thank Dr. Chris Kramer, Dr. Fred Epstein, Dr. John Mugler and Dr. Michael Salerno for educating me with their important knowledge of MRI, especially the clinical view of MRI applications. I would also thank Dr. John Hossack and Dr. Brent French for serving on my committee and giving me valuable suggestions about my academic research.

I have received much help from my colleagues: Li Zhao, Samuel Fielden, Xue Feng, Ken Johnson, Peng Hu, Weitian Chen, Hao Tan, Chris Sica, Kun Qing, Xiao Chen, Bhairav Mehta, and Yang Yang. They have served as volunteers for most of my research and helped bring inspiring thoughts to solve my problems in research. Also, they have brought much joy to the lab. I really enjoyed working with them.

Finally, I would thank my husband and my parents for their everlasting love and support.

Table of Contents

Chapter 1

Introduction

Parallel MR imaging with multi-coil arrays is a powerful tool to accelerate the acquisition process [2]. With the aid of parallel imaging, the dataset can be subsampled during the scan, and the missing data is then reconstructed using coil sensitivity information, either explicitly [2] or implicitly through auto-calibration [3]. Auto-calibrated image reconstruction methods perform a coil-by-coil reconstruction, using fully sampled regions for training and unaliasing each coil image separately. These methods are robust and used for many different applications. However, the computational complexity and reconstruction time increases enormously when the coil array is large. The synthetic target method, a rapid non-iterative reconstruction technique, was first proposed by Chen et al in 2008 [4]. The method uses one unaliasing step for reconstructing the final image. We test the synthetic target method on both Cartesian and spiral datasets and compare it with other methods in this work.

Detection of atherosclerotic plaque in coronary arteries is crucial for diagnosing coronary artery disease. In comparison other imaging modalities, one advantage of MR coronary artery imaging is that it can assess the remodeling process of the coronary arteries by eliminating the blood signal in the lumen. The double inversion recovery (DIR) prepared, ECG triggered, 2D fast spin echo (FSE) sequence is the most widely used sequence in clinical studies [1]. However, when applied to a 3D study, the original DIR cannot sufficiently remove the large amount of blood signal, which makes distinguishing the coronary wall impossible. Also, the time needed to acquire high-resolution 3D data is usually too long for one breath-hold. Navigator gating is then applied to reduce respiratory artifacts, but these methods cannot fully eliminate motion blur, especially when the navigator efficiency is low.

DANTE is a newly published black blood imaging technique, which is especially suitable for suppressing blood in a large volume while achieving SNR comparable to that achieved with DIR [5]. In this dissertation we developed a gated cardiac DANTE method, tested it with 2D multi-slice and 3D readout modules, and compared its performance with DIR-prepared results.

Spiral k-space scanning [6] is a rapid and efficient method of acquiring high-resolution cardiac images. It has been proven to be accurate in clinical studies [7]. The newly proposed SPIRiT algorithm [8] makes the combination of spiral trajectories and parallel imaging possible. In this dissertation, we describe a breath-held, DANTE prepared, 3D dual-density spiral gradient-echo sequence with SPIRiT image reconstruction for generating high-resolution, high-contrast coronary artery wall images.

1.1 Specific Aims

The research described in this dissertation was focused on four specific aims described in the following paragraphs.

Specific Aim 1: Test and improve synthetic target image reconstruction for Cartesian parallel imaging

Specific Aim 1 is to test and improve a novel parallel reconstruction method called synthetic target reconstruction, which was first described by W. Chen et al. [4]. The goal of the synthetic target method is to reduce the computation time required for parallel image reconstruction, as compared to the conventional techniques SENSE [2] and GRAPPA [3]. It uses auto-calibration to avoid the need for coil sensitivity estimation. The unaliasing step is performed only once to avoid coil-by-coil calculation. Ideally, it can reduce the reconstruction time by roughly the number of coils. With the help of other methods such as array compression [9] and parallel computing, the computation time can be further decreased. We will test the algorithm on a variety of datasets and show that this method can successfully remove aliasing with much less computation time than GRAPPA.

Specific Aim 2: Improve synthetic target image reconstruction for non-Cartesian parallel imaging

The synthetic target method uses data from the center of k-space for calibration of the convolution kernel. It is based on the assumption that the sampling pattern is uniform across k-space. For constant-density spirals, the assumption roughly holds, and thus synthetic target will work. However, for radial and variable density spiral trajectories, the sampling density in the center and outer k-space varies significantly; as a result, synthetic target will fail to remove aliasing unless modifications of the algorithm are applied. We will test synthetic target image reconstruction on different types of non-Cartesian trajectories, and the results will be compared with other possible methods.

Specific Aim 3: Implement and test DANTE pre-pulses for 2D spiral coronary artery wall imaging

DANTE pre-pulses were first proposed for black blood carotid scans [5]. The DANTE method is especially suitable for thick-slab scans, where they can maintain SNR and CNR comparable to DIR [10] and motion-sensitized driven-equilibrium (MSDE) [11].

We will implement DANTE with a gated 2D multi-slice spiral sequence for coronary artery wall studies and test the performance for imaging the right coronary artery (RCA) wall and the left anterior descending artery (LAD) wall. DANTE and DIR preparation results will be analyzed and compared.

Specific Aim 4: Develop 3D spiral sequences with DANTE preparation, dual-density spiral trajectories and parallel imaging for breath-held coronary artery wall studies

Navigator-gated studies can be quite time consuming and the final result can still suffer from motion artifacts. The aim of this study is to accomplish the acquisition of a 3D dataset within the time of one breath-hold, so that respiratory motion can be reduced. We will use 32-channel coils for parallel imaging in the study and slightly more than 1/4 of a fully-sampled dataset will be collected. Thus, the scan time can be reduced to about 20s. DANTE preparation is implemented to suppress blood in 3D slab. We will show that the final image is free of aliasing and respiratory artifacts. The sequence will be tested on healthy volunteers.

1.2 Dissertation Overview

The remainder of the dissertation is organized as follows:

Chapter 2 first gives an introduction to coronary artery disease (CAD). The possible modalities for diagnosing CAD are then reviewed. We describe recent MR coronary artery imaging studies and related techniques such as black blood imaging.

Chapter 3 presents the concept of synthetic target parallel image reconstruction. We discuss the influence of the choice of target on the final image quality. Array compression is added to the original synthetic target algorithm. The resultant images and computation time are compared with GRAPPA. We also extend the original synthetic target to multi-target synthetic target in order to reach a balance between computation time and image quality.

Chapter 4 is the application of synthetic target reconstruction to spiral and radial trajectories. We improve synthetic target with a PILS window to further remove aliasing. Phase-constrained synthetic target is developed for radial trajectories. SPIRiT reconstruction results are provided for comparison.

Chapter 5 discusses the application of DANTE pre-pulses for coronary artery imaging. We explored the feasibility of gated DANTE imaging and the optimal parameter set by simulating the blood and tissue signal using the Bloch equations. Then, we conducted in-vivo experiments using a 2D multi-slice spiral sequence on a 3T scanner. RCA and LAD images were collected with DANTE and DIR preparation. SNR and CNR were calculated to evaluate the performance of DANTE.

Chapter 6 discusses breath-hold DANTE-prepared 3D coronary artery wall imaging. Dual-density spiral scanning and parallel imaging are used for acquisition. SPIRiT is used for image reconstruction. We compared our RCA results with 1) 2D single-slice DIR results and 2) navigator-gated 2D Cartesian GRE results to show that our method can generate high-resolution, high contrast images without losing SNR.

Chapter 7 is a summary of the dissertation. We also discuss possible extensions of this work.

Chapter 2

Background

2.1 Coronary Artery Disease

The coronary arteries arise from the root of the aorta. The two main branches are the left and right coronary artery, which start from left and right aortic sinus, respectively. They provide the supply of oxygen to the heart muscle, together with their branches. The left anterior descending artery, usually known as the LAD, and the right coronary artery, usually known as the RCA, are often studied in cardiac imaging. The LAD is responsible for a significant portion of the blood flow to the left ventricle. The rest of the blood flow to the left ventricle is provided by the RCA and the left circumflex artery (LCx). The RCA also supplies blood to the right ventricle.

The blood flow in the coronary arteries changes during the heart cycle. During systole the flow is cut off because of the opening of the aortic valve and the contraction of the left ventricle. After systole, the coronary flow steadily increases and reaches maximum during diastole. The movement of RCA and LAD is complex during the heart cycle. The RCA experiences about twice the in-plane displacement of the LAD. Also, the maximum velocity of RCA is higher than that of the LAD [12]. The highest velocity usually occurs in early diastole, while in mid-diastole the motion is minimized. Figure 2.1 shows in–plane displacement plots of the LAD and the RCA during one heart cycle.

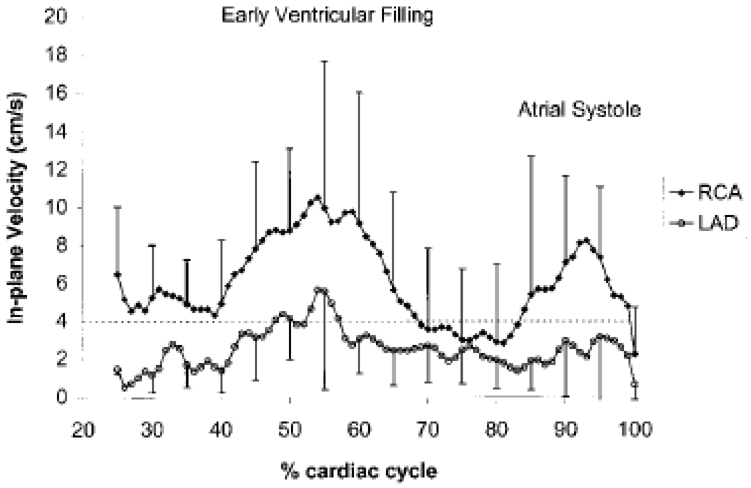

Fig. 2.1. Plots of the in-plane velocities of the RCA and LAD [13].

The accumulation of fatty lipids in the coronary artery wall is associated with atherosclerosis. The development of atherosclerosis and different types of lesions are shown in Fig. 2.2 [14]. During the first stages of atherosclerosis, a fatty steak formed by lipids, macrophages and smooth muscle cells gradually develops beneath the endothelium of the coronary artery wall. As the accumulation proceeds, the lesion can progress to types IV and Va. These two types of vulnerable plaques have a thin layer of cap over a core region, which is formed by smooth muscle cells and collagen-rich matrix [14]. They may experience rapid or intermediate progression. In the latter the plaques become fibrotic and stable; eventually they will cause stenosis and cut blood supply to heart muscle. Rapid progression is more dangerous. When the thin layer ruptures, the exposure of plaque components to the blood can result in thrombus, occlusion and sudden heart attack [14].

Coronary artery disease (CAD) caused by atherosclerosis is the most common cause of sudden death in the USA. In 2013, about 635,000 Americans will have a new coronary attack (defined as first hospitalized myocardial infarction or coronary heart disease death) and 280,000 will have a recurrent one [15]. In 2010, an estimated 954,000 inpatient percutaneous coronary intervention (PCI) procedures and 397,000 inpatient bypass procedures were performed in the United States to treat CAD. PCI serves as a major therapy for CAD. In the procedure, a catheter is placed down the coronary artery, with a small balloon at the tip of the wire. The balloon is later inflated to enlarge the narrowed vessel area. After that, a small metal mesh device called stent can be placed in the same area to prevent re-narrowing in future. Coronary artery bypass surgery is another possible treatment that increases the blood supply to the myocardium by providing a path for blood flow around coronary artery stenoses. Statin therapy is a commonly used medical treatment for CAD. Statins are a class of drugs that are inhibitors of HMG-CoA. HMG-CoA produces mevalonate, which is a precursor of cholesterol and also regulates immune activation [16]. In that way statins reduce the level of LDL cholesterol and C-reactive protein. These two markers have been shown to have a relationship with plaque progression [17]. Also statins increase the stability of plaques [18].

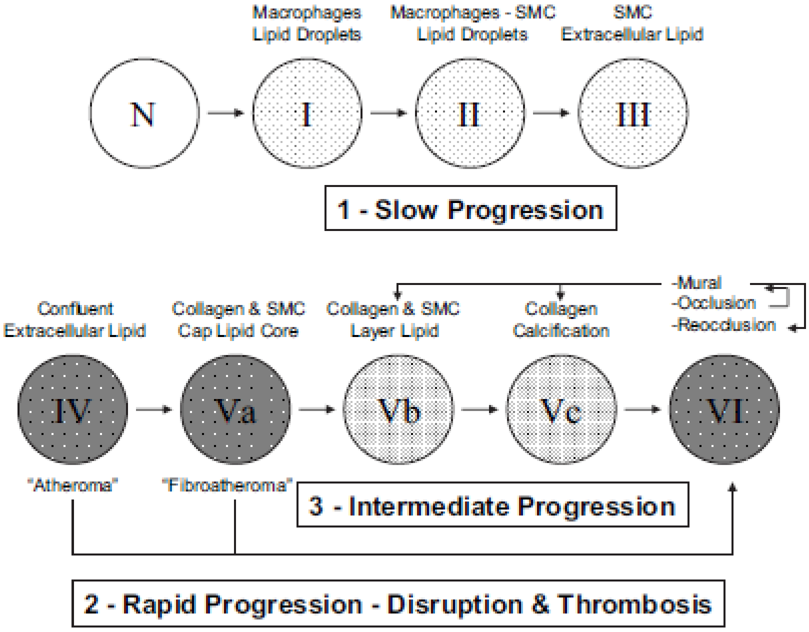

Fig. 2.2. Evolution of coronary artery disease [14].

2.2 Imaging Modalities for Coronary Artery Disease

X-ray angiography is the gold standard for diagnosing stenoses in coronary arteries, because of its ability to achieve high temporal and spatial resolution. It can also be used in a therapeutic procedure when combined with balloon dilatation and stenting. One disadvantage of x-ray angiography is that it is an invasive technique with associated morbidity and mortality. Another disadvantage is that it exposes patients and medical teams to ionizing radiation. As a result, it is not suitable for a screening procedure [14]. More, angiography is primarily useful when the patient is experiencing severe coronary stenosis. When the patient is in the first stages of the development of atherosclerosis and no obvious lumen narrowing is observed, CAD cannot be detected by X-ray angiography.

Intravascular ultrasound (IVUS) is another invasive imaging modality. It uses an ultrasound probe attached to the end of a catheter. By inserting the catheter in the coronary artery, it is possibly to obtain detailed images of atherosclerotic plaque. The advantage of IVUS over angiography is that it can visualize the remodeling process of CAD by assessing coronary artery wall thickness. IVUS is reported to be accurate in imaging plaque evolution [19] and has a higher sensitivity than angiography [20]. The disadvantage of IVUS is also the increased risk because of the invasive procedure.

Electron beam computed tomography (EBCT) and multi-slice computed tomography (MSCT) can image CAD non-invasively. They can detect calcium in the coronary arteries, and the resulting calcium score is associated with plaque burden [21]. EBCT is reported to have up to 95% sensitivity in defining calcium score [22]. However, calcium deposits are not predictive of stenosis [22]. Coronary CT angiography (CTA) is another promising method to image CAD. It can achieve a resolution as high as x-ray angiography. However，the radiation dose is much higher than conventional x-ray [23]. Cardiac motion is also a problem in CT angiography, especially for patients with fast heart rate, although recent scanner speed improvements have helped to address this issue. Extensive calcification in the coronary artery wall can reduce the accuracy of detecting stenosis [14]. Finally, coronary CTA is focused on imaging the lumen and not on remodeling of the vessel wall, although soft plaque imaging using CTA has been reported [24, 25].

MR coronary artery imaging has the potential to become a powerful tool for studying plaque progression, because it is radiation-free and non-invasive. Researchers have studied MR coronary angiography since the 1990s [5,26]. Early clinical studies of coronary MRA include ECG-gating, segmented k-space sampling and breath-holding to minimize respiratory artifacts [27,28]. Breath-holding limited the acquisition time, which in turn limited the achievable spatial coverage. Researchers then extended the imaging slab by using 3D fast imaging sequences, such as EPI [29]. Navigator gating and motion compensation was implemented to reduce respiratory artifacts for free breathing scans [30]. Navigator echoes monitor the position of diaphragm, which can then be used to make sure the positions are consistent among all the acquisitions. The popular techniques used in MR angiography are listed in Table 2.1 [14].

MRI can also be used for imaging the coronary artery wall, which can help to visualize the thickening of the wall. Double inversion recovery (DIR) is the most common method for black blood imaging [10]. It was implemented in coronary artery wall studies first using spiral scanning in [31] and then applied to patient studies using Cartesian scanning [1,32]. In these initial patient studies, DIR was placed before a FSE acquisition sequence to remove the blood signal inside the coronary artery. The in-plane resolution could reach as high as 0.5mm to visualize the vessel wall. For 2D imaging, either breath holding or navigator gating could be used [1, 32]. In [1], MR coronary vessel wall imaging was able to successfully detect both the obstructed region and thickening of the vessel wall. In this dissertation, we will mainly focus on coronary artery wall imaging. The details of DIR and other techniques used in the dissertation are discussed in the following section.

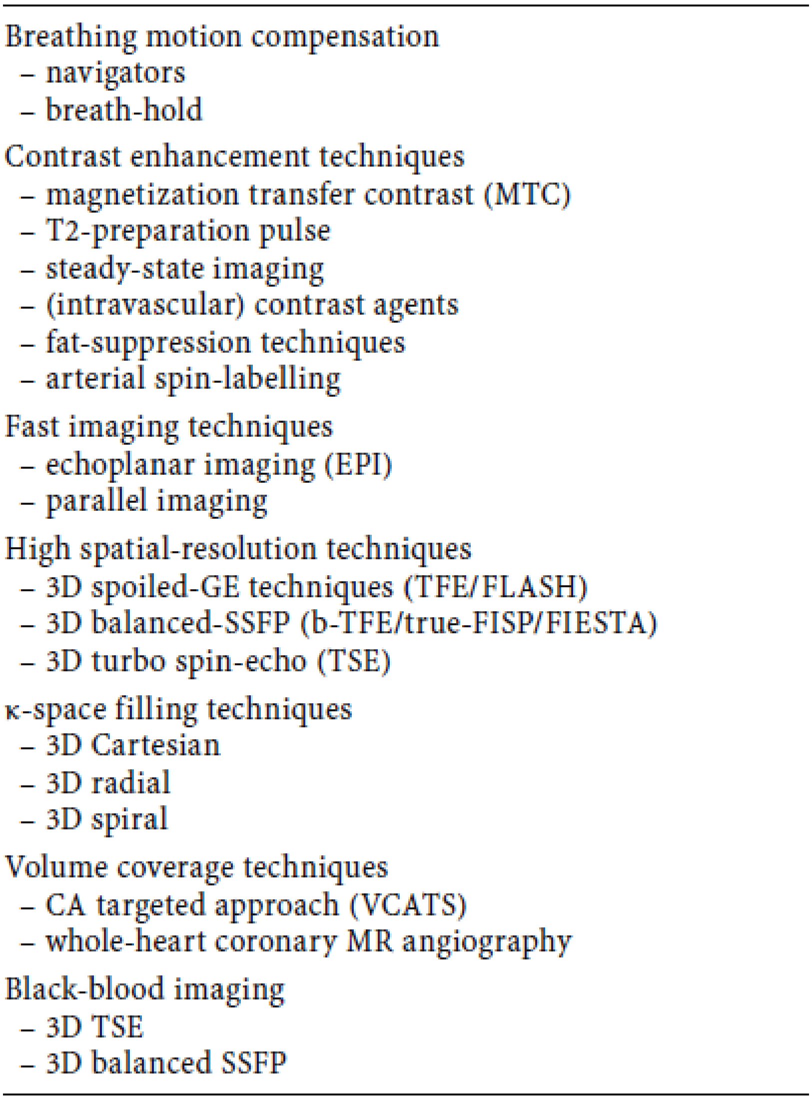

Breathing motion compensation
  - navigators
  - breath-hold

Contrast enhancement techniques
  - magnetization transfer contrast (MTC)
  - T2-preparation pulse
  - steady-state imaging
  - (intravascular) contrast agents
  - fat-suppression techniques
  - arterial spin-labelling

Fast imaging techniques
  - echoplanar imaging (EPI)
  - parallel imaging

High spatial-resolution techniques
  - 3D spoiled-GE techniques (TFE/FLASH)
  - 3D balanced-SSFP (b-TFE/true-FISP/FIESTA)
  - 3D turbo spin-echo (TSE)

κ-space filling techniques
  - 3D Cartesian
  - 3D radial
  - 3D spiral

Volume coverage techniques
  - CA targeted approach (VCATS)
  - whole-heart coronary MR angiography

Black-blood imaging
  - 3D TSE
  - 3D balanced SSFP

Table.2.1. Current strategies used for anatomical assessment of coronary arteries [14].

2.3 Techniques used in Coronary Artery Wall Imaging

2.3.1 Double inversion recovery (DIR)

Double inversion recovery is the most widely used black blood technique in vessel wall imaging, especially for carotid [33] and coronary studies [1]. It was first described in [10]. The pre-pulses contain one non-selective 180-degree pulse, followed by a slice-selective 180-degree pulse, as shown in Fig. 2.3 [34]. After non-selective inversion, both tissue and blood signal are inverted to $-M_0$. The subsequent selective inversion will immediately rotate the magnetization inside the imaging slice back to M_0. During the inversion time, the blood inside the slice is replaced by inverted spins. The magnetization of this blood gradually returns back to zero. The inversion time needed for nulling the blood signal is calculated as follows [10]:

$$TI = T_{1,blood} \times \ln\left(\frac{2}{1+\exp(-TR/T_{1,blood})}\right) \qquad [1]$$

TR is typically set to be equal to the R-R interval if the sequence triggers every heartbeat. An additional delay between the R wave and the DIR module can be used to set the acquisition in mid-diastole. However, the heart rate can vary significantly during the scan, especially in patient studies. The TR then changes for each heartbeat. A dynamic TI algorithm [35] can be used to find the optimal value for nulling the blood. In this method, the real-time heart interval in the previous heartbeat is read out during scan and used for the calculation for the current heartbeat. Studies with dynamic TI are shown to have a better blood suppression in the entire heart region, as illustrated in Fig. 2.4. The red arrows indicate that there is still residual blood in the heart chamber when using constant TI, while the blood in the same region is suppressed in the dynamic TI image. In this work we are using real-time heart interval monitoring to dynamically calculate TI and delay time in all of our scans.

Since there is a delay time between the DIR module and the image acquisition, the slice position in the DIR and imaging modules can be offset, which leads to incomplete blood suppression. The slice thickness of the selective pulse in the DIR module is typically set to about 2.5 times the imaging slice thickness to avoid this problem [32].

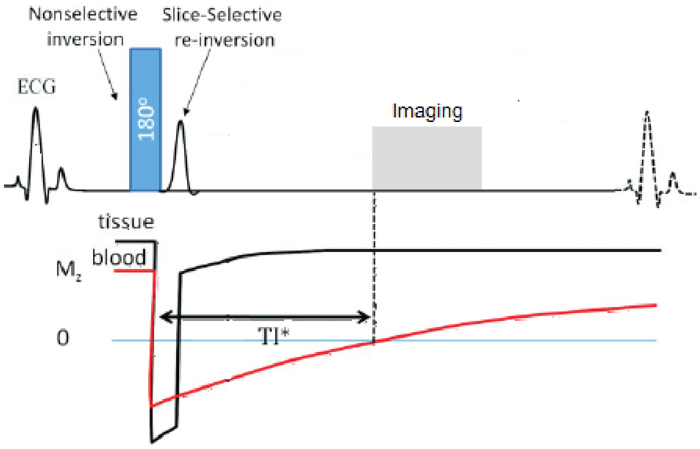

Fig. 2.3. Illustration of the double inversion recovery method for black-blood imaging [34].

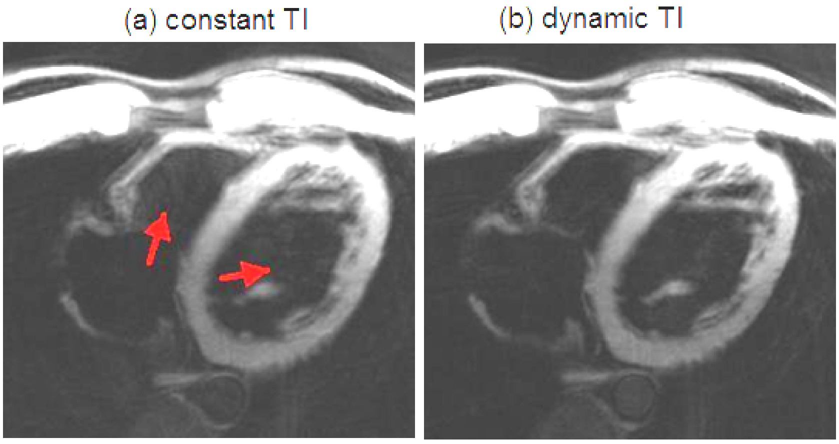
(a) constant TI
(b) dynamic TI

Fig. 2.4. Black-blood double inversion recovery cardiac images with (a) constant TI and (b) dynamic TI. Red arrows indicate incompletely suppressed blood in the ventricles.

2.3.2 Navigator gating in coronary artery imaging

To overcome the time limit set by breath-holding, navigator gating is often used in cardiovascular MR imaging. Navigator gating monitors the respiration of patients to reduce respiratory artifacts caused by the motion of chest wall and internal organs [36].

The navigator can use two orthogonal pulses or a 2D selective pulse to localize the signal to the right hemi-diaphragm when imaging coronary arteries. A readout gradient is applied to form a 1D image, which is used to monitor the patient's respiration. It should be noticed that if two intersecting planes are used for the navigator, this can result in a signal loss in the region of interest (ROI) [37]. Figure 2.5 shows the typical location of the navigator pulse and the diaphragm position it detects [36].

There are two types of navigator gating that differ in the way that the diaphragm location data are processed: prospective gating and retrospective gating. In prospective gating, the navigator is placed before image acquisition. This method will only allow acquisition if the diaphragm position is inside a certain range; otherwise, it will skip the readout. In retrospective gating, all of the data corresponding to different positions of the diaphragm is acquired. After creating a histogram of diaphragm location, only the data collected when the diaphragm position is close to the peak of the histogram is preserved [38].

Prospective gating can better reduce motion artifacts and is more time efficient than retrospective gating. It is more computationally demanding than retrospective gating [38]. An adaptive correction of respiratory motion can be combined with navigator gating to increase efficiency and reduce scan time compared to gating-only methods [37,39]. It has been reported that there is a linear relationship between cardiac and diaphragm displacement. As a result, a measure of diaphragm position can be used to adaptively adjust the imaging position [39]. In our work, we use prospective navigator gating with respiratory compensation as a comparison with breath-holding. The scheme of prospective navigator gating is shown in Fig. 2.6 [37].

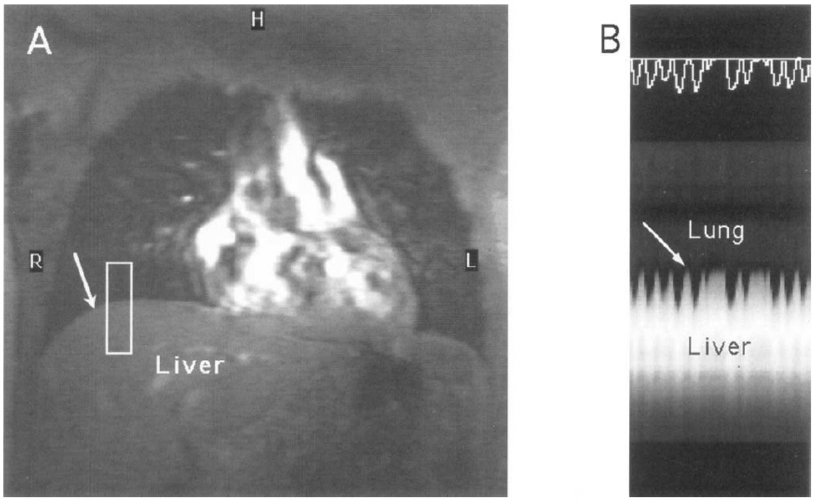

Fig. 2.5. (A) A 2D selective navigator placed at the dome of the right hemi-diaphragm, as indicated by the white rectangle in a human heart scout image. (B) A vertical 1D image shown the movement of diaphragm through time (about 1min). White lines indicate the calculated diaphragm positions [36].

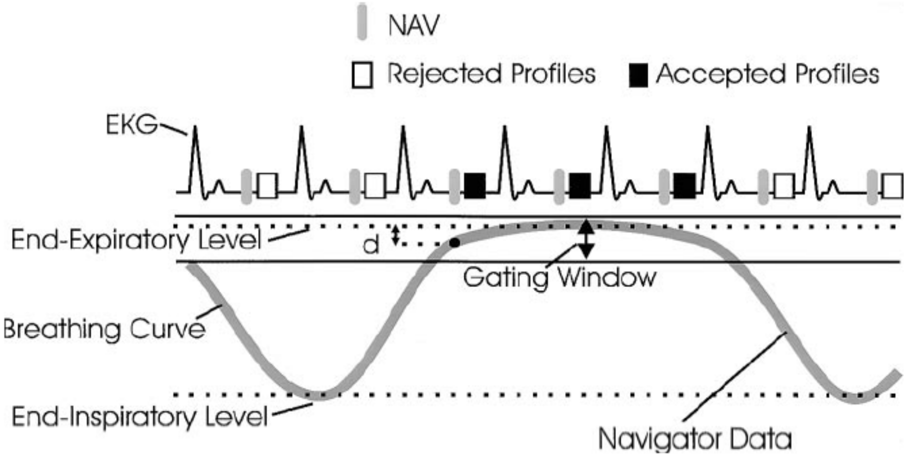

Fig. 2.6. Schematic chart of navigator gating showing an EKG and a breathing curve [37].

Chapter 3

Synthetic Target Image Reconstruction for Cartesian Parallel Imaging

3.1 Introduction

Parallel imaging with multiple receiver coils has been widely used in various applications of MRI to shorten the imaging time. A number of parallel image reconstruction methods have been developed. SENSE [2] is an established image-domain parallel reconstruction algorithm, and it will yield an optimal reconstruction if accurate coil sensitivities can be obtained. The encoding matrix used in SENSE can be modified to make it suitable for arbitrary k-space trajectories [40]. The main challenge with SENSE is acquiring accurate coil sensitivity profiles, which are hard to estimate in some applications. SMASH [41] and PARS [42] also have the same problem of coil sensitivity calculation. Auto-calibrated coil-by-coil reconstruction methods eliminate the need for explicit coil sensitivity calculation. In GRAPPA [3] and AUTO-SMASH [43], with auto-calibration, each individual coil is reconstructed and then combined by a conventional coil combination method such as root sum-of-squares. GRAPPA can remove aliasing and achieve nearly optimal SNR for a Cartesian trajectory.

These parallel reconstruction methods are able to perform unaliasing successfully. But, as the number of coil elements in the array increases, the reconstruction time becomes a significant issue. For a 32-channel coil and a large dataset, online GRAPPA reconstruction can take up to 10s. SENSE requires approximately the same computation time. As the number of coil elements increases to 128, we can expect a much longer reconstruction time. For certain applications such as real-time imaging, the slow reconstruction speed can become an obstacle. Thus, there is a need to develop a parallel image reconstruction method that requires less computation. PILS [44] is one possible solution. The main idea of PILS is to generate a Fermi mask of each coil image. By applying masks, it can get rid of aliasing of the coil images, which can then be combined together. The disadvantage of PILS is that it depends on coil size and the imaging point spread function (PSF). For large coil elements and high acceleration factors, PILS is not an option.

Here we present a novel parallel reconstruction method called the synthetic target algorithm, which was first proposed by Weitian Chen [45,4]. It uses auto-calibration to avoid coil sensitivity estimation. The unaliasing step is performed only once to avoid coil-by coil calculation. Thus, it eliminates a key factor that can lead to long computation time in GRAPPA. Ideally, it can reduce the reconstruction time by roughly the number of coils. With the help of other algorithms such as array compression [9] and parallel computing, the computation time can be further decreased. We will test the algorithm on a variety of datasets and show that this method gives comparable image quality to GRAPPA but with substantially less computation time.

The synthetic target method can be applied in both the image domain and k-space domain; established auto-calibrated parallel reconstruction techniques are typically performed in the k-space domain. In theory, the image-space reconstruction enables synthetic target to handle any arbitrary trajectory. In this chapter, the discussion is focused on Cartesian k-space trajectories.

3.2 Method

3.2.1 Review of GRAPPA

In order to understand the synthetic target reconstruction process, it is helpful to review the original GRAPPA algorithm [3]. In GRAPPA, each missing line in k-space can be reconstructed by a linear combination of the neighboring acquired lines from all the coils. The weighting of the combination is obtained by training on autocalibration scan (ACS) lines. Based on Eq. 2 in [3], the GRAPPA reconstruction process can be expressed as

$$S_j(k_x, k_y - m\Delta k_y) = \sum_{l=1}^{N_c} \sum_{b=0}^{N_b - 1} n(j, b, m, l) S_l(k_x, k_y - bA\Delta k_y) \qquad [3.1]$$

where $S_j(k_x, k_y - m\Delta k_y)$ represents the missing k-space data at location $(k_x, k_y - m\Delta k_y)$ in the j_{th} target coil. It has an $m\Delta k_y$ k-space offset from the acquired data. N_c is the number of coils, N_b is the number of blocks used for the reconstruction, A is the acceleration factor, and $n(j, b, m, l)$ are the weights that are used in the linear combination of adjacent lines to reconstruct the missing lines. $S_l(k_x, k_y - bA\Delta k_y)$ is the acquired k-space data for the l_{th} coil and b_{th} block with an $bA\Delta k_y$ k-space offset from the acquired data. After each missing data point is estimated, an unaliased coil image can be reconstructed. The final image is then formed by root sum-of-squares of the target coil images.

As stated by Griswold in [46] and implied by Bankson and Wright [47], Eq.3.1 can be viewed as a convolution process as follows:

$$S_j(k_x, k_y + \Delta k_y) = \sum_{l} \sum_{\tau_x} \sum_{\tau_y} n^l(\tau_x, \tau_y) S_l(\tau_x - k_x, \tau_y - k_y) \qquad [3.2]$$

Equation 3.2 is an expansion of Eq. 3.1, where $n^l(\tau_x, \tau_y)$ stands for the weight set used in reconstruction. The GRAPPA reconstruction is now modeled as a 2D convolution operation [46].

Chen stated in [4] that Eq.3.2 can be written as:

$$M_j(k) = \sum_{l=1}^{N_c} H_l^j(k) * \overline{M_l}(k) \qquad [3.3]$$

where $H_l^j(k)$ is the k-space convolution kernel. $\overline{M_l}(k)$ is the subsampled k-space data from each coil. $M_j(k)$ is the reconstructed missing k-space data for the jth target coil. It should be noted that in GRAPPA, the unaliasing process is performed on each coil. The reconstruction time increases significantly as the coil number increases.

3.2.2 Theory for Synthetic Target algorithm

In [4], Chen et al. described the basic synthetic target algorithm, which we review here. In the image domain, the convolution process in Eq.3.3 becomes a pixel-by-pixel linear combination to unalias each coil image:

$$m_j(r) = \sum_{l=1}^{N_c} h_l^j(r)\overline{m_l}(r) \qquad [3.4]$$

$m_j(r)$, $h_l^j(r)$ and $\overline{m_l}(r)$ are the Fourier transforms of $M_j(k)$, $H_l^j(k)$ and $\overline{M_l}(k)$, respectively. $\overline{m_l}(r)$ is the aliased coil image for l_{th} coil. $h_l^j(r)$ is the weighting mask for the l_{th} coil. As mentioned above, $H_l^j(k)$ is a small kernel in k-space, and thus $h_l^j(r)$ is a slowly varying function in the image domain. $m_j(r)$ is the unaliased coil image.

According to [48], the final image can be calculated by a linear pixel-by-pixel combination of unaliased coil images, which can be expressed by the following equation:

$$m_0(r) = \sum_{l=1}^{N_c} w_l^*(r) m_l(r) \qquad [3.5]$$

$m_l(r)$ is the unaliased coil image obtained by Eq.3.3. $w_l^*(r)$ is the smooth weighting coefficient for the l_{th} coil. It contains the noise correlation and coil sensitivity information, as follows:

$$\overline{w} = \alpha R_n^{-1}\overline{c} \qquad [3.6]$$

R_n is the noise correlation matrix. α is calculated from the square matrix of mutual resistance and the magnitude of the transverse magnetic field for unit current in the coil. It usually treated as constant. The absolute value of α only affects the magnitude of the final image [48]. The vector $\overline{c}$ is the value of the sensitivity map at each pixel. Plugging Eq. [3.4] into Eq. [3.5] yields the following expression:

$$m_0(r) = \sum_{j=1}^{N_c} w_j^*(r) \sum_{l=1}^{N_c} h_l^j(r)\overline{m_l}(r) \qquad [3.7]$$

If we define $u_l(r) = \sum_{j=1}^{N_c} w_j^*(r) h_l^j(r)$, Eq.3.6 can then be written as

$$m_0(r) = \sum_{l=1}^{N_c} u_l(r)\overline{m_l}(r) \qquad [3.8]$$

Equation 3.8 suggests that the final composite image can be formed using a linear combination of aliased coil images [4]. The main task is now to determine the weighting masks $u_l(r)$. According to Eq.3.7, $u_l(r)$ is a combination of $w_j^*(r)$ and $h_l^j(r)$. The former contains coil sensitivity information, which is usually window-shaped in the image domain. The latter is the Fourier transform of a small GRAPPA convolution kernel, which corresponds to a slowly varying mask. As a result, $u_l(r)$ should also be smoothly varying in the image domain [4].

As in GRAPPA, we would like to auto calibrate $u_l(r)$ using ACS lines. The goal of the training process is to find the $u_{l,t}(r)$ that minimizes the following least square norm:

$$\left\| m_{0,t}(r) - \sum_{l=1}^{N_c} u_{l,t}(r)\overline{m}_{l,t}(r) \right\|_2 \qquad [3.9]$$

where the subscript t stands for low-resolution images acquired by ACS lines. $m_{0,t}(r)$ is a target unaliased low resolution image formed by fully sampled ACS lines. $\overline{m}_{l,t}(r)$ is a low resolution image reconstructed using undersampled ACS lines. We assume that the weighting masks $u_{l,t}(r)$ used to reconstruct low-resolution images will be suitable for reconstructing high-resolution, full FOV images. The difference between $m_{0,t}(r)$ and $m_0(r)$ is a truncating window applied in k-space, which corresponds to a slowly varying, sinc-shaped mask convolved with the original image. We will define the mask to be $s(r)$, and the convolution process is described below:

$$\begin{aligned} & m_{0,t}(r) = FFT(rect(r)) * m_0(r) = s(r) * m_0(r) \\ & = \sum_{|\Delta r| < r_0} s(\Delta r) m_0(r - \Delta r) \\ & = \sum_{|\Delta r| < r_0} s(\Delta r) \sum_{l=1}^{N_c} u_l(r - \Delta r)\overline{m_l}(r - \Delta r) \end{aligned} \qquad [3.10]$$

Because $u_l(r)$ is the slowly varying mask, we assume $u_l(r) = u_l(r - \Delta r)$ inside a small region $|\Delta r| < r_0$. Equation 3.9 can be further simplified as follows:

$$\begin{aligned} m_{0,t}(r) &= \sum_{|\Delta r| < r_0} s(\Delta r) \sum_{l=1}^{N_c} u_l(r - \Delta r)\overline{m_l}(r - \Delta r) \\ &= \sum_{l=1}^{N_c} u_l(r) \sum_{|\Delta r| < r_0} s(\Delta r) m_l(r - \Delta r) = \sum_{l=1}^{N_c} u_l(r)\overline{m}_{l,t}(r) \end{aligned} \qquad [3.11]$$

Equation 3.11 suggests that the weighting masks trained with low-resolution images can be applied to reconstructing full FOV, high-resolution images later [4].

To constrain the training and reconstruction process, we can approximate $u_l(r)$ by a linear combination of orthogonal basis functions [4]:

$$u_l(r) = \sum_{k=1}^{K} a_k^l f_k(r) \qquad [3.12]$$

In this expression, $f_k(r)$ are the basis functions, which can be polynomial or exponential functions, for example. a_k^j are the coefficients of the functions for the l_{th} coil. K is the number of basis functions. Because $u_l(r)$ is slowly varying, we can set K to a small value (usually 4-6 in our studies). We can determine a_k^j by minimizing the following least square norm:

$$\left\| m_{0,t}(r) - \sum_{l=1}^{N_c} \sum_{k=1}^{K} a_k^l f_{k,t}(r) \overline{m}_{l,t}(r) \right\|_2 \qquad [3.13]$$

More constraints can be added to further improve the optimization, such as Tikhonov regularization [49].

3.2.3 Choice of targets

The key element of the image reconstruction is the training of the weighting coefficients; thus, the choice of the target image $m_{0,t}(r)$ will significantly affect the results. There are several ways to compute the low-resolution target image. In [4], Chen et al. stated that the first choice is Roemer's method, given in [48]. As in Eq. 3.4, assume $m_{0,t}(r)$ is obtained by:

$$m_{0,t}(r) = \sum_{l=1}^{N_c} w_{l,t}^*(r) m_{l,t}(r),$$

where $m_{l,t}(r)$ are unaliased low resolution coil images reconstructed by ACS lines. $w_{l,t}^*(r)$ is the combination matrix that contains coil sensitivity information. Roemer's method is designed to give the maximum SNR. However, it requires the estimation of sensitivity maps, which increases complexity. Another possible method is adaptive reconstruction, which estimates combination coefficients by calculating the eigenvectors of the array correlation matrix [50]. These two techniques both require additional time to compute the magnitude and the phase of the target image. A simple root of sum-of-squares (SOS) of the low-resolution coil images can give results comparable to composite combination yet takes less computation time. SOS combination is expected to generate a magnitude image with zero phase, which corresponds to constraining the final image to be real. We will compare the three methods below.

3.2.4 Array compression

Array compression methods can reduce computation time for multi-coil image reconstruction [9,51,52]. These methods use singular value decomposition (SVD) in either the image domain or the k-space domain to reduce the coil dimension. According to [9], one can reduce the size of datasets from independent channels before any reconstruction algorithm. The compression is especially effective when applied to large coil arrays. In this chapter, all datasets are acquired using a 32-channel coil. These datasets can be compressed to 10 channels with no significant reduction in SNR. The reconstruction is then three times faster.

The array compression is accomplished using Principal Component Analysis (PCA), which is a commonly used method to reduce the dimension of datasets without losing important information. First, we arrange the dataset in a matrix of dimension (number of image pixels) × (number of coils). We then apply SVD along the coil dimension. By selecting the M biggest eigenvalues out of N, we can achieve an M/N compression ratio. Array compression is applied before image reconstruction, as illustrated in Fig. 3.1.

3.2.5 Multi-Target Synthetic Target

The major difference between the synthetic target and other auto-calibration methods is the choice of target images. In GRAPPA, k-space data from each coil is treated as a single target, so the number of targets is equal to the number of coils. In contrast, in the synthetic target method, these images are combined into a single target image. However, the synthetic target method can be easily modified to choose an arbitrary number of target images. As an example, consider a dataset with 6 channels. We can divide the 6 coils to 2 groups, each with 3 coils, and synthesize one target image for each group. Then we perform the typical synthetic target algorithm for each target image, yielding an image for each target. The two reconstructed images can be combined using sum-of-square methods to obtain the final image. An illustration of this process is given in Fig. 3.2. When each group contains only one coil image, the revised synthetic target method is equivalent to GRAPPA in the image domain. This modification of the original synthetic target method can help to eliminate the effect of imperfect target image calculation. With multiple target images, any signal loss can largely be eliminated. The tradeoff is an increase in computation time.

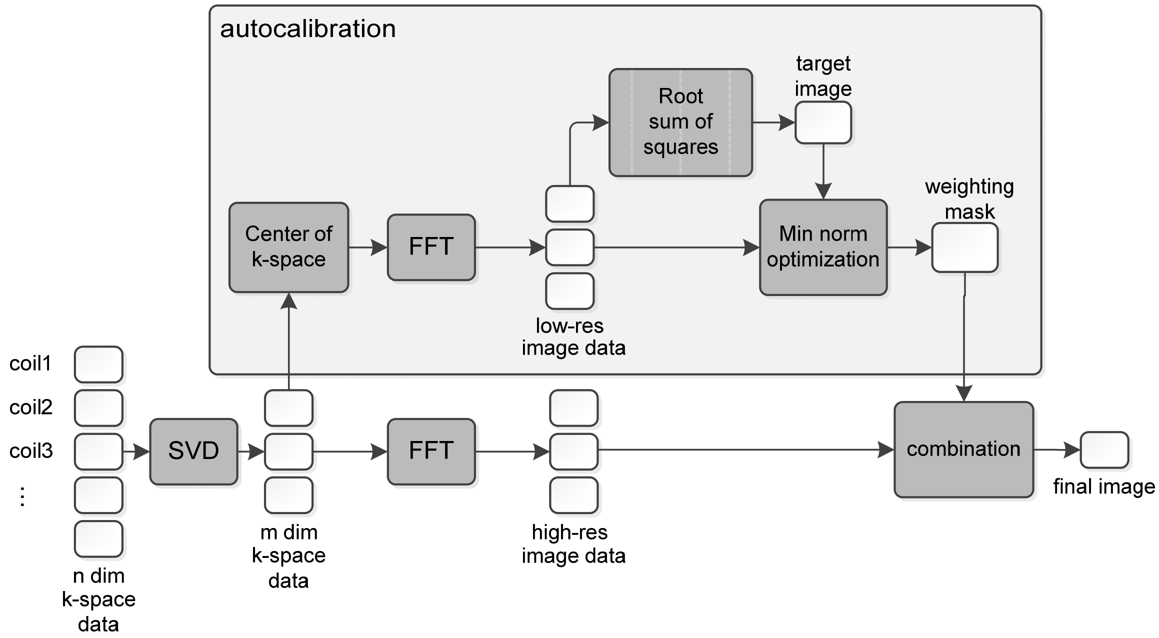

Fig. 3.1. Overview of array-compressed synthetic target image reconstruction.

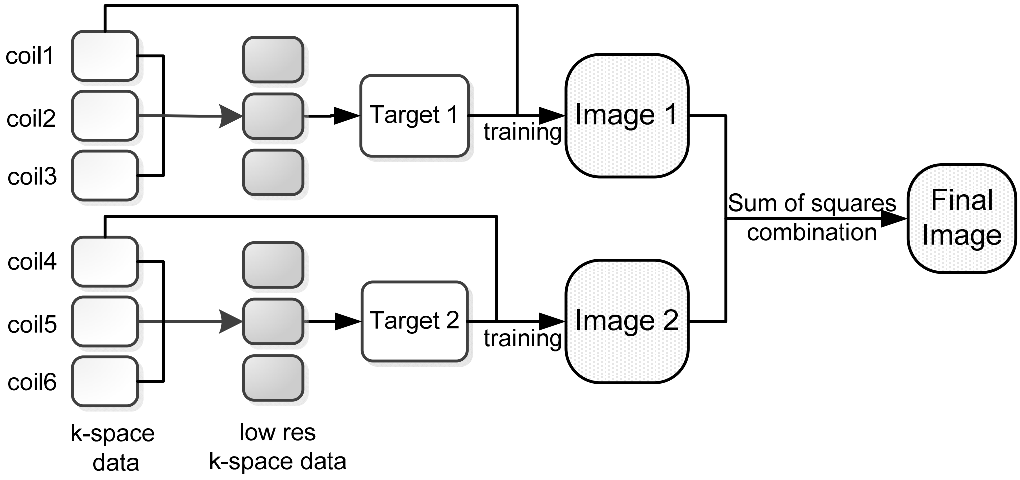

Fig. 3.2. Overview of multi-target synthetic target image reconstruction.

3.3 Methods

6-channel phantom imaging

A phantom dataset was acquired using a Siemens 1.5T Avanto scanner with a 6-channel array coil with a Cartesian TSE sequence. FOV = 28cm, slice thickness = 5mm, TR/TE = 600/98ms. We collected 26 ACS lines, and the acceleration factor was set to two. We used three methods to calculate the target images: Roemer, adaptive reconstruction, and square root of sum-of-square (SOS). Both the magnitude and the phase of the final image are presented. We chose the regularization factor to be e-11 for all of the image domain reconstructions. GRAPPA images and direct combination of all coil images are shown for comparison. The reference 1X dataset was reconstructed using fully sampled k-space. The computation time was evaluated using a desktop computer with a 1.66GHz Intel Core 2 duo CPU and 2GB of memory.

32-channel phantom imaging

To explore the computation speed of the synthetic target method, we collected a 32-channel dataset on a Siemens Avanto 3T scanner using a FLASH sequence. FOV = 400 mm, slice thickness = 5mm, TR/TE = 9.1/4.8ms, flip angle = 15. The dataset was originally fully sampled and then subsampled with 2X, 3X and 4X acceleration. The number of ACS lines can be chosen arbitrarily. In this study we set the number to 26.

For all of the image reconstructions, we set the array compression ratio to be 0.3 (10 coils). We will show that at this rate, the computation could be maximally accelerated without losing SNR. We also compared the reconstruction time with GRAPPA as the coil number increases (and the compression ratio decreases). The difference images (X6000) of all the reconstruction results were calculated. Both the synthetic target and GRAPPA algorithms were developed using Matlab (MathWorks Inc., Natick, MA), and executed on a 6-node computer cluster; each node had two 2.8GHz Intel Xeon CPUs and 2GB memory.

Multi-target synthetic target reconstruction was also performed using this dataset. Data from all 32 coils was divided into 2, 4, 8, 16, and 32 groups, and target images were generated for each group. After performing the synthetic target algorithm for each group, the reconstructed images from all groups were combined into a final image. We computed the mean square error (MSE) for the final image as a function of the number of targets. The results were compared to images reconstructed using GRAPPA.

In vivo brain imaging

We used a Cartesian TSE sequence to collect a transverse slice of the brain of a normal volunteer. We acquired the dataset using a Siemens 1.5T Avanto Scanner. A head coil with 12 elements was used for parallel imaging. The imaging protocol was as follows: FOV = 28cm, TR/TE = 4000/99ms, slice thickness = 5mm. We collected data with 2X, 3X and 4X accelerations, each with 26 ACS lines. The final results were compared with GRAPPA reconstructions.

Cardiac in vivo imaging

In this study, we used a breath-hold CINE gradient echo sequence to obtain a right coronary artery wall localization image on seven healthy volunteers (ages 27 to 32, all male) using a Siemens Avanto 3T scanner and a 32-channel coil array. Image parameters were as follows: FOV = 34cm, TR/TE = 44.52/1.82ms, slice thickness = 6mm, flip angle = 50, segments = 12. The sequence was ECG triggered on every heartbeat. The dataset had 26 ACS lines in the center of k-space and the rest of k-space was undersampled by a factor of 2. Coil compression was used to reduce the number of coils from 32 to 10 to accelerate the synthetic target reconstruction. GRAPPA images were used as a reference to calculate MSE and structural similarity index (SSIM) of the synthetic target images.

3.4 Results

3.4.1 Phantom study for choice of targets

Figure 3.3 shows phantom images reconstructed using three different target images. Synthetic target reconstruction with each of the three target images removes aliasing artifacts compared to a direct (non-parallel) image reconstruction (Fig. 3.3g), as shown in magnitude images (Fig. 3.3a-c). The Roemer image gives the best results, although the time required for generating the target image is the longest (5.05s). With the adaptive reconstruction target, there is a signal drop-off in the center of the image. The SOS target also has a signal drop-off in the center of the image, and the aliasing is not completely suppressed. The computation time for target generation was 2.68s and 2.50s for the adaptive reconstruction and sum-of-squares methods, respectively. Figure 3.3h is the GRAPPA reconstruction of this data. The center signal appears dark in the GRAPPA image as in Adaptive and SOS image. The Roemer (Fig. 3.3d) and adaptive reconstruction (Fig.3.3e) targets yield similar estimates of the final phase, although the Roemer phase map has more oscillations in the background. The SOS phase map (Fig. 3.3f) is nearly zero as expected.

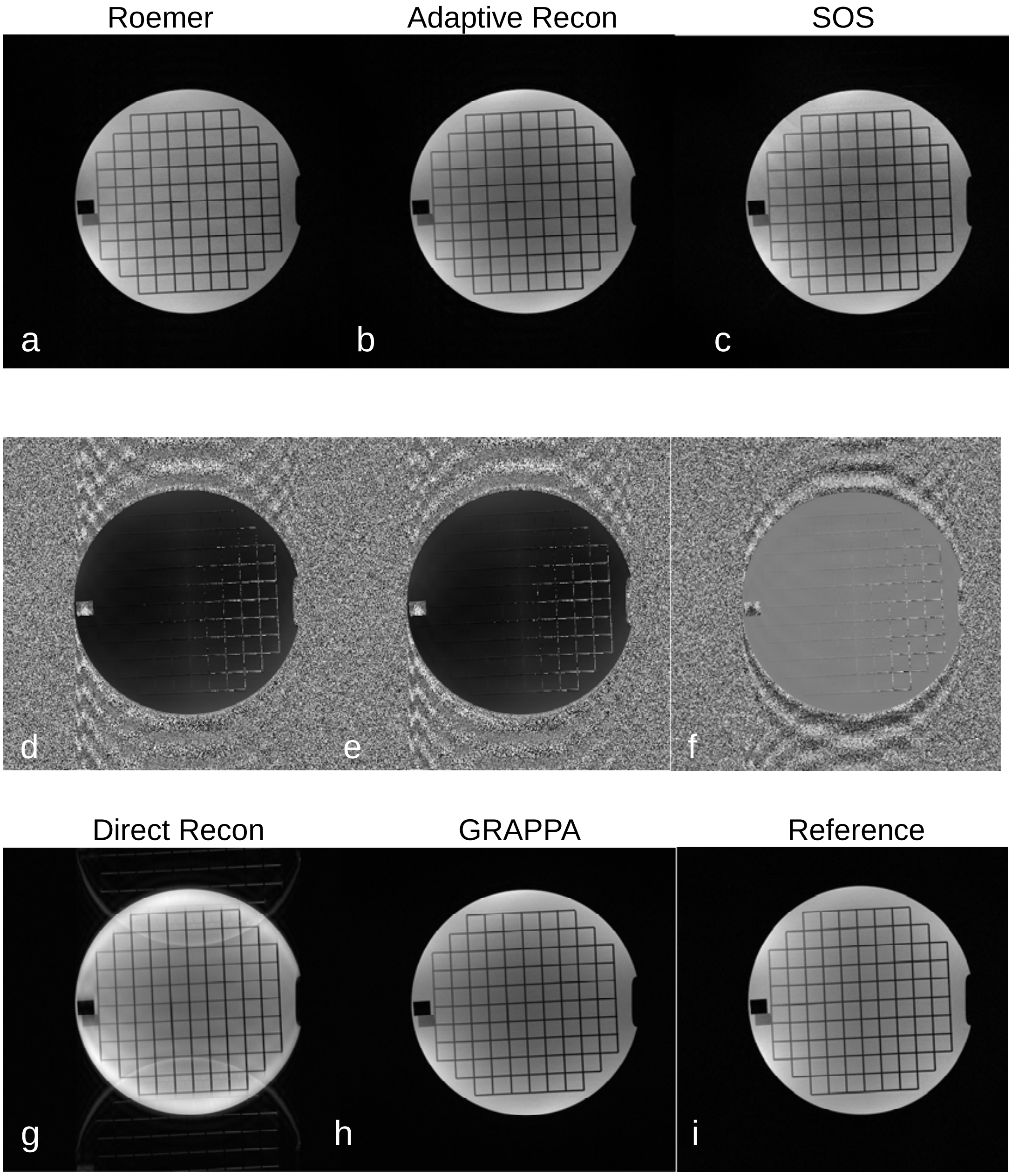

Fig. 3.3. Phantom images reconstructed by the synthetic target algorithm. The target images were calculated using Roemer’s method, adaptive reconstruction, and SOS. (a-c) are the reconstructed magnitude images and (d-f) are the corresponding phase maps. (g) is the direct combination of

aliased coil images. (h) is a 2X image reconstructed by GRAPPA. (i) is used as the reference image to calculate MSE.

3.4.2 Array compression and reconstruction speed

We also tested the synthetic target algorithm using a 32-channel coil. The final phantom images are shown in Fig. 3.4. The difference images are presented for comparison, multiplied by a factor of 6000. As shown in Fig. 3.4, the synthetic target method works successfully on removing the artifacts for all cases. Especially for 2X acceleration, the difference between the synthetic target reconstruction and the reference images is very small, which implies that the synthetic target method can reconstruct the image with minimal loss of image quality.

We also reconstructed the 2X image with three different levels of coil compression. The results are shown in Fig. 3.5. Undersampling artifacts were successfully removed in each case. However, the difference images demonstrate that the image reconstructed with 5 compressed coils has some loss of information. This is consistent with Fig. 3.6, which shows the amplitude of the normalized eigenvalues of this data. The first 10 eigenvalues are significantly larger than the rest, indicating that the corresponding 10 eigenvectors should give a good estimation of the total dataset without losing much information. This provides evidence that compressing from 32 to 10 channels will result in relatively minor changes in the reconstructed image.

The reconstruction speed was also studied. We applied synthetic target, synthetic target with parallel computing, and GRAPPA on the 2X dataset. As the array compression rate decreased, the number of coils used for reconstruction increased. The number of coils studied were 8, 11, 17, 24, and 32. The computation time is listed in Table 3.1. The comparisons of synthetic target to GRAPPA and synthetic target with and without parallel computing are shown in Figs. 3.7 (a) and (b), respectively. For all compression rates, synthetic target accelerates the image reconstruction significantly.

The data is consistent with the hypothesis that the synthetic target method will shorten the computation time by roughly the number of coils as compared to GRAPPA. The computation time of the synthetic target method increases approximately with the number of coils. Parallel Computing can further increase the speed by distributing the reconstruction tasks to different nodes. But for a smaller number of coils, the time of communication between the nodes will become dominate thus the reconstruction time will increase.

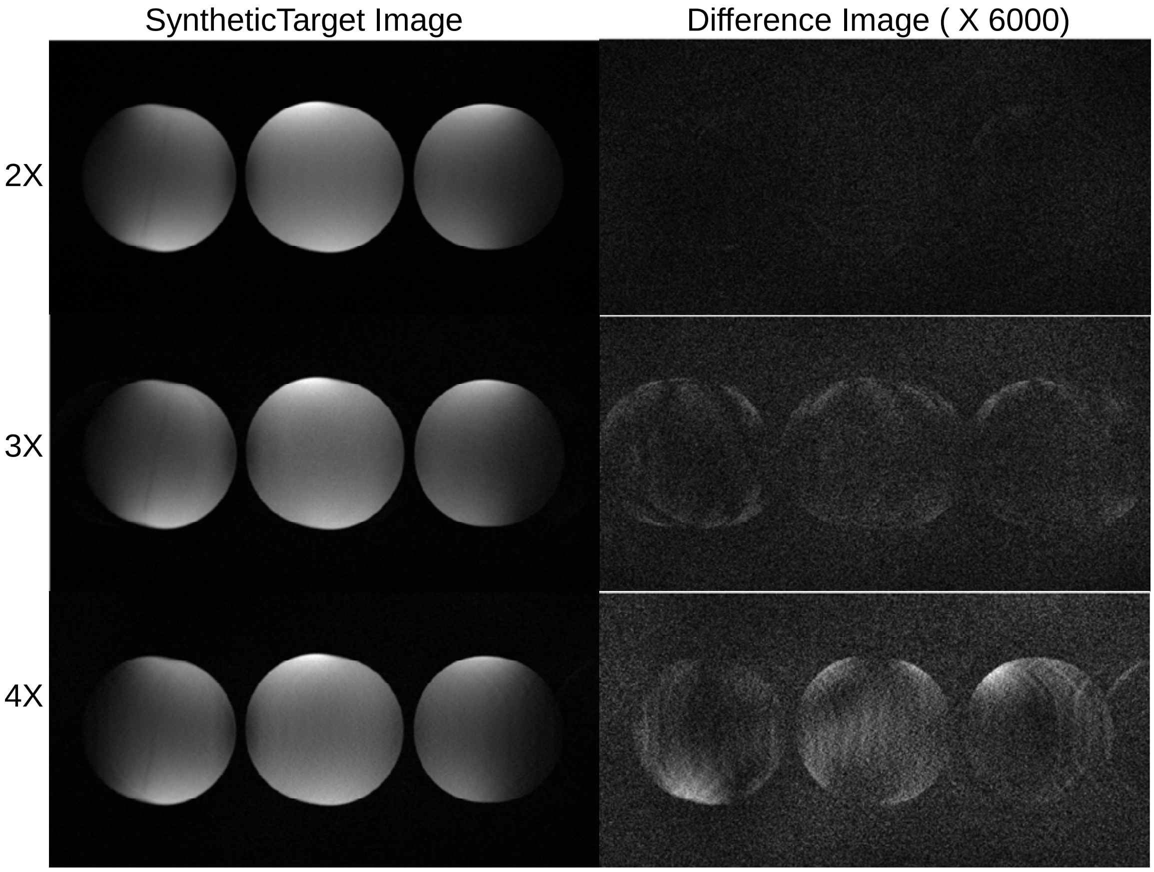

Fig.3.4. 32-channel phantom images reconstructed using the synthetic target method with 2X, 3X and 4X acceleration. Corresponding difference images are also presented (×6000).

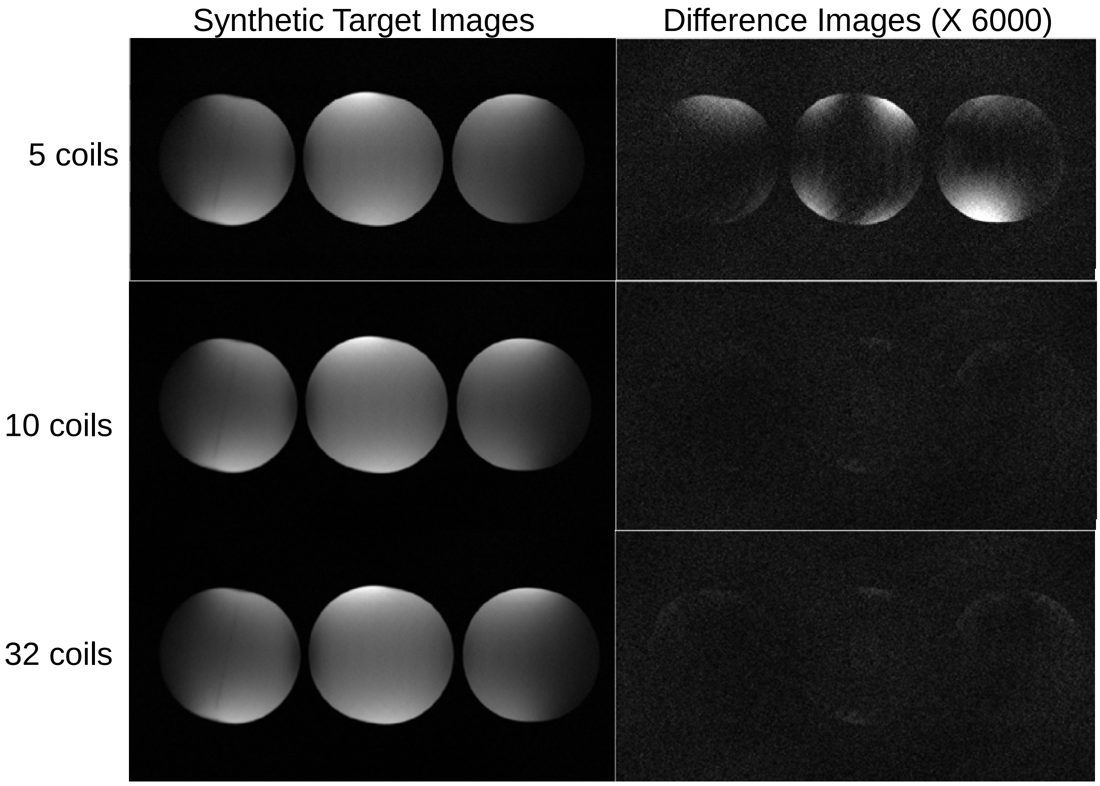

Fig. 3.5. Phantom images reconstructed using the 2X synthetic target method with 5, 10 and 32 compressed coils and the corresponding difference images (×6000).

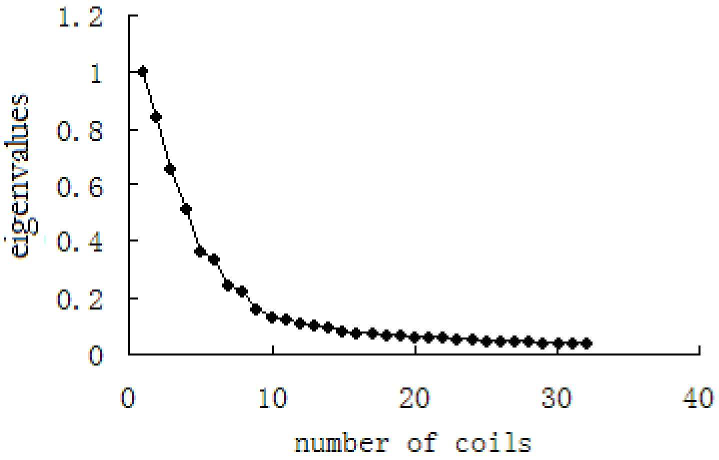

Fig. 3.6. Normalized eigenvalues generated by SVD of 32-channel raw data.

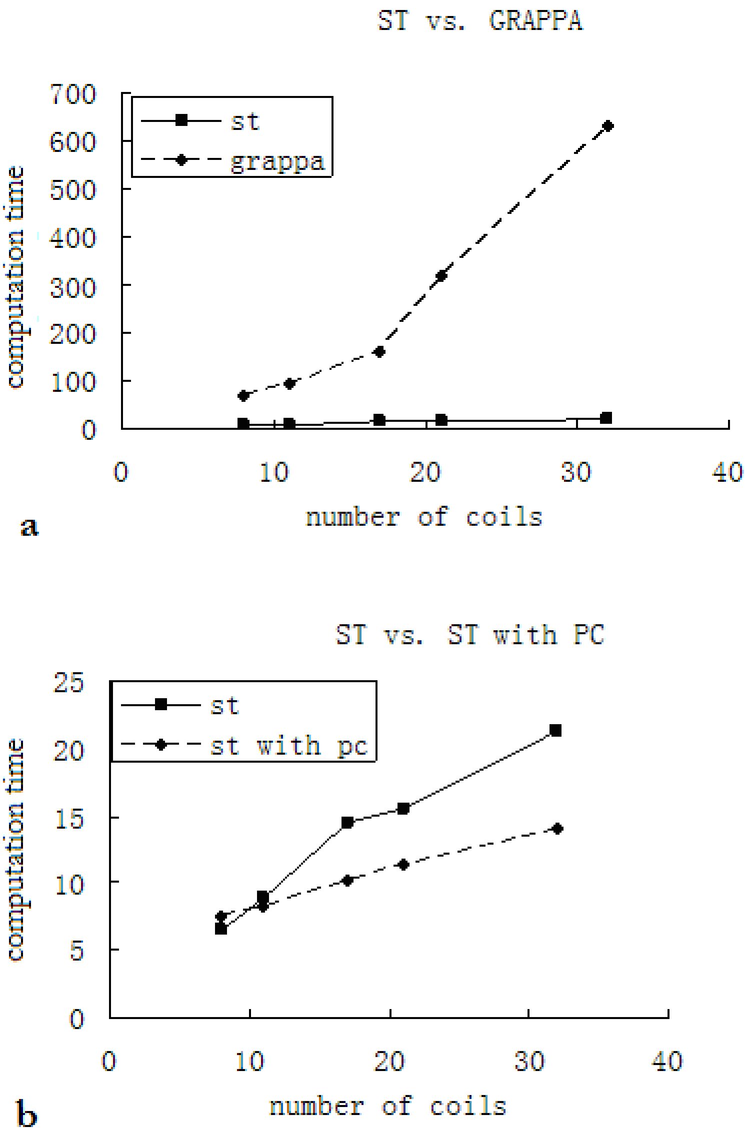

Fig. 3.7. Computation time comparison as a function of the number of coils. (a) Synthetic target (st) vs GRAPPA. (b) Single-threaded synthetic target reconstruction vs. synthetic target with parallel computing (pc) The results were calculated using 8, 11, 17, 24 and 32 compressed coils using 32-coil data.

	8	11	17	24	32
ST	6.58	8.83	14.56	15.58	21.35
ST with PC	7.48	8.34	10.22	11.38	14.02
GRAPPA	68.83	93.26	161.93	320.48	631.03

Table 3.1 Computation time for 32-channel data using synthetic target, synthetic target with parallel computing (PC) and GRAPPA.

3.4.3 Multi-Target studies

As the number of targets increases, the mean square error of synthetic target final images drops, as shown in Fig.3.8 (a). When each coil image is used as a separate target, the synthetic target method turns out to have a similar unaliasing strategy to GRAPPA. In this case, the synthetic target reconstructed image has a MSE close to a GRAPPA image, which means multi-target synthetic target can achieve a comparable image quality to GRAPPA. When a single target is used, the MSE in this simulation is approximately twice that in the GRAPPA image. As expected, the computation time increases as the number of targets increases, as shown in Fig.3.8 (b). One can choose appropriate numbers of targets to achieve a balance between image quality and reconstruction speed. For 2X undersampled images, single-target synthetic target can unalias undersampling artifacts efficiently, according to the results in Fig. 3.4. When reconstructing data with a higher acceleration factor, it may be desirable to use 2-4 targets to better eliminate artifacts.

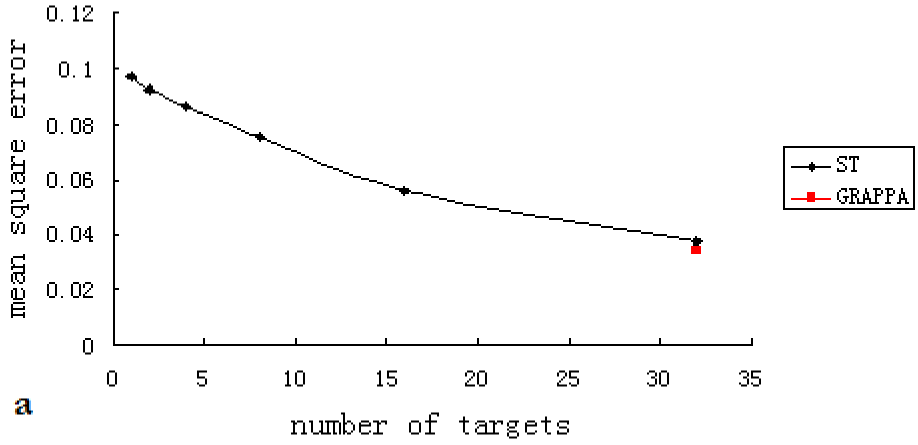

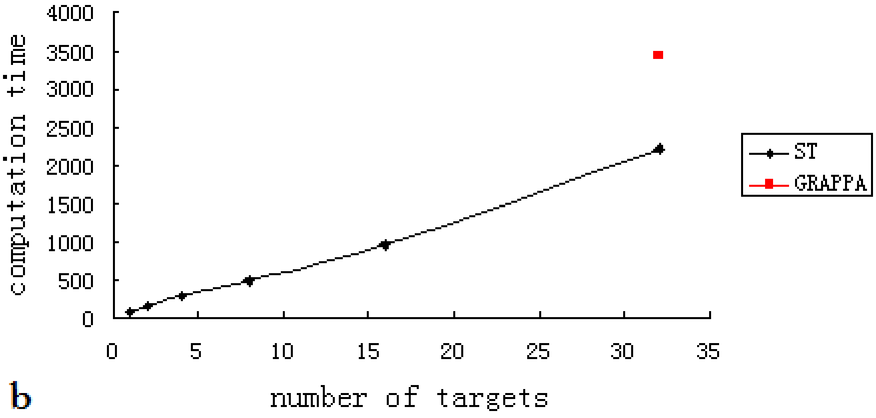

Fig. 3.8. (a) Mean square error and (b) computation time of synthetic target reconstructions when the number of targets is set to 1, 2, 4, 8, 16, and 32.

3.4.4 In-vivo results

In vivo brain images reconstructed with acceleration factors 2X, 3X, and 4X are shown in Fig. 3.9. Both the direct sum-of-square images (Fig. 8a-c) and the GRAPPA images (Fig. 3g-i) are presented for comparison. Figure 3.9d-e demonstrates that the synthetic target method successfully removes aliasing in all three cases. The synthetic target gives generally comparable image quality to GRAPPA, although the GRAPPA images are slightly smoother and less noisy in some areas of the image.

Figure 3.10 shows in vivo cross-sectional views of the right coronary artery acquired from two volunteers. Synthetic target and GRAPPA image reconstructions of 2X undersampled data are shown. The mean MSE and STD of the synthetic target images from seven volunteers were 1.22e-7 and 6.04e-8, respectively. Mean and STD of SSIM were 0.9197 and 0.0217, respectively. The synthetic target method successfully removed aliasing artifacts and provided images that have small MSE and high SSIM when using GRAPPA images as references. As in Fig. 9, the two sets of reconstructed images have similar image quality in most regions. However, there is some signal drop off in the chest wall region in the bottom left image (indicated by red arrow). This phenomenon appeared in several datasets in our study.

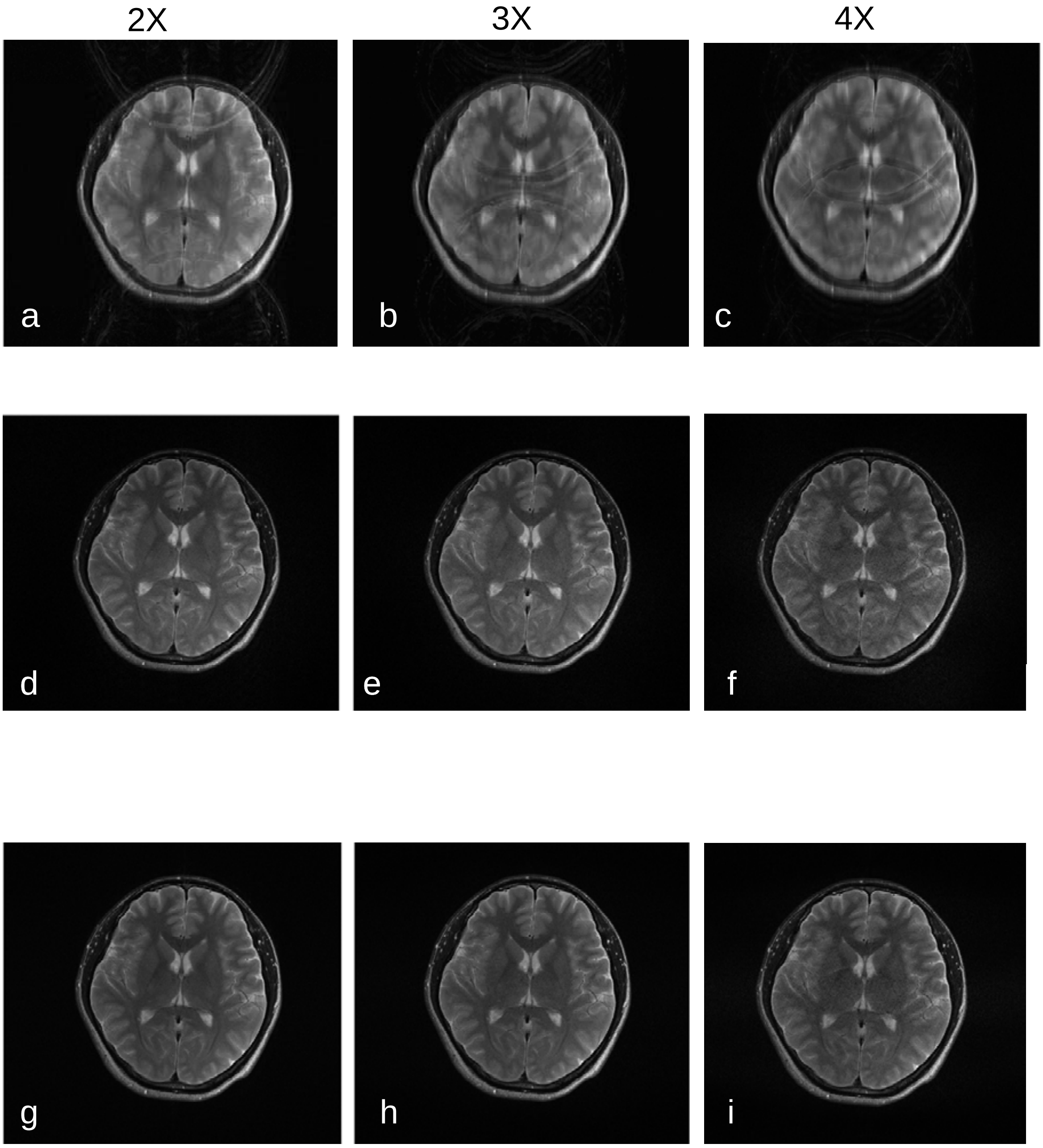

Fig. 3.9. In vivo head images with 2X, 3X and 4X acceleration. (a-c) Direct sum-of-squares combination of aliased images. (d-f) Synthetic target reconstructions. (g-i) GRAPPA reconstructions.

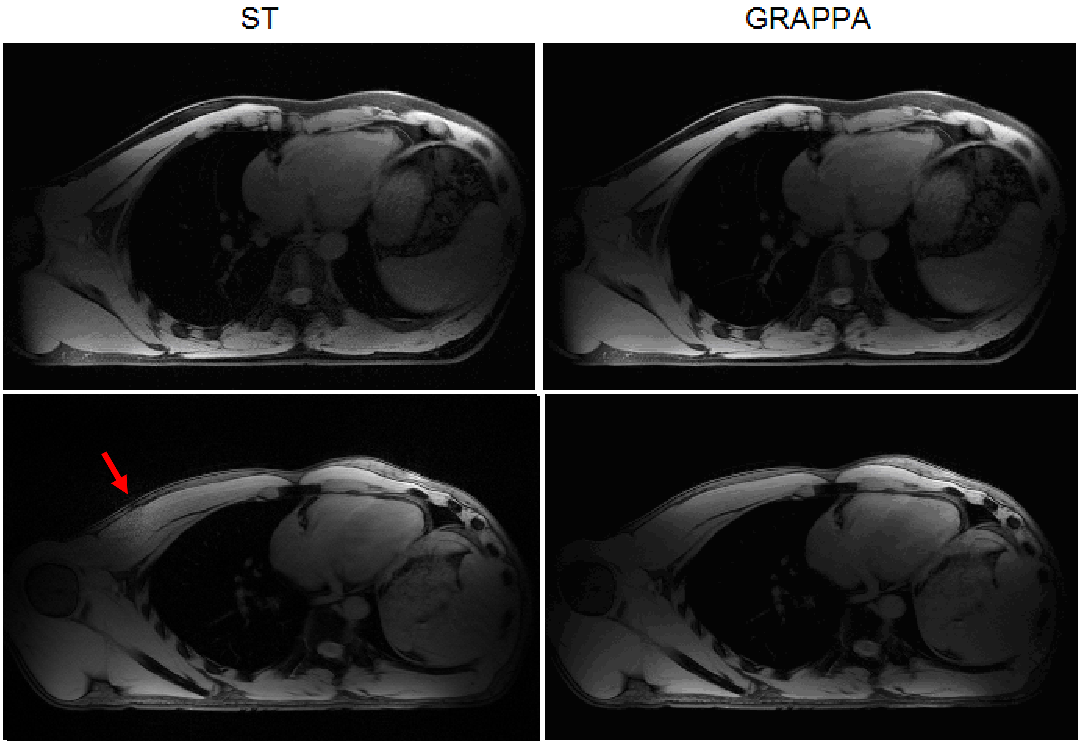

Fig. 3.10. Two sets of in-vivo RCA localization images acquired using a 32-channel coil and subsampled by a factor of 2. Images are reconstructed by the array-compressed synthetic target (ST) method and GRAPPA.

3.5 Discussion

In this study, the synthetic target method has been tested using various Cartesian datasets. Instead of generating unaliased coil images and combining them together, the final image is reconstructed by a linear combination of aliased coil images. The training and combination process is performed only once, so the computational time can be greatly reduced. Array compression can further accelerate the algorithm without causing severe quality degradation. The synthetic target method has been demonstrated to give results comparable to GRAPPA in all applications studied to date. However, the final image can suffer from some signal drop off in some cases. There are several possible improvements for the algorithm, as discussed below.

A data-driven fast reconstruction called Direct Virtual Coil (DVC) has been published by Beatty et al. [53]. The algorithm is similar to the synthetic target algorithm, but it is performed only in the k-space domain. In this method, low-resolution coil images are first combined to generate a target image. The image is then Fourier transformed and the resultant k-space data is treated as a “virtual coil” target in the training process. The training and the combination are based on the coil data in k-space using ARC [54]. DVC has been demonstrated to have no significant image quality difference with coil-by-coil techniques in high-resolution liver imaging [55] and time-resolved contrast-enhanced imaging [56]. The noise performance of DVC in background regions is even better [56]. In [56], DVC was able to achieve maximally a 15-fold speed up for 32-channel image reconstruction, while synthetic target achieves 30-fold speed up. This difference might be the result of the different synthesis process for the target images. A more complicated method was studied later for a smoother phase map, as discussed below.

3.5.1 Target image

One possible are of improvement for the synthetic target algorithm is in the choice of the target image. The magnitude of the target image can be easily obtained by a combination of unaliased low-resolution coil images. However, the image quality of the synthetic target method is also sensitive to the phase map of the target image. In our study, we found that water/fat and air/tissue interfaces can cause the phase in those regions to change rapidly, so that the unaliasing step in the synthetic target method cannot perfectly recover the original signal.

As a result, we may still need a low-resolution sensitivity map to acquire an accurate target image. Roemer’s method is designed to give an estimate of weighting masks and thus optimize the SNR when combining unaliased coil images. The tradeoff is that there is additional computation time required for fitting. However, in our study we found that this additional computation time was acceptable in practice. Beatty et al. have proposed another possible method to determine the phase of the target image [57]. In this region growing technique, image space is divided into multiple blocks that overlap each other. A linear combination of coil images in each block will generate a region of known phase. Then an affine phase matching step is applied to diminish the discontinuity between each block using overlapping area. This algorithm can be viewed as an extended version of adaptive reconstruction. A smooth phase map may minimize the effect of phase cancellation and thus remove the signal drop off in the final reconstructed image. However, the tradeoff is that the extra time used for region growing is several times longer than adaptive reconstruction, which could diminish the speed advantage of synthetic target. A better and simpler strategy to generate an accurate phase map for target images should be explored in the future.

3.5.2 Constrained optimization

Another remaining problem with the synthetic target method is in the training process. Since the number of the coefficients of each weighting mask is relatively small (about 5 for each coil), while the total points of each coil image are either 256×256 or 512×512, the optimization turns out to be an overdetermined estimation problem. We have used a regularization factor in this chapter to constrain the training. The value of this factor is different for every dataset. For in-vivo studies, we found that a larger regularization factor is needed to perform the unaliasing. However, there may be some signal loss in low SNR regions for larger regularization factors. Other than this concern, the method worked well for all of the datasets.

Other types of constraints could be added later to further improve the optimization process. Constraining the properties of the trained weighting masks is one possible approach. For example, the weighting matrix should be a low-frequency window-shaped mask. The condition could force the oscillation of the trained masks to be less than a certain level. Another approach is to enforce data consistency between the trained k-space line and the original k-space data. Iteration would be required with this approach, as in SPIRiT [8]. This approach would likely improve the optimization, but would also result in a decrease in reconstruction speed.

3.5.3 Parallel computing

In this exploratory study, all of our image reconstructions were performed in Matlab for maximum flexibility. Simply implementing the algorithm in a compiled language such as C++ would result in one or more orders of magnitude reduction in computation time, but this was outside the scope of this study and so we explored using the Matlab parallel computing toolbox to accelerate the image reconstruction. As shown in Table 1, it did reduce the computing time, but not significantly. There are other powerful tools to facilitate synthetic target reconstruction. MPI and openMPI are the most popular methods for parallel computing. The techniques are quite mature and there are open resources for MPI functions in both C and Matlab, so they could be easily incorporated into the original synthetic target code. Another possible method to further reduce reconstruction time is the use of a graphics processing unit (GPU). GPU computing has been used for a variety of image reconstruction algorithms [58,59,60]. According to [59], a GPU can increase the reconstruction speed by a factor of 22 for a 512×512 image for a compressed sensing reconstruction [61]. We anticipate that the use of some combination of these methods would make real-time synthetic target reconstruction practical.

3.6 Conclusion

We have developed a fast image reconstruction technique for Cartesian parallel imaging called the synthetic target algorithm. This algorithm was shown to give comparable results to coil-by-coil reconstruction methods. It reduces both the computation time and the memory of parallel iamge reconstruction. We also combined array compression with the original synthetic target method to achieve higher reconstruction speed. The synthetic target metjhod is capable of generating unaliased images for both brain and cardiac imaging. We observed some signal loss in low SNR regions, as in cardiac images. The algorithm could be improved with a more accurate target image and more constraints in the training.

Chapter 4

Improved Synthetic Target Image Reconstruction for non-Cartesian Trajectories

4.1 Introduction

Parallel imaging can be applied to non-Cartesian acquisitions to further reduce scan time. The non-uniform sampling pattern increases the difficulty of calculating missing data points in k-space. There have been a number of reconstruction methods published for non-Cartesian parallel imaging in recent years. Iterative SENSE [40] is a modified SENSE algorithm which is suitable for arbitrary trajectories. It includes trajectory information in the encoding matrix, and then iteratively unaliases the image using explicit coil sensitivities as in the original SENSE method. It requires accurate estimates of coil sensitivity and the reconstruction can be time consuming.

Auto-calibration methods such as GRAPPA cannot be directly applied to non-Cartesian k-space, because the distance between the samples varies; thus, the trained convolution kernel cannot be applied to every position. Intuitively, researchers have realigned each interleaf on a Cartesian grid [62] and performed GRAPPA on matched lines. This is easier to implement for radial trajectories than for spirals, because the transformation from spiral a trajectory to a Cartesian grid is not straightforward. GROG is another way to handle arbitrary trajectories. It trains the kernel and then uses kernel properties to correct for different sampling patterns at each position [63]. The tradeoff of this method is the required long computation time.

Spiral PILS [64] was studied by Hu et al., and it is a fast and straightforward method. The basic principle of spiral PILS is similar to Cartesian PILS: it uses Fermi window masks to suppress the aliasing resulting from undersampling [64]. We will show that it is suitable only for an acceleration factor less than three. Hu et al. proposed another algorithm called BOSCO [65], which trains the kernel and can conduct the unaliasing step in either the image domain and k-space domain; it has been shown to work for constant density spiral trajectories. BOSCO has computational time comparable to GRAPPA, which can be quite long for arrays with a large number of coils. Thus, we have modified synthetic target based on BOSCO to accelerate the computation, and this chapter describes the results with this approach.

The original synthetic target method has an assumption that the weighting masks trained in the center of k-space could later be used in all regions of k-space. This assumption is certainly true for Cartesian trajectories, since the sampling is uniform. For constant density spirals and dual density spirals, the sampling density is also uniform, and thus it roughly meets this assumption, as shown in Fig. 4.1 (a). For the variable density spiral trajectory of Fig. 4.1 (b), the spacing between interleaves linearly decreases from the center to outer regions of k-space, so the convolution kernel for each location varies significantly; thus, it does not meet the assumption. Radial trajectories (Fig.4.1 (c)) are similar to variable density spiral trajectories, but the spacing between radial spokes varies even more. We would expect that synthetic target might not be suitable for radial trajectories. Later in this chapter we will test synthetic target for constant density and radial trajectories, and discuss improvements that constrain the reconstruction process for better results.

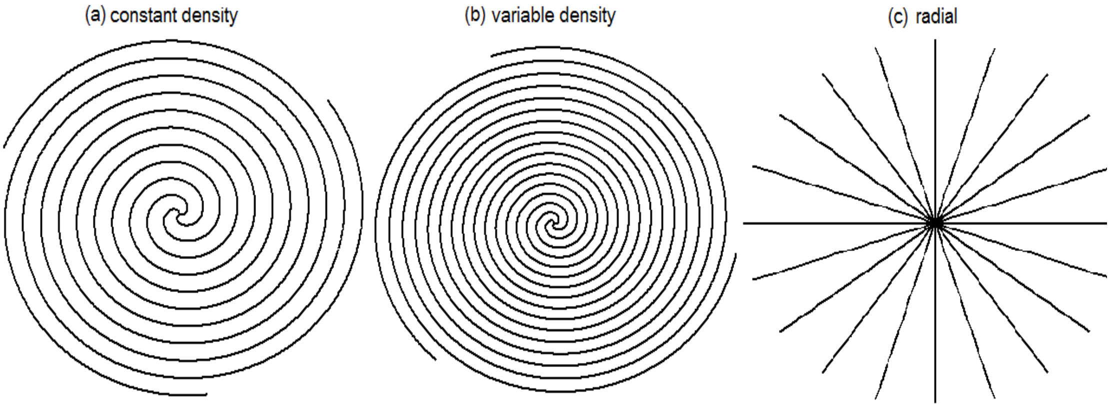

Fig. 4.1. Different types of non-Cartesian trajectories: (a) constant density spiral, (b) variable density spiral, and (c) radial.

4.2 Synthetic Target-PILS for Spiral Trajectories

4.2.1 Theory

PILS (Parallel Imaging with Localized Sensitivities) is a popular parallel imaging reconstruction technique with high SNR and rapid image reconstruction [44]. The first step in PILS is to determine a localized coil sensitivity mask for each coil based on fully sampled data. Typically, these masks are fit to a smooth function, such as a Fermi window. Then, these masks are applied to each coil image to remove aliasing, and the resulting unaliased images are combined. The idea of PILS is quite simple and efficient. However, PILS is only suitable when the coil sensitivity profile is smaller than the first sidelobe of the PSF [64]. Thus, it is especially useful when imaging with 32-channel arrays, where the coil sensitivity is localized. However, it works well only with a low undersampling rate. In this chapter we describe the combination of PILS with synthetic target parallel image reconstruction to permit higher acceleration factors than PILS and better SNR than synthetic target alone.

The algorithm is as follows: First, use the spiral PILS algorithm to automatically generate Fermi window masks [64]. Next, apply these masks to both the generated low resolution and the aliased high resolution coil images to suppress aliasing energy.

Finally, apply the synthetic target method to these modified aliased images to obtain the final image. This revised synthetic target reconstruction process can be expressed as

$$m_0(r) = \sum_{1}^{N_c} u_j(r)\overline{m_j}(r)w_j(r) \qquad [4.1]$$

which is similar to Eq. 3.6 except that $w_j(r)$ is the Fermi window mask for the j^{th} coil. Then we can train for the spatial weighting matrix as we did in the Cartesian case to minimize the following least square norm:

$$\left\| m_{0,t}(r) - \sum_{j=1}^{N_c} \overline{m}_{j,t}(r)u_{j,t}(r)w_{j,t}(r) \right\|_2 \qquad [4.2]$$

where j stands for the j_{th} coil. $u_{j,t}(r)$ is the low resolution spatial weighting matrix. $\overline{m}_{j,t}(r)$ are low resolution, aliased coil images. $m_{0,t}(r)$ is a composite full FOV low resolution image used as a target image. $w_{j,t}(r)$ are low resolution Fermi window masks. Combining PILS with synthetic target will help to further remove the aliasing. Applying masks will make the matrix sparser and increase the rank. Also it is equal to putting more constraints on the overdetermined estimation problem, and hence it helps to solve the optimization. We will compare the results of PILS alone, synthetic target alone, and synthetic target-PILS to see how much improvement it yields.

4.2.2 Experiments and results

We collected two datasets with a 32-channel coil on a Siemens 1.5T scanner, both with constant density spiral gradients. The readout gradient was 16 ms with 8192 samples. FOV = 280 mm, slice thickness = 5 mm, number of interleaves = 24, with undersampling factors of 2 and 4. BOSCO reconstruction was used to provide the reference images. We also performed PILS reconstruction and the combined synthetic target-PILS method.

The results are displayed in Fig. 4.2. For both datasets, PILS removes the aliasing when the acceleration factor equals to 2. The results suffer from undersampling artifacts for 4X cases. For dataset 1, the coils have a relatively smaller sensitivity profiles than the first side lobe of the PSF. Thus PILS gives better 4X image quality for dataset 1 than for dataset 2. The latter has more severe aliasing in the middle of image, and there is signal drop off near the heart.

Synthetic target removes undersampling artifacts in both datasets. However, comparing SyntheticTarget and ST-PILS results, we find that adding PILS reduces the MSE for both datasets. The effect of applying PILS masks is more evident for dataset 1, because the coil sensitivities are smaller in this dataset. As shown in Fig. 4.2, ST-PILS yields lower MSE than synthetic target and BOSCO for dataset 1. For dataset 2, the synthetic target image is somewhat blurred while the ST-PILS image has a better view of detail.

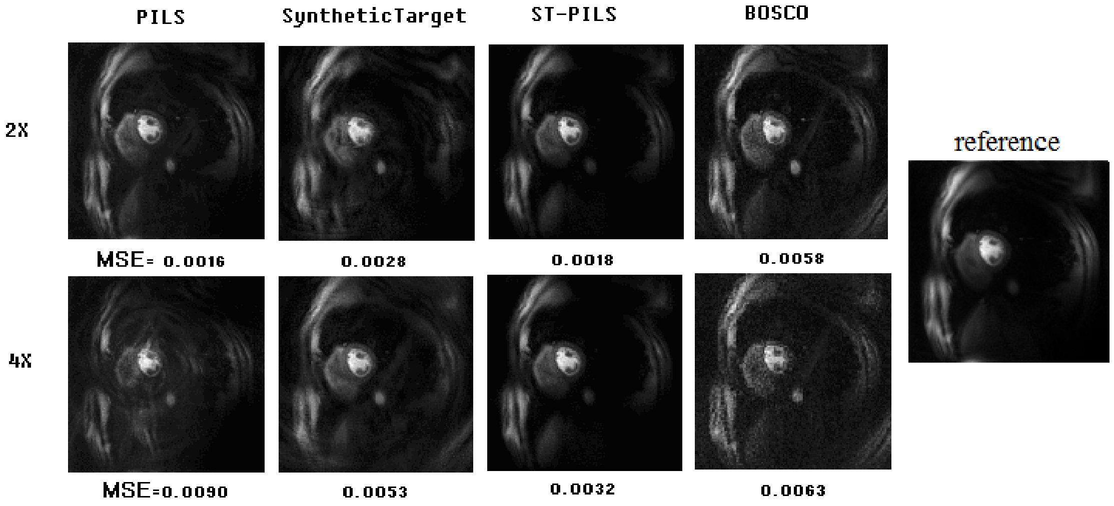

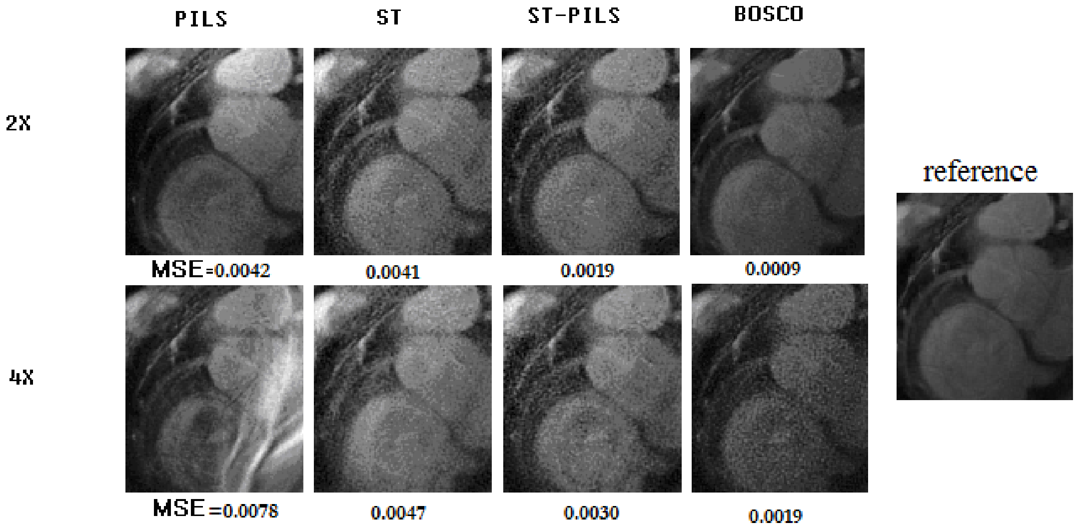

Figure 4.2: Reconstruction for two 32-channel spiral datasets using PILS, synthetic target, ST-PILS and BOSCO. The top row for each dataset shows results with an acceleration factor of 2 and the bottom row with an acceleration factor of 4.

4.3 Phase-Constrained synthetic target for radial trajectories

4.3.1 Theory

For non-uniform sampling patterns such as variable-density spiral and radial trajectories, convolution with an invariant k-space kernel may result in residual phase error in the target image. A phase-constrained term can be added to the training step to force the combination of low resolution images to be real. Phase-constrained reconstruction was initially used in partial Fourier parallel imaging [66]. It utilizes the data symmetry in k-space and sets the imaginary part of the image to be zero. An additional acquired phase map can be applied to increase accuracy [66,67]. We can use the same strategy in the process of training for the target image. The least square norm in Eq. 3.8 then can be written as follows:

$$\left\| m_{0,t}(r) - \sum_{j=1}^{N_c} \overline{m_{j,t}}(r) u_{j,t}(r) \right\|_2 + \lambda \operatorname{Im} \left\| \sum_{j=1}^{N_c} \overline{m_{j,t}}(r) u_{j,t}(r) \right\|_2 \qquad [4.3]$$

where j stands for the j_{th} coil. $u_{j,t}(r)$ is the low resolution spatial weighting matrix.

$\overline{m_{j,t}}(r)$ are low resolution, aliased coil images. $m_{0,t}(r)$ is a composite full FOV low resolution image used as a target image. We set the phase to zero in the following studies. The second term is used as a phase constraint. The empirical value for λ is 10^{-2}. Any acquired or estimated arbitrary phase map $P_{0,t}(r)$ with unity magnitude could be combined in the least square norm for a more accurate reconstruction.

4.3.2 SPIRiT

SPIRiT [8] was proposed as a novel parallel imaging reconstruction tool in 2010. It is a coil-by-coil, self-calibration algorithm that is suitable for generalized trajectories. The idea of SPIRiT reconstruction can be stated as follows [8]:

$$\begin{array}{ll} \min & \|(G-I)x\|^2 \\ s.t. & \|Dx-y\| \le \varepsilon \end{array} \qquad [4.4]$$

x is the fully sampled kspace data vector from all coils that we want to solve for. y is the actual acquired k-space data from all coils. The first term stands for the consistency with calibrations. G is the convolution operator trained in the fully sampled center of kspace. The method assumes that by applying a convolution operator G to neighboring points, we will get the same k-space data [8]. The second term stands for the consistency with data acquisition. D is the operator that maps x to the acquired data y. The term is suitable for all trajectories. If y is non-Cartesian data, D involves interpolating data to non-Cartesian locations [8].

SPIRiT uses conjugate gradient or projection over convex sets (POCS) algorithms to iteratively solve the optimization problem. Typically it takes 10-30 iterations before reaching the result. The algorithm can be performed in either k-space or image space. It has been shown to be able to generate good results for Cartesian and spiral trajectories. The results have been reported to have less error than GRAPPA, because data consistency is applied [8]. In our work, we used SPIRiT as a comparison algorithm for the phase-constrained synthetic target method. In Chapter 6, SPIRiT is also used as the parallel imaging reconstruction technique in the coronary artery wall studies.

4.3.3 Experiments and results

We have tested synthetic target's performance on radial data. Radial phantom data was acquired using a 1.5T Siemens Avanto scanner and 12-channel coils. 192 lines were collected, each with 384 samples. Since BOSCO does not work well with radial data, we use SPIRiT [8] as the reference algorithm. And also, we tested the performance of the phase-constrained synthetic target method. The reconstruction was performed on a dual-processor computer with 2.8GHz Intel Xeon CPUs. The reconstruction code was written in Matlab.

As shown in Fig. 4.3, for both the 2X and 4X cases, the original synthetic target images have severe aliasing in the object region. The uneven signal intensity may come from the inaccurate phase map generated for the final image. The noise level in the background is high. With the phase-constrained method, most of the noise and the aliasing have been removed and the resultant images have better quality.

The image on the right is presented as a reference image, which is obtained using SPIRiT. The quality in the images reconstructed using SPIRiT can be improved with more iterations. The tradeoff is a small loss of resolution in some cases. In this study we choose the iteration number to be 50. It takes about 50s for SPIRiT to reconstruct the 256×256 image, while for SyntheticTarget it takes about 11s.

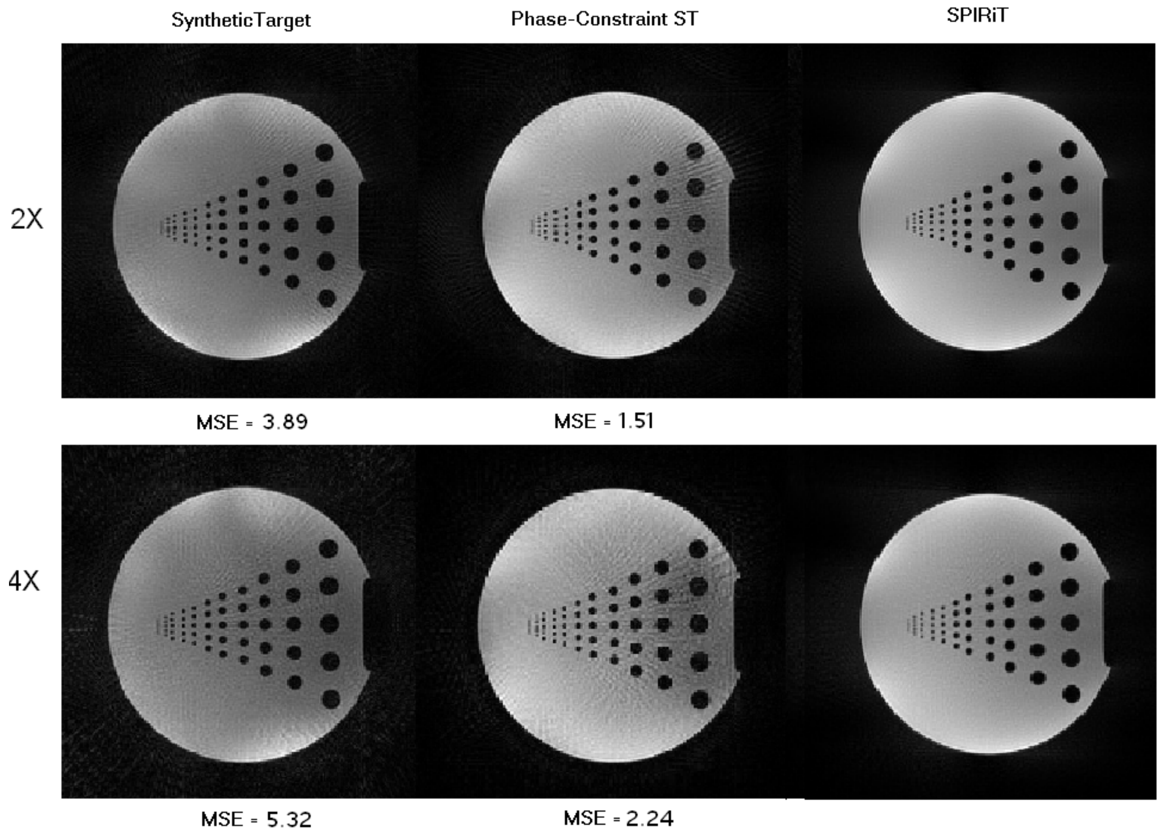

Fig 4.3: Reconstruction of 12-channel radial dataset using synthetic target, phase-constrained synthetic target and SPIRiT

4.4 Discussion

Synthetic target is capable of removing undersampling artifacts for constant density spirals. It is especially useful when combined with PILS for reconstructing 32 channel data. For radial data, phase-constrained synthetic target may help the degradation of reconstructed image to some level; however, it does not achieve results comparable to SPIRiT. One possible reason is that the PSF for a radial trajectory is more complex and the aliased energy is harder to remove using a non-iterative reconstruction. A more complicated strategy could be used for variable density spiral and radial trajectories in future studies.

4.5 Conclusion

We have tested synthetic target methods on constant density spiral and radial trajectories. PILS masks and zero phase maps were added as constraints for improving the performance of synthetic target. For a constant density spiral trajectory, ST-PILS can generate images with good quality compared to BOSCO. For a radial trajectory, phase-constrained synthetic target can remove the aliasing to some extent.

Chapter 5

DANTE Preparation for 2D Coronary Artery Wall Imaging

5.1 Introduction

Coronary artery disease is a leading cause of death. MR coronary angiography and other whole-heart studies have been powerful tools to detect coronary artery stenosis [27]. However, it is also valuable to image the coronary wall and the remodeling process in order to diagnose the first stages of atherosclerosis. For coronary wall imaging, black blood techniques are typically used to null the blood signal in the coronary lumen. Double inversion recovery (DIR) pre-pulses combined with ECG gating are typically used in current coronary wall studies for black blood imaging [1]. This method generates high contrast between coronary wall and lumen and preserves signal in the tissue. It can be integrated into all types of coronary imaging pulse sequences, such as GRE, FSE and SSFP.

DIR still has some limitations, especially for multi-slice scans. First, the inversion time is usually more than 600 ms for 3T studies, because of the long T_1 of blood. This leaves less time for imaging in one heartbeat and therefore constrains the imaging coverage. Second, the optimal delay time calculated to completely null the blood is only suitable for a single slice, unless multiple re-inversion pulses are used [68]. That increases the complexity and execution time in the sequence. Finally, the contrast of the coronary artery wall is highly sensitive to the motion of the vessel. Typically, the imaging module is placed in mid diastole, when the RCA moves less [13]. However, there are cases when the rest period happens early in the heart cycle. Then, the time between the R wave and the start of rest period will not be sufficient for blood signal to return to zero. DIR will not work as well in these patients. Ideally, imaging should occur during the rest period and TI should be set optimally, but that is hard to achieve when using DIR.

There are other possible black blood techniques besides DIR that can shorten the preparation time. One technique is phase-sensitive inversion recovery (PSIR), which does not require the blood signal to return to zero before data acquisition [34]. The contrast is enhanced by preserving the phase information in the lumen during image reconstruction. The TI can be shortened to 150ms using this method, so it is suitable for multi-slice imaging [34]. However, PSIR requires one magnetization-prepared and one imaging scan, which increases scan time. Misregistration is a potential source of error. And, since it relies on phase information, phase error induced by flowing blood must be carefully addressed.

Motion-sensitized driven equilibrium (MSDE) [11] is another black blood imaging method, which was first used for carotid artery studies. The simplest version of MSDE uses one 90-degree excitation pulse at the beginning, followed by a 180-degree refocusing pulse and another 90-degree pulse to restore the magnetization to the z axis. Spoiling gradients are placed between the pulses on three axes to suppress moving material. The performance of MSDE is sensitive to B1 inhomogeneity, especially at 3T. It also suffers from signal loss caused by T_2 decay and eddy currents. An improved version called iMSDE [69] was developed to preserve vessel wall signal, and it has been used for coronary artery wall imaging [70].

DANTE [5] is a novel black blood technique that can achieve a higher contrast-to-noise ratio (CNR) while maintaining a signal-to-noise ratio (SNR) similar to DIR. We hypothesized that this method would be suitable for coronary wall imaging, especially because of the relatively slow coronary blood velocity. The total duration of

DANTE is less than 300 ms, which makes it more flexible for imaging during the rest period. The flip angle used in DANTE is low, it is robust to field inhomogeneities and the signal loss will be less than with MSDE. In this chapter, we will discuss how we combined DANTE pulses with gating and our current spiral coronary sequences to evaluate its performance; we will show that DANTE gives comparable SNR and CNR to single-slice DIR but with more flexible timing of the imaging readout. DANTE prepulses are especially suitable for multi-slice coronary artery wall imaging. Also we will discuss the choice of DANTE parameters and the influence of heart movement on DANTE blood suppression.

5.2 Methods

5.2.1 Review of DANTE prepulses

As shown in Fig. 5.1, DANTE preparation consists of a series of non-selective pulses, with phase alternating RF spoiling [5]. The prepulses are often placed along the flow direction, with spoiling gradients between pulses. During the execution, flowing spins are spoiled because of the phase increment induced by velocity. Meanwhile, most of the signal from stationary spins is preserved, because the flip angle of the pulses is less than 15°. The contrast between stationary and flowing spins is thus enhanced.

It should be noted that the signal attenuation ratio of flowing spins is not proportional to velocity. The blood signal will be fully spoiled as long as the velocity is above 0.1cm/s with typical parameters [5], which is a lower threshold from MSDE and makes DANTE especially suitable for coronary imaging. The performance of DANTE largely depends on the choice of parameters, which are based on the relaxation times of tissue and blood. In the carotid study conducted by Li et al., the DANTE parameters were chosen as follows: number of pulses = 64, flip angle = 7, duration between pulses = 1ms, gradient amplitude = 18mT/m [71]. We will discuss the simulation of parameters for 3T coronary wall imaging in the next section.

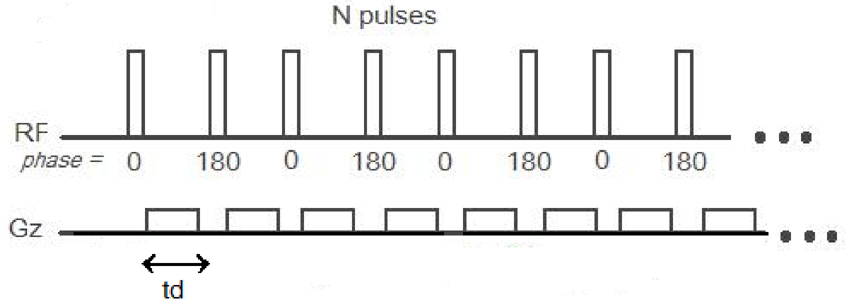

Fig. 5.1. DANTE prepulse module. A train of low-flip-angle, phase-alternated RF pulses with flow spoiling gradients interspersed suppresses signal from flowing blood while largely preserving the magnetization of static spins.

5.2.2 Numerical simulation of DANTE parameters

There are four parameters that determine the performance of DANTE: number of pulses N_p, interval between pulses t_d, flip angle of pulses α, and amplitude of spoiling gradient G_z. As stated in [5], the magnitude of stationary signal $M_{s,z}$ at the end of the RF pulse train can be expressed by the following equation:

$$M_{s,z} = E_{1,app}^{n}(M_{ini,s,z} - M_{ss,z}) + M_{ss,z} \qquad [5.1]$$

$$M_{ss,z} = \frac{(1+E_1\cos\alpha)(1+E_1)}{1-E_{1,app}^2}$$

$$E_{1,app} = \sqrt{E_1^2\cos^2\alpha - E_1E_2\cos\theta\sin^2\alpha}$$

where $E_1 = \exp(-t_d/T_1)$, $E_2 = \exp(-t_d/T_2)$, θ is the phase dispersion induced by the spoiling gradient, and $M_{ini,s,z}$ is the initial magnitude of the static tissue. Similarly, we have the following approximate equation for $M_{m,z}$ [5] :

$$M_{m,z} = E_{1,app}^{n}(M_{ini,m,z} - M_{sm,z}) + M_{sm,z} \qquad [5.2]$$

$$M_{ss,z} = \frac{1-E_1}{1-E_1\cos\alpha} M_0$$

$$E_{1,app} = E_1 \cos\alpha$$

$M_{ini,m,z}$ is the initial magnitude of the moving signal. During the execution of DANTE, we are assuming that the moving spins are fully spoiled. So, the phase dispersion term θ does not appear in the final expression. Moreover, $M_{m,z}$ does not depend on the flow velocity either, as long as the signal is fully spoiled, which implies the performance of DANTE is flow insensitive.

In [5], G_z was chosen to be 5 mT/m for single slice imaging and 6 mT/m for 3D imaging. In our study we set G_z to be 6 mT/m. Other parameters were simulated based on this value.

We will discuss the influence of the interval between pulses first. The magnitude decays at a rate T_{app}, and T_{app} is defined by the following expression [5]:

$$1/T_{app} = -\ln(\cos\alpha)/t_d + 1/T_1 \approx \alpha^2/2t_d + 1/T_1 \qquad [5.3]$$

Equation 5.3 implies the decay rate of flowing signal is inversely proportional to t_d. Shorter t_d means the dephasing of static signal will be less, which should lead to a higher overall SNR. Thus in our experiments, we chose t_d to be 0.5-0.6 ms.

It should also be noted that in Eq. 5.3 the decay of flowing signal is proportional to the flip angle α. However, a large flip angle will also cause the static signal to drop off. Similarly, increasing the number of pulses N_p will attenuate both stationary and flowing signal. To find the parameter that leads to the best CNR and SNR, we assumed the contrast between stationary and moving spins to be $M_{s,z} - M_{m,z}$ and conducted a numerical simulation. We used the T_1 and T_2 values of blood and vessel wall at

3T: $T_{1,motion} = 1550ms$, $T_{1,static} = 1115ms$, $T_{2,static} = 47ms$ [72], and $M_{ini,m}, M_{ini,s} = 1$, $t_d = 0.5ms$. A plot of contrast and moving signal are shown in Fig. 5.2 as a function of the number of pulses. Simulations at different flip angles are shown in different colors.

In Fig. 5.2 (a), the suppression of blood improves at larger flip angles, which matches our intuition. When the flip angle is less than 7 degrees, the suppression of moving signal is not sufficient. However, the static signal drops severely drop as the flip angle increases, as in Fig. 5.2 (b). So, we chose a flip angle of 7 degrees for our experiments to achieve a balance between preserving tissue signal and nulling blood. N_p was set to 400-500, which yields high contrast, as shown in Fig. 5.2 (c), while most of the blood signal is suppressed, as shown in Fig. 5.2 (a).

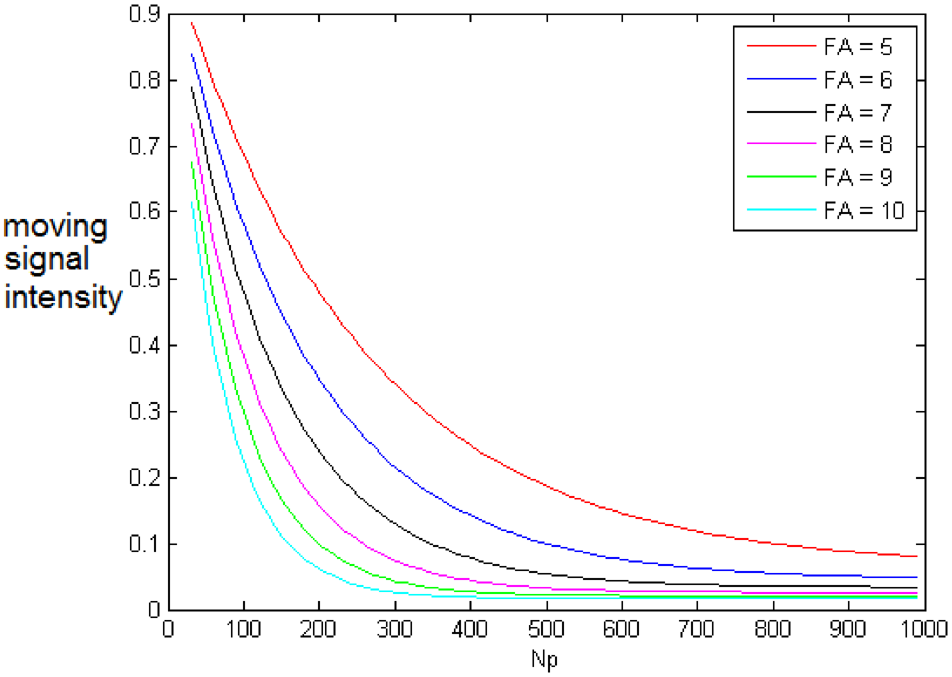

(a)

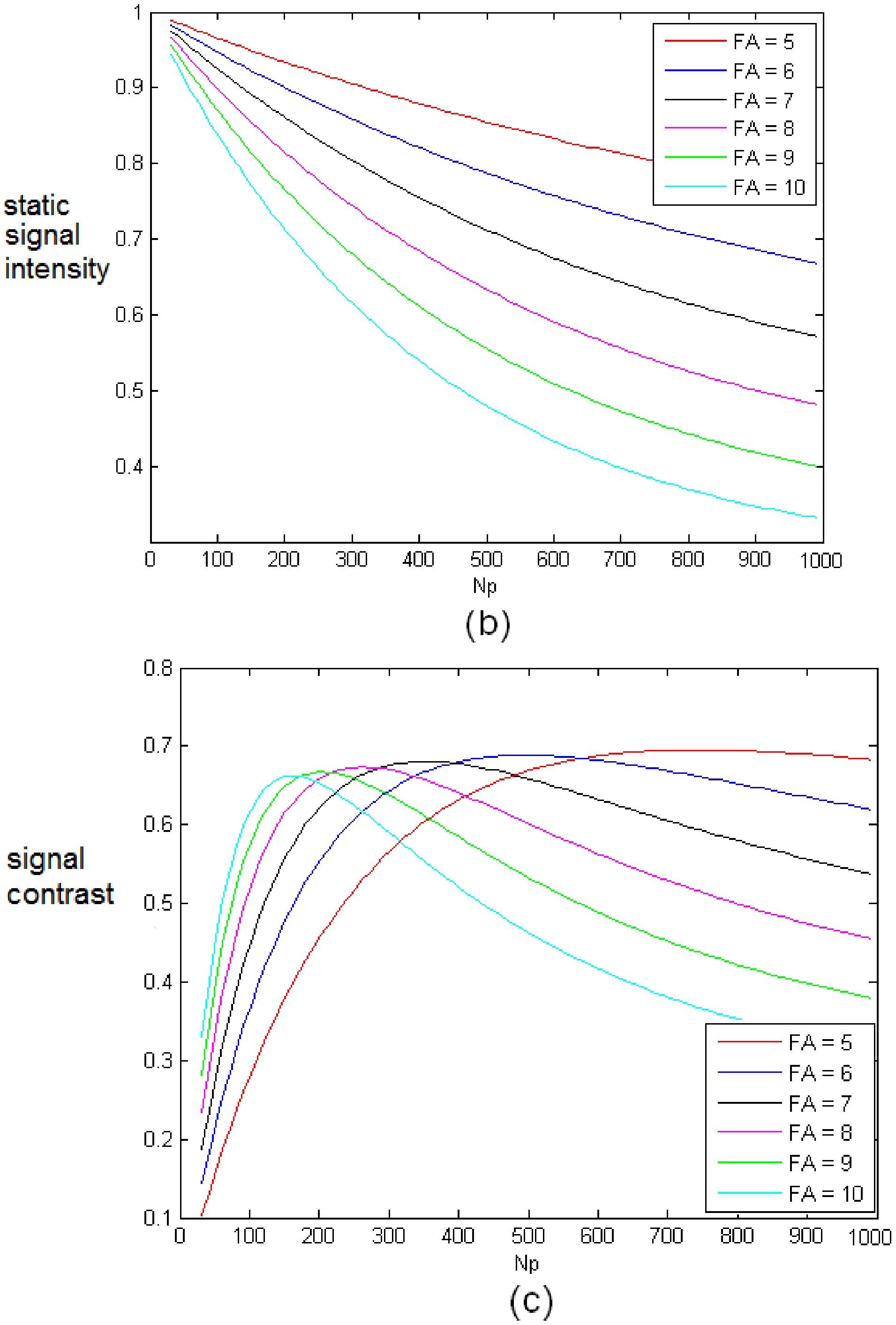

Fig. 5.2. Numerical simulations of (a) moving spins only, (b) static signal only, and (c) contrast between static and moving spins with DANTE preparation. The flip angle of the DANTE prepulses varies from 5 to 10 degrees and the number of pulses varies from 1 to 1000.

5.3 Material and Methods

5.3.1 Materials

All of the experiments were performed on a Siemens 3T Trio scanner, with a 32-channel body coil array. The maximum gradient amplitude of this scanner was 45 mT/m and the maximum slew rate was 200 mT/m/s. Seven volunteers (ages 27-34, all male) were imaged using the methods described below.

After a scout scan of the heart, a gated breath-held 2D single-slice spiral GRE sequence was used to acquire white-blood in-plane images of the left and right coronary arteries. Typical localization images are shown in Fig. 5.3. The white rectangle represents the center imaging slice, which is placed between the proximal and mid portions of the RCA and LAD, orthogonal to the arteries. The multi-slice slab for the DANTE sequence is 15-25 mm thick. That typically covered the entire mid portions of the RCA and LAD. A cine trueFisp sequence was then placed in the same location to determine the in-plane coronary wall movement during heart cycle. The start time of the rest period was then used to calculate the optimal delay time for the subsequent coronary wall imaging sequences.

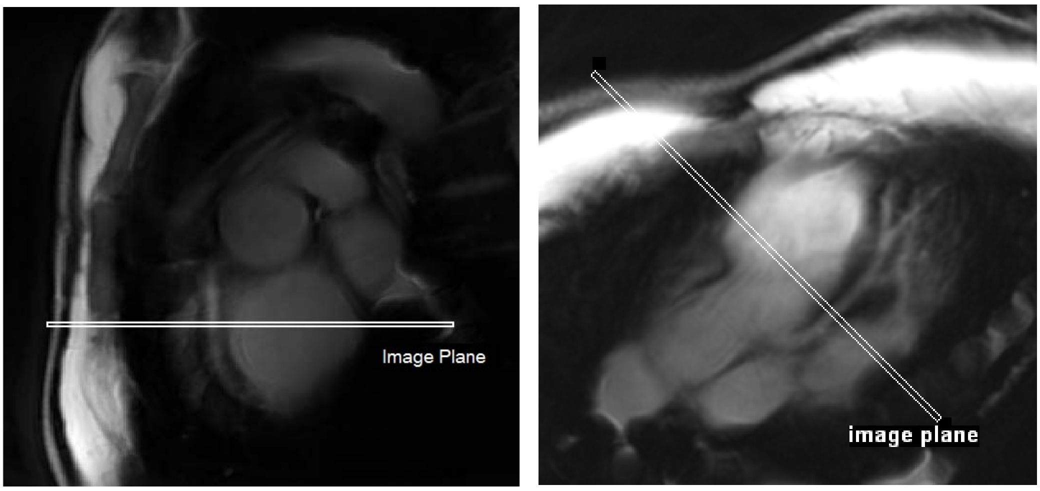

(a) (b)

Fig. 5.3 In-plane white-blood scout images of the right (a) and left (b) coronary arteries. The location of the center image slice is shown by the white rectangle.

5.3.2 Sequence design

Two protocols were used to test the performance of DANTE sequences for cross-sectional imaging of the RCA and LAD. One protocol was a 2D multi-slice spiral gradient-echo sequence combined with gating. After detection of the R wave and a delay time, a 5-ms spectral-spatial pulse was used for excitation, followed by a 16-ms constant density spiral readout gradient. Other imaging parameters were set as follows: FOV = 280-300mm, 14 interleaves, 5-mm slice thickness, in-plane resolution 0.8-0.9mm. Total scan time was 16 s. A diagram of the sequence is shown in Fig. 3.4 (a).

A simulation of the Mz magnitude during sequence execution is shown in Fig.3.4 (b). For the simulation, we chose $N_p = 500$, $\alpha = 7^\circ$, $t_d = 0.6\ ms$, which were the parameters used in our experiments. $T_{1,motion} = 1550ms$, $T_{1,static} = 1115ms$, $T_{2,static} = 47ms$. Because we are gating every heartbeat, the TR is set to the R-R interval and the numerical simulation is performed so that the initial magnetization $M_{ini,m}$ and $M_{ini,s}$ do not return to M_0. Thus, the simulation results are slightly different from the results showed in [5]. We can see that there is extra contrast induced by DANTE preparation besides the contrast caused by different recovery rate in both sequences. The blood signal will be suppressed to less than 10% after DANTE pulse execution. Note that the signal loss is approximately 10% for static spins. We verify these simulation results with experimental results described below.

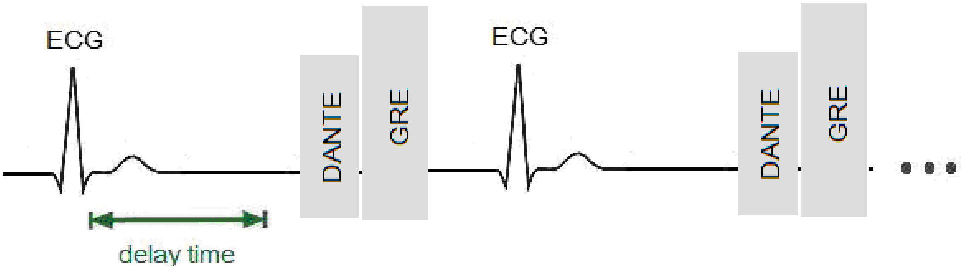

(a)

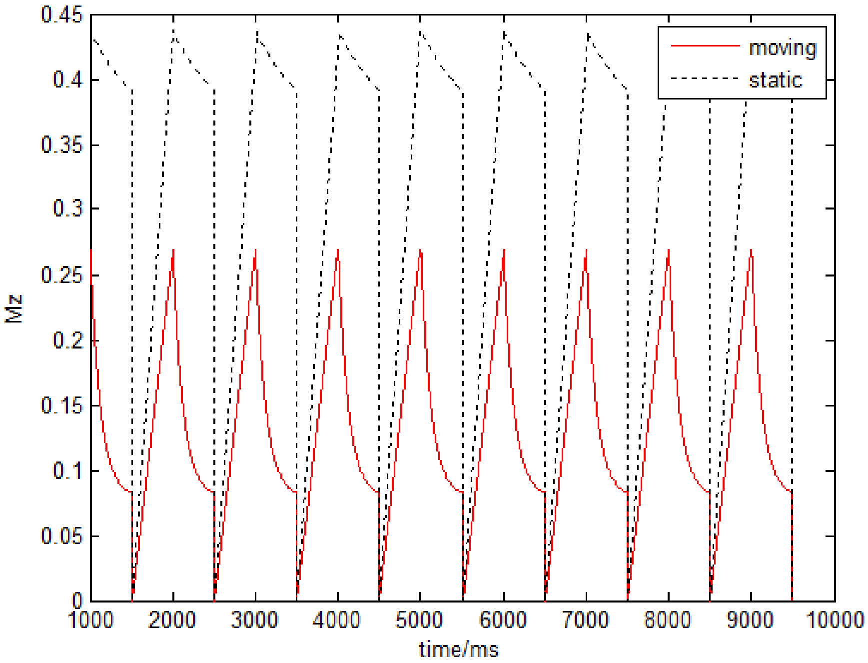

(b)

Fig. 5.4. (a) Schematic of DANTE 2D spiral GRE sequence with gating. (b) Simulation of the longitudinal magnetization static and moving spins during a gated DANTE GRE sequence.

5.3.2.1 DIR preparation

A 2D gradient echo sequence with DIR and gating was used to collect images for comparison with DANTE results. In the sequence, we used the same set of sequence parameters as with the DANTE sequence described before. Theoretically, DIR can yield the highest SNR and CNR of the current blood suppression techniques, since the blood signal will return to 0 if the inversion time is chosen carefully [1]. However, sometimes the optimal TI cannot be achieved even in single-slice scans. One possible reason is the conflict between the imaging window set by the rest period and the optimal inversion time. When subjects have a long RR interval, the required TI can be as long as 700 ms at 3T, while the subject's coronary rest period can be about 500ms after the R wave. In this case, there is not enough time for the blood signal to return to zero when imaging in the rest period window. The blood suppression will then be incomplete, and residual blood signal will lower CNR. DANTE can eliminate this conflict. The delay time of the DANTE sequence can be arbitrarily chosen, as long as it is larger than the DANTE execution time, which in our experiments is 300 ms. Considering that the rest period is usually in mid-diastole, the delay from the R wave to the imaging module will be more than 300 ms in most cases [13].

There are other factors that may affect the performance of DIR, such as flow velocity and flow patterns, while DANTE is insensitive to all of these factors [71]. In [71], DIR yielded higher SNR than DANTE for carotid imaging, yet CNR for the two methods was similar. And, since DANTE is suitable for multi-slice imaging, the overall time efficiency will be increased while contrast will not be sacrificed.

5.3.2.2 Image reconstruction and statistical analysis

Semiautomatic off-resonance correction using a Chebyshev approximation for fast conjugate phase reconstruction [73] is built into our on-line image reconstruction algorithm, after standard gridding of the spiral data. It is used for the correction of blurring from off resonance caused by B0 inhomogeneity and concomitant gradient fields, which is crucial when using long spiral readouts at 3T. The algorithm requires two additional acquisitions to generate a low-resolution field map. The map data is then used by the semiautomatic method to estimate a high-resolution field map. The final field map is then used for correction of the final image. The whole reconstruction process is performed slice by slice, and it takes about 10s for a 512×512 image on the scanner.

SNR and CNR were calculated and compared for corresponding slices acquired using the DANTE and DIR sequences. We measured the signal intensity of myocardium S_{myo} , left ventricle chamber S_{cham}, coronary wall S_{wall} and coronary artery lumen S_{lum} for all images. The standard deviation of noise N was measured in a region near the chest wall in each image. The contrast for the left ventricle and the coronary artery were defined as $C_{LV} = (S_{myo} - S_{cham}) / N$ and $C_{wall} = (S_{wall} - S_{lum}) / N$, respectively. Mean and standard deviation of measured SNR and CNR were calculated over all seven subjects, with an ROI defined for each subject.

5.4 Results

5.4.1 DANTE and DIR comparison

Cross sectional views of the RCA and LAD in the same volunteer are shown in Fig. 5.5. Images acquired by both DANTE and DIR sequences are presented for comparison. The slice location is the same for each pair. In RCA images, blood flow in all heart regions is successfully suppressed, which means that in this case, DANTE nulls the blood in not only the coronary artery, but also the heart chambers. The DIR image has motion blur in the coronary wall and adjacent myocardium, while the same part in DANTE image is sharp and clear, because the optimal delay time to image in rest period can always be achieved using DANTE. That significantly reduces motion artifacts.

There was a similar effect in LAD images, where the DANTE images had better blood suppression inside the coronary lumen and the coronary wall was sharper.

However, for the left atrium and ventricle, the residual blood caused more blur than in DANTE-prepared LAD images than in RCA images, especially in the atrium. One possible reason is that DANTE prepulses are direction-oriented. DANTE works best when the preparation gradient is along the direction of flow, which is always the case for blood in the coronary artery. So for all RCA and LAD images, the coronary wall should be free of residual blood. But for the heart chambers, especially the left atrium, the flow pattern is more complicated and residual flow in the image plane may cause some artifact. This is worse in LAD images, since the atrium is seen in close to a sagittal view and there is more blood inside the imaging slice. The flow artifact is also patient-specific, according to our studies.

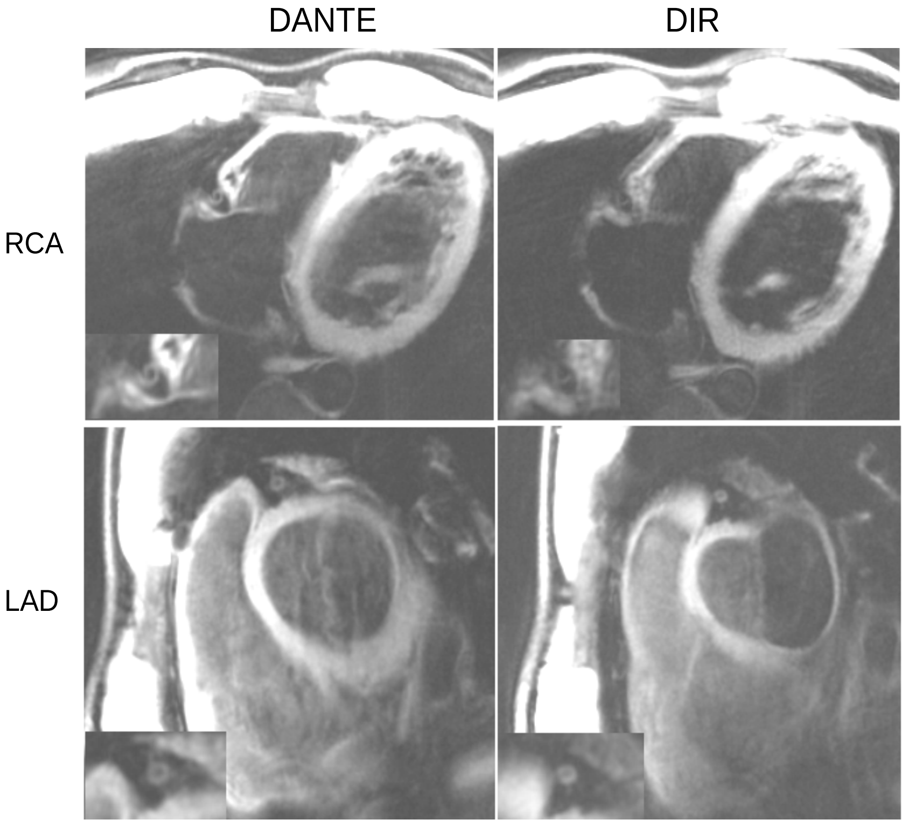

Fig. 5.5. Cross sectional images of the RCA and LAD, acquired by DANTE and DIR sequences.

5.4.2 Multi-slice DANTE imaging of RCA and LAD

Figure 5.6 shows RCA and LAD images acquired by DANTE prepared sequences. In both cases we are imaging three 5-mm slices, and the total slab is then 15 mm. DANTE successfully suppresses coronary blood flow in all the slices. In the DANTE module, the low flip angle pulses are non-selective, which makes DANTE able to null the blood in the entire artery, as long as the flow is in the direction of a spoiling gradient. In each heart cycle, one DANTE module is sufficient to suppress blood in the whole imaging slab, because the longitudinal magnetization of the blood recovers very slowly at 3T. According to our experience, the slice number can be increased to five without sacrificing too much contrast. Moreover, DANTE takes less time than DIR, which leaves enough time for imaging more slices.

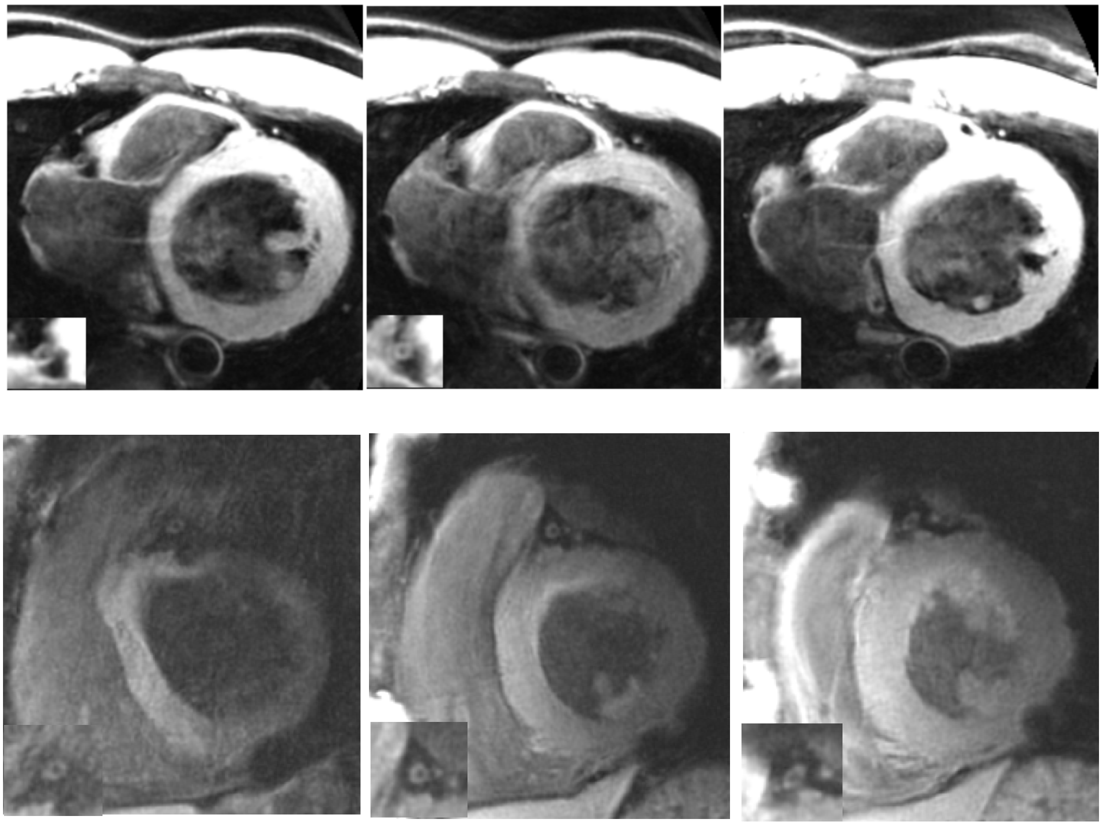

Fig. 5.6. Multi-slice results of DANTE images of the RCA (top) and LAD (bottom).

5.4.3 In-vivo validation of simulations

We performed experimental verification of our DANTE parameter simulations. RCA images with N_p changing from 200 to 600, flip angle = 7 degrees, pulse interval = 0.6 ms, and spoiling gradient amplitude = 6mT/m are presented in Fig. 5.7. Coronary wall regions are zoomed in for better visualization. Inn (a), blood suppression in the left ventricle and coronary artery lumen improved as N_p increases; however, for N_p = 400, 500 and 600, there was not much difference in blood suppression in the chamber and wall. The wall signal drops significantly with larger N_p, especially for N_p = 600. The best contrast was achieved with N_p = 400, where blood suppression and wall signal preservation reaches a balance for this particular case. Since the blood volume is different for different subjects, some subjects require larger suppression. We chose N_p = 400-500 for all of the following experiments.

Mean signal intensity of coronary lumen blood pool and coronary wall were measured and normalized. Final values are plotted in (b) and (c), to show the in-vivo attenuation of moving and static spins. Numerical simulation were also calculated according to Eq. 5.1 and Eq. 5.2 with the same parameters and plotted in (b) and (c). There is good agreement between experimental and simulation blood suppression, as in (b). Unlike the carotid artery study described in [5], in-vivo static spins experienced more attenuation than predicted by the simulation, with a signal drop off of about 10%. This is likely due to movement of coronary arteries during the DANTE pulse train. When N_p gets larger, the signal loss becomes more severe.

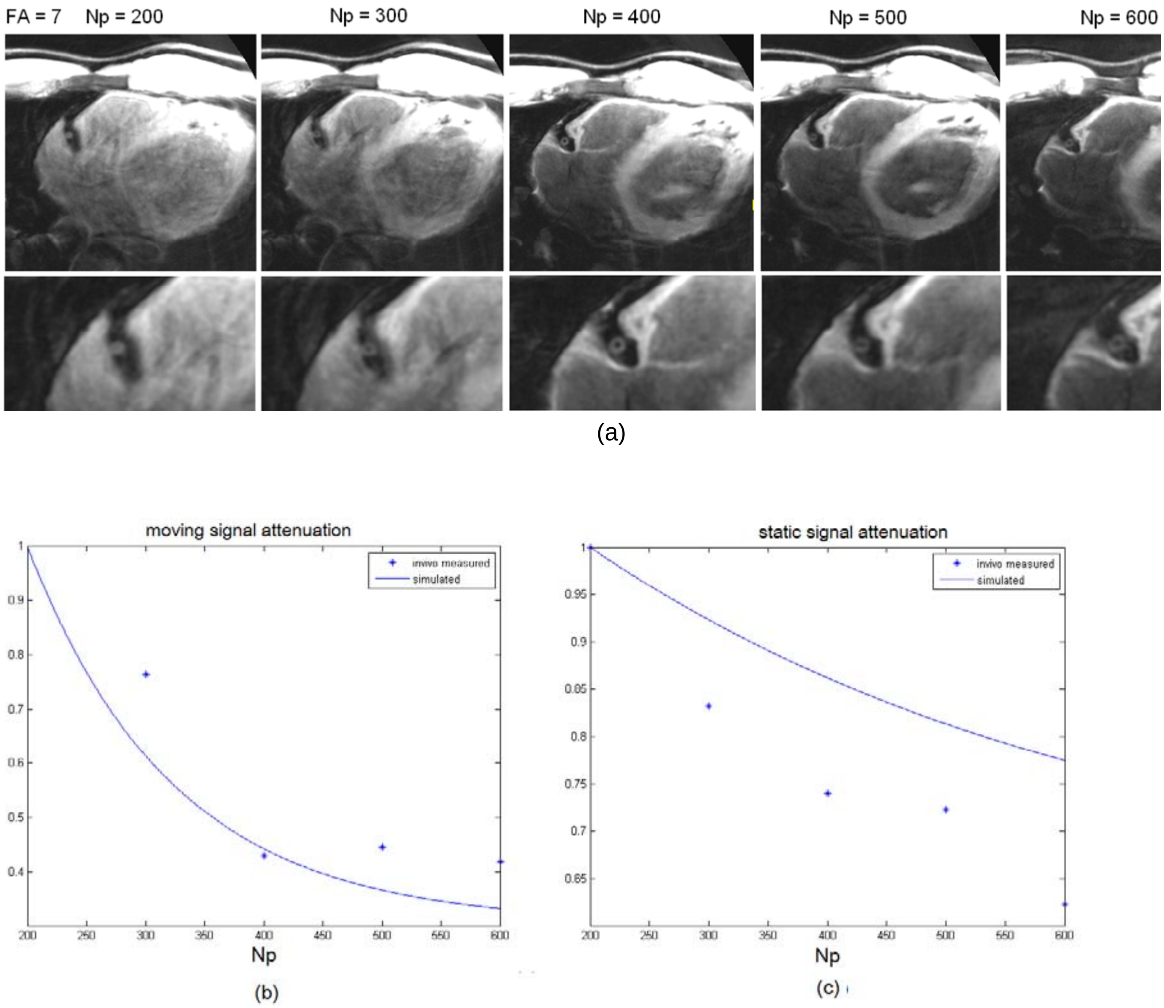

(a)

(b)

(c)

Fig. 5.7. (a) RCA wall images acquired with DANTE preparation, with NP = 200, 300, 400, 500 and 600 and flip angle = 7 degrees. (b) Simulated and experimental signal attenuation of moving spins using DANTE preparation. (c) Simulated and experimental signal attenuation of static spins using DANTE preparation.

5.4.4 DANTE for imaging in early diastole

Imaging during the rest period of the coronary arteries is crucial in our study, since motion blur and artifacts could be severe and damage image quality. However, for some patients whose rest period occurs in the early mid-diastole, the optimal TI for a DIR preparation and the start time of rest period cannot be satisfied at the same time. Figure 5.8 show in vivo results using both DIR and DANTE that illustrate this effect. Figure 5.8 (a) shows a DIR image with the inversion time set to ~500ms. The coronary artery is relatively stationary then, but the inverted blood signal has not returned to zero at that time point. Thus, in the image, the coronary wall is clear, but appears thickened because of the residual blood. Similar results can be seen in the atrial and ventricular chambers. In Fig. 5.8 (b), the blood suppression in the chambers is better because a longer inversion time is applied (~700ms). However, the RCA wall is blurred due to in-plane vessel motion. A DANTE sequence can successfully balance the two factors to achieve an optimal delay time, since it does not require a long inversion time to null the blood. The imaging strategy is more flexible and robust. As shown in Fig. 5.8 (c), DANTE can generate an image with better black blood suppression in all heart regions, while yielding a sharp and clear view of the coronary wall. These results suggest that DANTE is especially suitable for patients with an early rest period.

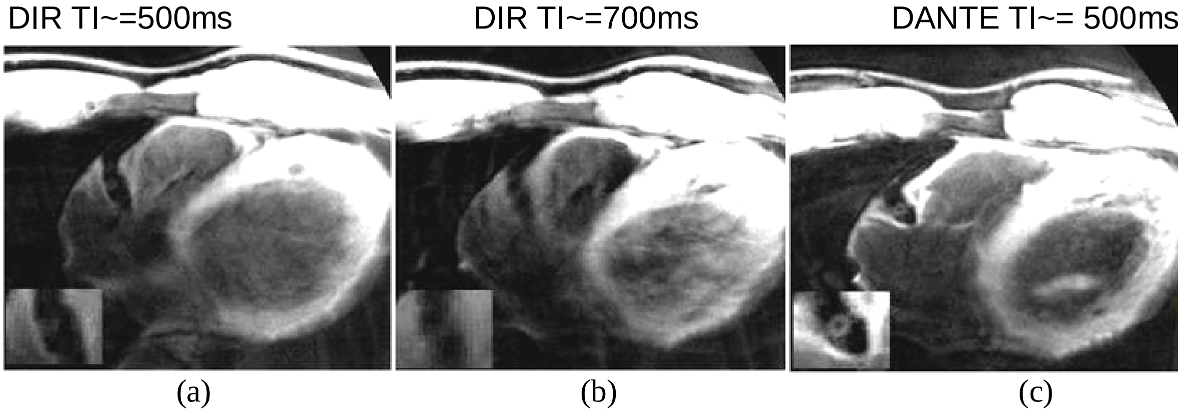

Fig. 5.8. Cross-sectional view of RCA with (a) DIR with short TI, (b) DIR with long TI and (c) DANTE.

5.4.5 DANTE performance at different delay times

We also studied the performance of DANTE sequences in different phases of the heart cycle. Figure 5.9n shows results in the same volunteer but with different delay times. According to a CINE scout scan, the subject was found to have a heart rate of 50 beats/s with a rest period from 470ms-550ms. As stated above, the DANTE preparation pulses have a total duration of 300 ms, which means the DANTE preparation ends 300 ms after the cardiac trigger. The minimal delay time is thus 300ms. In [5], it is stated that DANTE prepulses works well for slow blood flow, as long as the flow velocity > 0.1cm/s. For blood flow in RCA, the flow velocity will meet the criteria during most parts of the cardiac cycle [74]. So theoretically DANTE should work well for all phases, even right after systole. We measured the SNR inside the RCA lumen and LV chamber, as an indicator of residual blood signal. A higher SNR means more blood remains. In Fig. 5.9 (a) and (b), the RCA wall region maintains good contrast. SNR inside the lumen is slightly higher in (a) than (b). Fig.5.9 (b) is shown to give the best result of the four, since the coronary artery is relatively stationary and the blood flow velocity is higher, which ensures better blood suppression. In (c) and (d), the vessel wall is blurred because of in-plane motion, but rhe blood signal is sufficiently suppressed, as indicated by the SNR value.

For blood suppression inside the left ventricle, the flow pattern is more complicated. As stated before, in our studies DANTE only works well for flow in the through-plane direction. After systole, the chamber is emptied by ejection, and we observed the best blood nulling results of the four. During the following phases of heart cycle, as the blood is slowly refilling the left ventricle chamber, slow blood flow and blood inside the imaged slice made the blood suppression more difficult, as shown by the chamber SNR values in (b), (c) and (d). In Fig.5.9 (d), at the end of heart cycle, blood flow is so slow that DANTE did almost nothing to the blood pool inside the left ventricle.

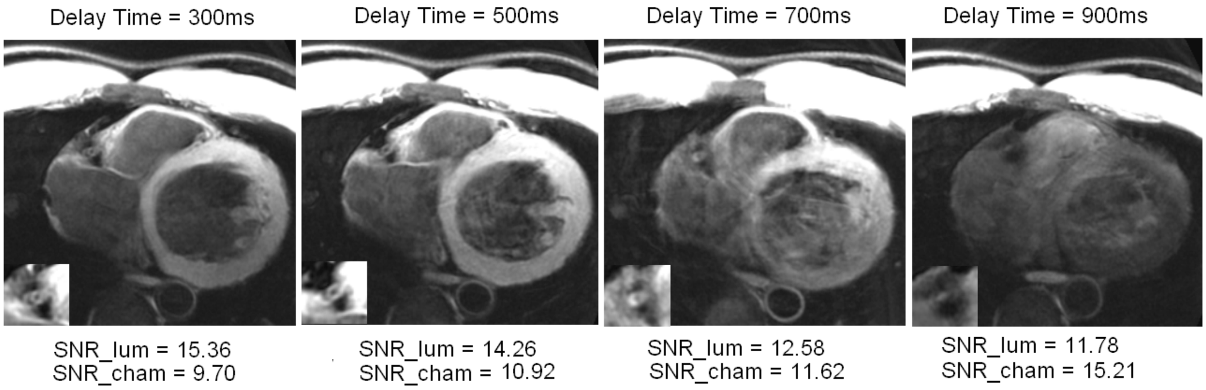

Fig. 5.9. RCA images acquired at different phases of the heart cycle by a DANTE sequence.

5.4.6 SNR and CNR analysis

An SNR and CNR comparison of DANTE and DIR is presented in Table 1. For RCA imaging, DANTE reaches a higher CNR and SNR in the coronary region. One possible reason is that DANTE reduces motion artifacts by always imaging in the rest period, while DIR images will suffer from signal loss caused by blurring. There is not much difference SNR and CNR value between DANTE and DIR RCA images, which corresponds to the observation in [71] that DANTE generates comparable SNR to DIR. The LAD results are opposite from the RCA results. The SNR and CNR of the LAD wall is lower with DANTE than with DIR. But, for the left ventricle, DANTE generated images with higher SNR and CNR. The difference between RCA and LAD results may rise from the motion patterns of the two vessels. During the heart cycle, the principal movement of the LAD is in through-plane direction, parallel to the vessel [12], while the motion of RCA is mostly in-plane. As stated before, DANTE will cause more signal loss for through-plane motion, since the spoiling gradient is along that direction. So, the LAD wall will experience additional SNR drop off based on our imaging localization. The effect of DANTE prepulses on the movement of RCA wall would be less.

	SNR_myo	CNR_LV	SNR_wall	CNR_RCA
RCA DIR	51.67/17.88	32.35/12.4	13.86/7.94	2.86/1.60

RCA DANTE	50.01/18.51	31.73/12.33	21.42/13.65	4.40/2.98
LAD DIR	42.74/19.19	28.95/14.20	22.20/8.04	6.37/4.16
LAD DANTE	44.83/18.53	30.22/13.62	18.28/7.27	6.22/2.78

Table 5.1. SNR and CNR of RCA and LAD imaging. Values are mean/SD.

5.5 Discussion

DANTE preparation is a newly published technique for black blood imaging. Unlike in carotid studies [5], DANTE coronary imaging has to be combined with gating, thus the choice of TR is constrained and the recovery time for tissue signal will be insufficient, which affects the contrast between static and moving spins. However, our simulations show that there still should be sufficient contrast for imaging in each heart cycle. Results also show that DANTE can successfully remove the blood signal inside both the coronary arteries and heart chambers and generate comparable or higher CNR than the DIR method, while preserving most of the signal in the myocardium and vessel wall.

One major advantage of DANTE over DIR is that the preparation needs less time (around 300ms in our study). The sequence is then freer to choose the delay time of the imaging module. The optimal delay time to fit for imaging in rest period is always feasible. The best contrast between wall and lumen could always be achieved with DANTE imaging, as long as we carefully choose the imaging strategy. Unlike with the DIR method, DANTE prepared coronary imaging will also work well if imaging in early-diastole. As stated in [13], both the LAD and RCA have a relatively static period before early ventricular filling, when the coronary artery movement is lmiited. And, since the filling of the ventricle is not complete then, DANTE will also better suppress blood in the left ventricle. As a result, placing DANTE and acquisition in early diastole is more desirable for both coronary and LV black blood imaging.

Another advantage of DANTE is that it is more suitable for multi-slice imaging than DIR. Since the T_1 of blood is relatively long at 3T, the recovery of the longitudinal magnetization of blow will be slow after DANTE prepulses. Good contrast is then feasible for a multi-slice acquisition. The original DIR was designed for single-slice imaging; the second inversion pulse in a DIR module is slice selective. A number of multi-slice DIR black blood techniques have been proposed for more efficient scanning [68,75,76], but they increase the complexity of imaging and are not as simple and robust as DANTE.

Although DANTE is more flexible regarding imaging time, the imaging orientation must be carefully chosen when imaging the heart. The spoiling gradient of the DANTE prepulse nulls the moving spins, but it can also degrade image quality in two way. First, the gradient will cause signal loss if the tissue has motion along the same direction. In our study, both the RCA and LAD had some SNR drop off during imaging. The influence is more significant for LAD imaging. So DANTE is more suitable for RCA studies according our current study. Second, the suppression of blood is also flow-dependent. If there is a large amount of in-plane flow, residual signal can cause artifacts in the heart chamber, although typically not in the coronary region. This effect could be neglected in our coronary studies, but should be carefully treated if DANTE is implemented in studies for other regions, such as short axis and long axis imaging of the heart. The relationship between flow direction and DANTE performance should be further studied if DANTE is used for a wider range of cardiac studies.

5.6 Conclusion

We have tested the performance of DANTE combined with gating for RCA and LAD coronary wall imaging. Based on the parameters chosen by numerical simulation and experimentally validated, DANTE was shown to be able to remove the blood signal in coronary artery and heart chambers. Moreover, DANTE images achieved better contrast between wall and blood pool, especially in RCA studies. We have also studied the influence of motion on DANTE prepared images. More studies are needed in the future to further explore the utility of DANTE for cardiovascular imaging.

Chapter 6

Breath-held 3D Coronary Artery Wall Imaging with DANTE Preparation and Parallel Imaging

6.1 Introduction

MR imaging provides a safe, noninvasive method of imaging atherosclerotic plaque and stenoses in the coronary arteries, providing a potential alternative to x-ray and CT angiography that does not use ionizing radiation. A common clinical protocol for imaging the coronary artery wall is an ECG-triggered single-slice fast spin echo (FSE) pulse sequence with double-inversion recovery (DIR) blood suppression at 1.5T [32]. This method can acquire images with up to 0.46 mm in-plane resolution. This resolution is sufficient to visualize the coronary vessel wall, although it is still inferior to x-ray resolution. Spiral k-space trajectories have been used to achieve high resolution more efficiently without image quality degradation [31]. The scan time for 2D acquisition is usually short enough to be completing during a breath-hold using these methods. Breath-holding minimizes artifacts caused by respiration. Navigator gating enables free-breathing acquisitions. Navigator-gated exams can take 4-8 minutes for a single slice [32].

3D imaging has been explored for more coverage of the coronary arteries. The original 2D imaging method has two problems when applied to 3D scanning. First, the scan time is usually too long for one breath-hold. Navigator gating has to be implemented for a 3D scan to remove respiratory artifact [32,77]. In navigator-gated studies, the sequence will accept the data when diaphragm position is inside a certain range. Otherwise, the data is discarded. The technique can significantly prolong scan time when changes in respiration cause low navigator efficiency [78]. Also, image blur caused by motion may result in overestimation of coronary wall thickness as compared to intravascular ultrasound [79].

Another difficulty comes from traditional DIR blood suppression, which is widely used before the imaging module for black blood imaging. DIR usually contains two 180-degree RF pulses. The first, non-selective pulse inverts all the spins within the transmit coil to $-M_z$, and the second, selective pulse re-inverts the signal in imaging slice back. The reinverted blood inside the imaging slice is replaced by inverted spins during the delay time. However, when the imaging slab is large, one difficulty is that all of the spins may not be replaced during the delay time with slow coronary flow. This can lead to incomplete blood suppression and overestimation of coronary wall thickness. Another difficulty is that the second inversion pulse in DIR may re-invert a large amount of blood signal in the left ventricle back to $+M_z$, which cannot be nulled by relaxation during delay time. Some of this blood can later flow into the coronary artery and decrease the contrast between blood and tissue. Local inversion pulse [77] and oblique inversion pulse [80] techniques modify the second inversion pulse in DIR and can avoid the re-inverting effect in the left ventricle. Blood nulling is then more sufficient for thick slab. These methods require accurate localization of the pulses, and their performance is sensitive to B1 inhomogeneity, especially for 3T scans [81].

Here we propose a new imaging strategy to generate high-resolution, artifact-free images with good contrast. In this study, we used a segmented spiral GRE sequence which has been shown to be capable of generating high resolution images in 3T coronary wall studies [82]. Parallel imaging with multiple coil arrays has been implemented in Cartesian whole heart studies [83]. Here we combined spiral scanning and parallel imaging to accelerate the acquisition process. The resulting scan was nearly three times faster, allowing the study to be finished in one breath hold. Thus we can generate images with resolution as high as in 2D single-slice studies [1], but with more coverage in the z direction within the same scan time. The scan time was reduced to around 20 seconds, as compared to 6-10 minutes in navigator-gated studies [32, 82]. Moreover, by avoiding navigator gating, we hypothesized that the images would have less motion blur and thus the coronary artery walls would be sharper.

To facilitate the use of parallel imaging, dual-density spiral gradients were applied to acquire a fully-sampled region in the center of k-space, with an undersampled outer region of k-space. SPIRiT reconstruction was used for off-line reconstruction to calculate the missing data [8]. Spiral acquisition at 3T is rarely used in coronary artery wall research, since the off-resonance blur will be more severe than at 1.5T. In our study, we added off-resonance correction to the parallel image reconstruction to solve the problem. We also implemented on-line spiral PILS image reconstruction to provide feedback during the exam [64]. For blood suppression, we implemented DANTE prepulses to null the blood in the 3D slab. DANTE was first used for carotid studies, and it has been shown to generate high contrast images without losing too much SNR as compared to DIR [5]. In our study, we combined it with gating and tested its performance in 3D spiral coronary artery wall imaging. It is able to suppress blood inside the coronary arteries and it is insensitive to flow velocity and slice thickness, which makes it suitable for thick slab imaging. A DANTE prepulse does not require the long recovery time that DIR does, so it is more flexible and time efficient. We will show that with the help of DANTE preparation and parallel imaging, we were able to acquire high-resolution, motion-artifact-free coronary wall images with little SNR loss in a single breath-hold. The results will be compared with 2D single-slice, DIR-prepared images and navigator-gated Cartesian GRE images.

6.2 Methods

6.2.1 Sequence design

Figure 6.1 shows the 3D segmented spiral GRE sequence. After detection of the R wave and a delay time, DANTE preparation pulses and a fat suppression pre-pulse are placed right before the imaging module to null both blood and fat signal. The imaging module consists of a series of low-flip-angle excitation pulses, followed by dual-density spiral gradients. Spoiler gradients are applied following the readout. The readout gradients encode the 3D data in a stack-of-spiral k-space trajectory. In every heartbeat, we collect one dual-density spiral interleaf in the x-y plane, and use Cartesian phase encoding in z direction with centric ordering. The stack of spirals in k-space is shown in Fig. 6.2 (a).

6.2.2 Dual-density spiral and parallel image reconstruction

To shorten the acquisition time, we used parallel imaging with 32-channel coils in our studies. Only 1/4 of the total interleaves are collected during the scan using dual-density spiral trajectories. The center of k-space is fully sampled, leaving the rest of k-space sub-sampled by a factor of 4, as illustrated in Fig.6.2 (b). Missing data is calculated slice-by-slice using SPIRiT in the reconstruction step [8]. In the SPIRiT algorithm, the fully sampled region in k-space is used for calibrating the convolution kernel. That kernel is then combined with data consistency conditions for iteratively calculating the unaliased final image.

SPIRiT takes about 40 iterations to reconstruct one slice. The algorithm is relatively complicated for on-line image reconstruction. Hence, we also tried spiral PILS to remove undersampling artifacts in a simpler way [64]. As stated in Chapter 4, we generate one Fermi window for each coil image to window out the artifacts outside the window. This improves the image quality in the final coil-combined image relative to a direct (non-parallel) image reconstruction, although the performance of PILS may be not as robust as SPIRiT. We implemented spiral PILS for on-line reconstruction, resulting in a rapid 3D spiral parallel on-line image reconstruction. We also saved the raw data for later off-line reconstruction using SPIRiT.

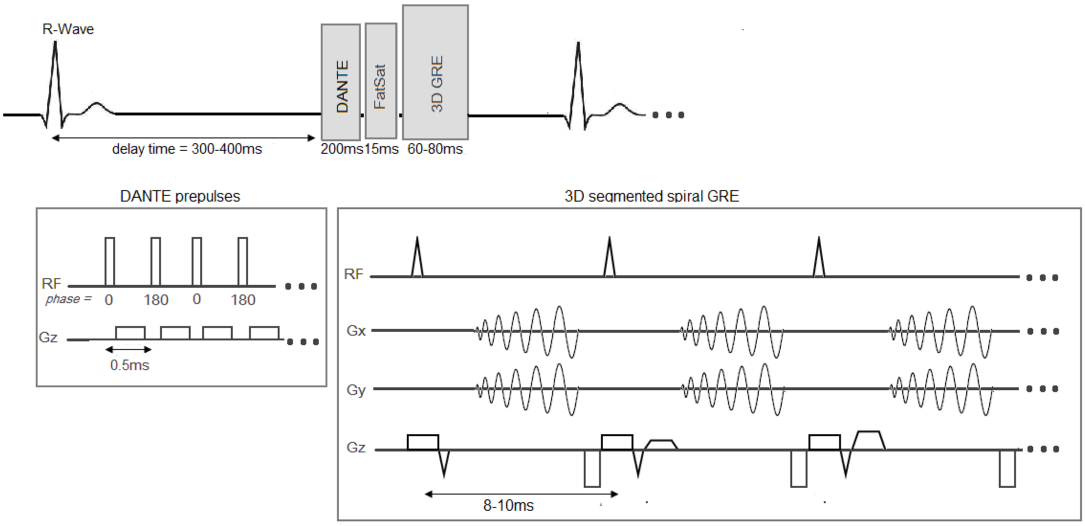

Fig. 6.1. Schematic of 3D segmented spiral GRE sequence with DANTE preparation. The imaging module is placed in mid-diastole, after determining the start of rest period. The DANTE preparation consists of 400-500 non-selective phase alternating pulses, each with 7-10 degree flip angle, with 0.5 ms spacing between pulses.

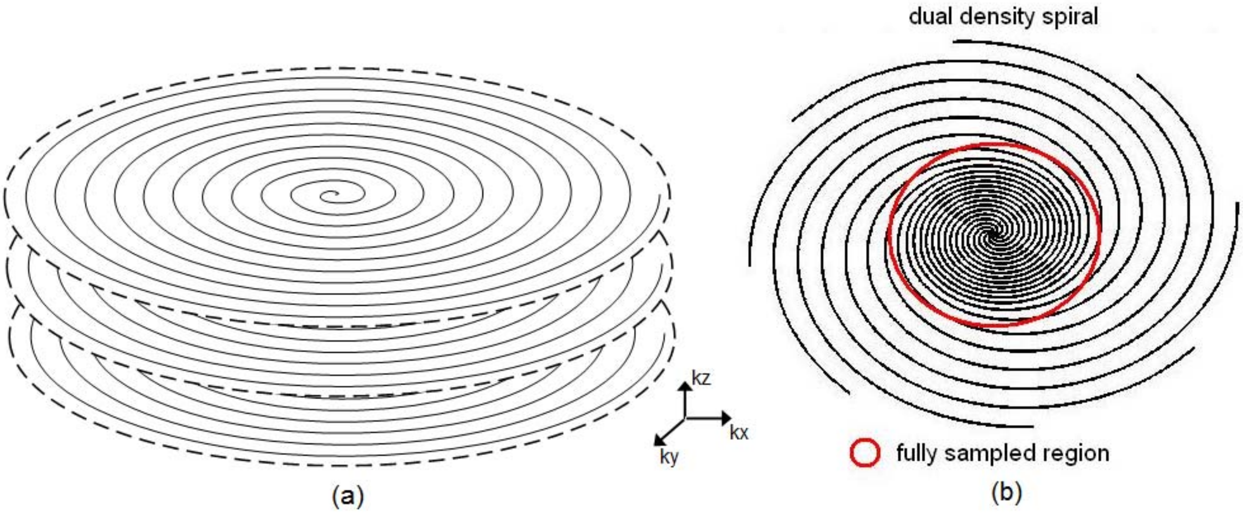

Fig. 6.2. Illustration of (a) stack of spirals and (b) dual-density spiral k-space trajectories.

6.2.3 Chebyshev off-resonance correction

B0 off-resonance effects can be crucial in coronary wall studies, since the wall thickness is less than 1 mm [1]. It is especially important when we are using long spiral readout gradients for acquisition at 3T. Our first attempt for correction was to acquire an additional field map before the actual data acquisition. However, we found that a direct correction using the low-resolution field map did not help much in the final reconstruction. Conjugate phase deblurring [84] is a technique usually used for off-resonance correction based on the acquired low resolution field map. However, it is quite time consuming. Chen et al. [73] proposed a fast version of inhomogeneity correction using a semi-automatic correction methods that generates a high-resolution field map. It uses Chebyshev polynomials to approximate the off-resonance phase terms. Off resonance caused by B0 inhomogeneity and concomitant gradients can be corrected simultaneously by this method.

In this study, all the datasets are sub-sampled by a factor of 4. The aliasing caused by undersampling will corrupt the original Chebyshev reconstruction algorithm if used directly. We modified the reconstruction scheme as follows. First, unaliased images are reconstructed by SPIRiT. Then, we substitute the base images used in Chebyshev reconstruction with these reconstructed fully sampled images [73]. After that the typical Chebyshev approximation reconstruction was performed to search for a high-resolution field map. The map is later used for correcting off-resonance blurring.

Figure 6.3 shows reconstruction results of a phantom dataset acquired at 3T with a 12-channel head coil and a 2D single-slice GRE sequence. The readout was 16 ms long with a constant-density spiral trajectory. Figure 6.3 (a) shows and image reconstructed by direct gridding and sum of squares. The image has significant undersampling artifacts. SPIRiT is capable of unaliasing the image, as shown in Fig. 6.3 (b). The result is free of artifacts and has improved image quality. However, the lines in the center are somewhat widened due to off-resonance effects. Combining Chebyshev correction with SPIRiT removes the blur, as shown in Fig. 6.3 (c).

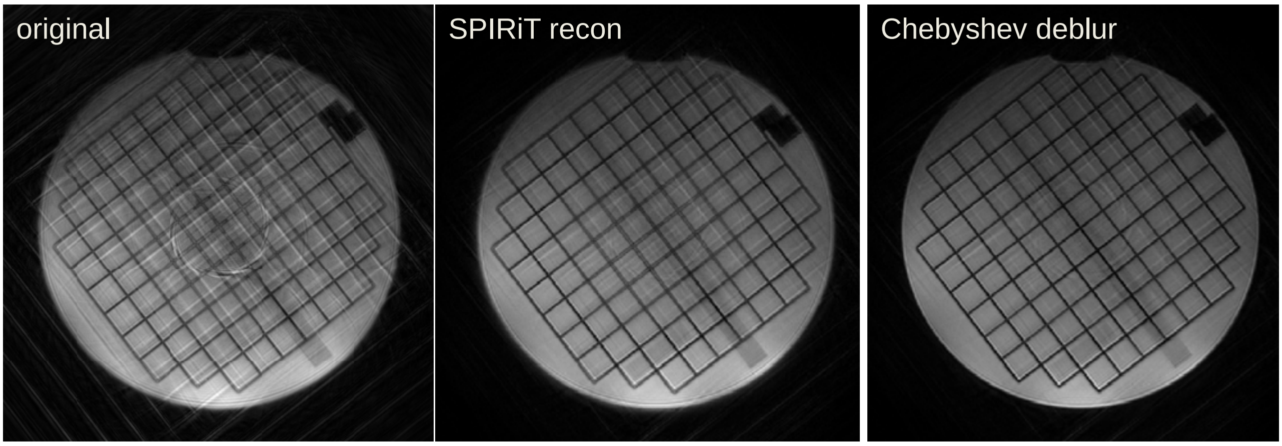

Fig. 6.3. Phantom images acquired using a 12-channel coil and 16ms spiral readout, reconstructed by (a) direct reconstruction, (b) SPIRiT reconstruction, and (c) SPIRiT reconstruction combined with Chebyshev deblurring.

6.3 Experimental Design

Experimental imaging studies were conducted on the mid RCA to test the performance of the 3D spiral GRE sequence. A DIR-prepared 2D single-slice spiral segmented GRE sequence was used for coronary artery localization and cross-sectional imaging. The 2D cross-sectional images were used for image quality comparison with the 3D results. The sequence consisted of a 5-ms spectral-spatial excitation pulse, followed by a 16-ms constant-density spiral readout gradient. FOV = 280 - 300mm, 14 interleaves, 5-mm slice thickness, in-plane resolution 0.8-0.9 mm. We used a TrueFISP cine sequence to determine the rest period of coronary artery movement. All of the acquisitions were set in the rest period to minimize motion artifacts. Typical localization of imaging slabs for the RCA and LAD are shown in Fig. 6.4.

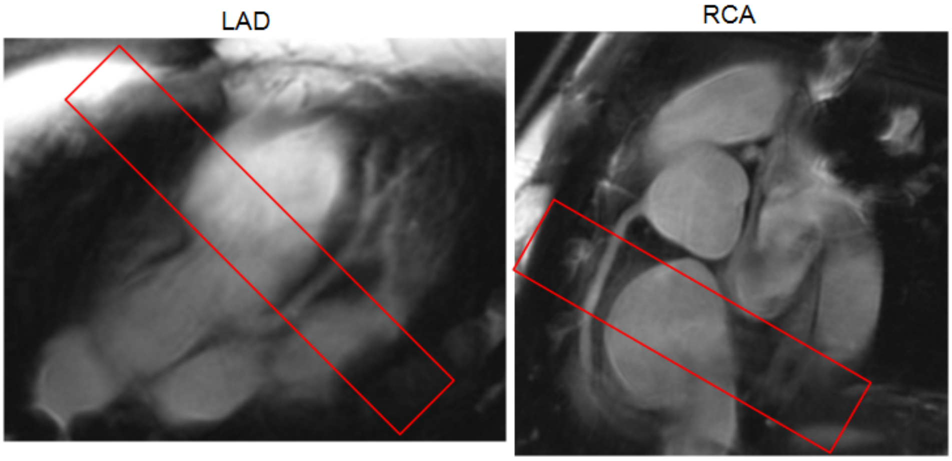

Fig. 6.4. Localization of imaging slabs for LAD and RCA.

Seven volunteers (ages 25-32, all male) were imaged with a 3T Siemens Avanto scanner, with a 32-channel coil array and ECG geting. For each volunteer, four sequences were used: 1) DIR-prepared 2D single-slice spiral GRE sequence; 2) DANTE-prepared 3D spiral GRE sequence; .3) DIR-prepared 3D spiral GRE sequence; and 4) navigator-gated Cartesian GRE sequence. SNR and CNR in the left ventricle and coronary artery wall regions were evaluated and analyzed. The standard deviation of the noise was measured in a region near the chest wall.

The 3D spiral GRE sequence collected 18 of 72 spiral interleaves in k-space. The excitation pulse was 30 degrees and 4 ms long. The dual-density spiral readout gradient was 6-8 ms, resulting in an in-plane resolution of 0.5mm to 0.9mm. We usually collected 6×5mm slices. Zero-filling in the z direction was used to reduce reconstructed pixel size. Both DIR and DANTE preparations were used for blood suppression and the resultant contrast were compared later. All the volunteers are required to hold their breath for ~20s. The results were reconstructed offline using a 6-node cluster; each node had two 2.8GHz Intel Xeon CPUs and 2GB memory.

A navigator-gated Cartesian GRE sequence with DIR was executed to acquire free breathing coronary artery wall images. The protocol was as follows: FOV = 280 –

300mm, image matrix = 304×320, inplane resolution = 0.9×1mm, flip angle = 12 degrees, TR/TE = 200/3.04ms. Orthogonal navigator pulses were placed at the diaphragm and acquired before the readout, with gating window = 5mm and correction factor = 0.6.

6.4 Results

6.4.1 DANTE performance

Coronary wall images with DANTE and DIR preparation are shown in Fig 6.5. The comparison was conducted in both RCA and LAD regions. In both cases, DIR images suffered from unsuppressed blood in the heart chambers, as predicted in [77]. The contrast was too poor to visualize the coronary wall. Although in some cases DIR performed somewhat better than in Fig. 6.5, the performance of DIR in 3D imaging was highly variable, largely depending on the structure of the heart and timing of flow. Theoretically, DANTE-prepared images can remove the blood in all regions of the heart, since non-selective pulses are used. In RCA images, there was excellent contrast between blood and tissue. The coronary wall looked sharp and clear. For LAD results, we observed some artifacts caused by unsuppressed blood flow in the left ventricle. To achieve the best blood nulling for coronary wall imaging, the DANTE flow-spoiling gradients are placed along the direction of coronary artery flow. However, in LAD imaging, the blood flow in the left ventricle is complicated and it is not always along the spoiling gradient direction, so there can be residual blood signal in the ventricle. In the LAD wall region, DANTE typically achieved good contrast, but the SNR was sometimes degraded from artifacts resulting from residual blood signal.

The SNR and CNR analysis in RCA images showed that DANTE-prepared images generated comparable SNR in the myocardium and approximately double the CNR in left ventricle regions ($p < 0.05$) than DIR-prepared images. The SNR and CNR in the coronary wall were not calculated, since the contrast for DIR images was too poor to show the lumen.

We also conducted in vivo experiments to test the performance of DANTE when the number of pulses changes. Figure 6.6 (a) shows the RCA results with DANTE preparation, with the number of pulses varying from 200, 300, 400, 500, and 600, with the flip angle set to 7 degrees and the spacing between pulses set to 0.5ms. The coronary region is zoomed for better visualization. The blood suppression performed better when more pulses were used in the DANTE preparation. The tradeoff was be the loss of tissue signal. For $N_p = 500 \textit{ and } 600$, the image achieved the best contrast in the left ventricle and the coronary wall while maintaining good SNR. As a result, we chose this parameter set in all of the following studies.

Figures 6.6 (b) and (c) demonstrate the experimental and simulated signal dropoff for moving and static spins. In (b) we observed good agreement between in-vivo and simulation results. However, in (c), the actual signal loss is more severe then predicted. A likely reason for this is that the coronary artery experiences up to 10cm/s through-plane movement when imaging [13], which will result in SNR loss. The movement of the coronary artery can be minimized by carefully choosing the starting time of imaging in heart cycle so that the degree of SNR loss could be decreased to some extent. The cine scout scan is crucial in setting up a proper starting time.

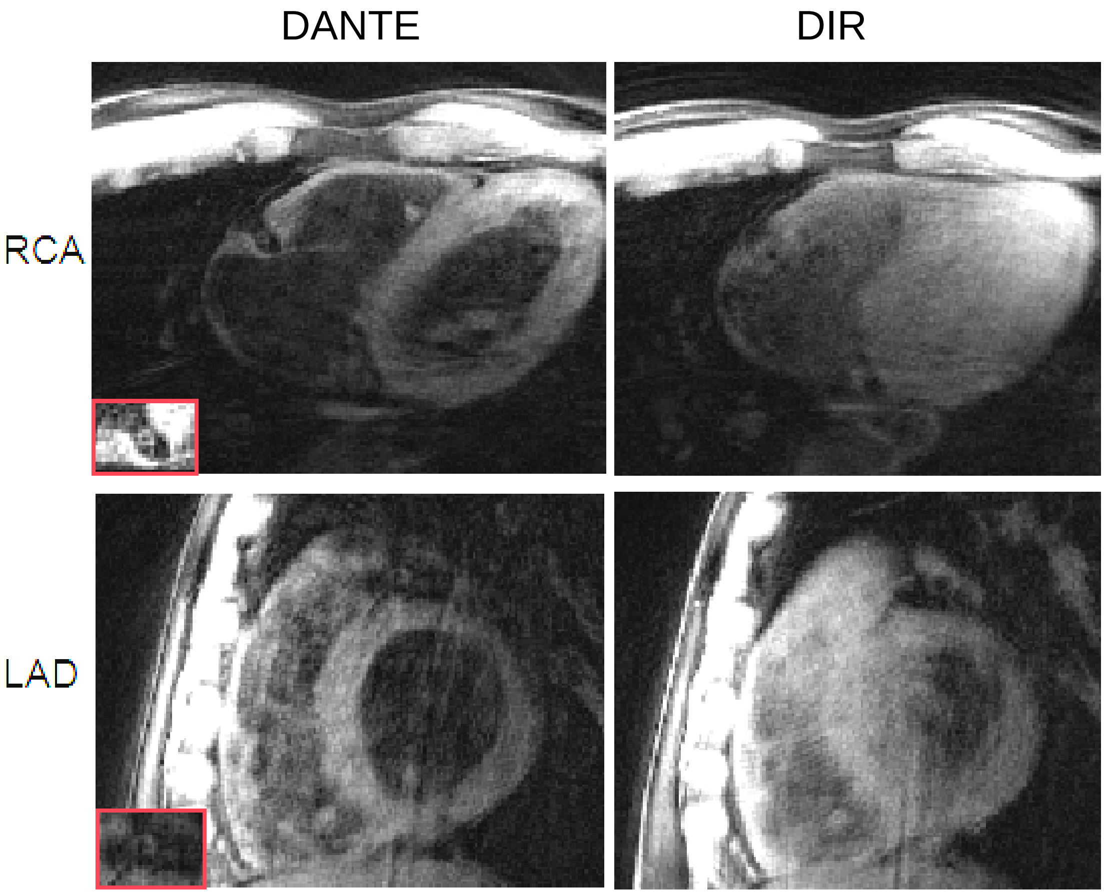

Fig. 6.5. RCA and LAD coronary wall images with DANTE and DIR preparation.

	SNR_myo	CNR_LV(p<0.05)
RCA DIR	49.9/29.9	15.9/6.2
RCA DANTE	47.7/16.5	32.7/14.4

Table 6.1. SNR and CNR analysis of RCA and LAD results. Values are mean/SD.

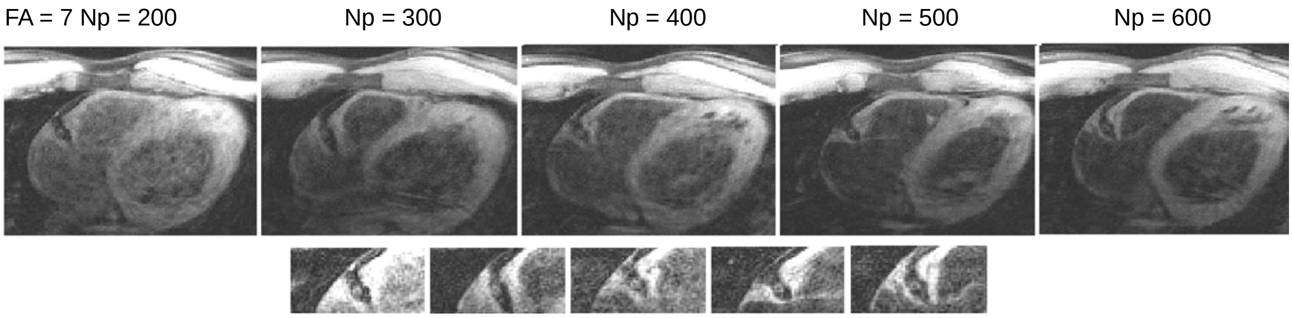

(a)

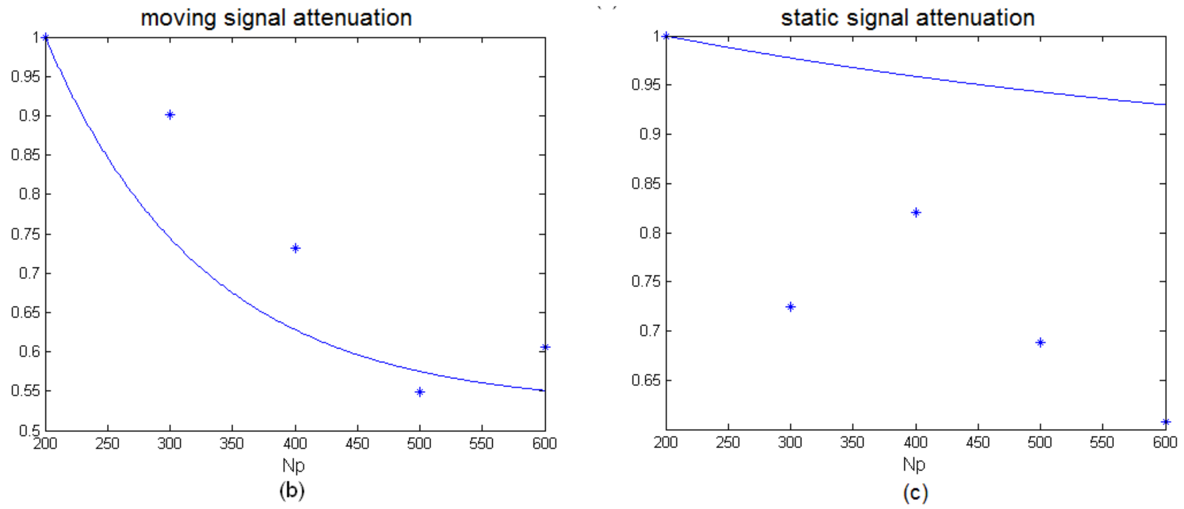

Fig. 6.6. (a) RCA wall images acquired with DANTE preparation, with NP = 200, 300, 400, 500 and 600 and flip angle = 7 degrees. (b) Simulated and experimental signal attenuation of moving spins using DANTE preparation. (c) Simulated and experimental signal attenuation of static spins using DANTE preparation.

6.5.2 Parallel imaging

In order to increase acquisition efficiency, we used parallel imaging in our study. With an acceleration factor of 4, the resultant image will have significant undersampling artifacts with a direct, non-parallel image reconstruction. The missing spiral interleaves are calculated by iteration based on data consistency and convolution kernels trained in center of k-space by SPIRiT. We hypothesized that the SNR loss caused by parallel imaging would be minor, and our coronary images will have comparable SNR in the myocardium and coronary wall to 2D single-slice fully sampled results.

Figure 6.7 shows an RCA image with an in-plane resolution of 0.5mm. In order to acquire the image, a 16ms spiral readout was used. We would expect severe off-resonance blurring at 3T with this long readout. Figure 6.7 (a) shows the direct reconstructed image. Significant undersampling artifacts arising from the chest wall and back are evident in the middle of the image. Spiral-like undersampling artifacts can be seen throughout the image. The image also suffers from off-resonance blurring. The SPIRiT reconstruction removes most of the undersampling artifacts, as seen in (b), and significantly enhances the image quality. It should be noticed that the noise level is also elevated in some regions of the background using SPIRiT.

A direct implementation of off resonance correction to the undersampled image will corrupt the correction, since the high-resolution field map cannot be precisely generated. Based on the SPIRiT reconstructed, fully sampled images, we applied a semi-automatic off-resonance correction using Chebyshev approximation of inhomogeneity terms. A more detailed comparison between no correction and deblurred images is shown in Fig. 6.8. We see that in the anterior chest wall, where the inhomogeneity is more serious due to water/air interface (as indicated by red arrow), the correction method reduces off-resonance blurring. The corresponding regions in the corrected images look clearer. The same effect could be found near the coronary wall, as can be seen in the areas indicated by red arrows in slices 2, 3 and 4 at the bottom of Fig. 6.8.

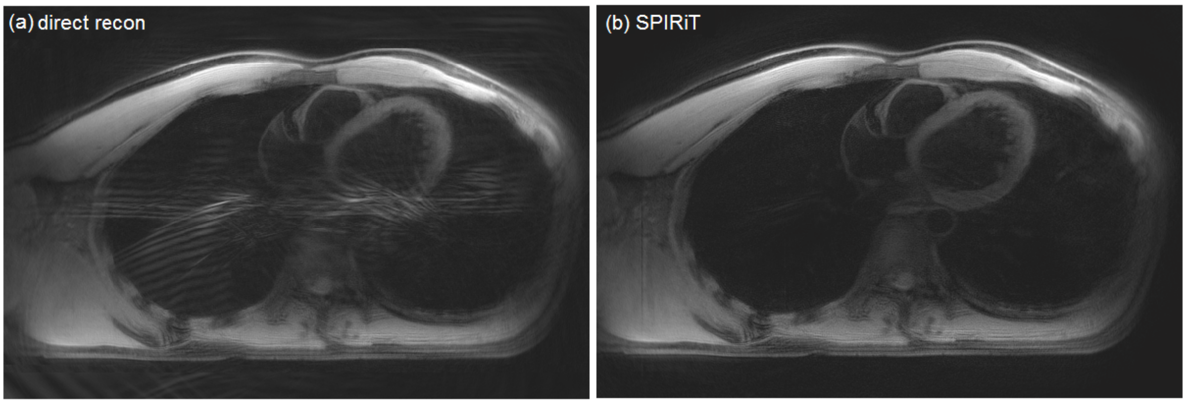

Fig. 6.7. RCA image reconstructed with (a) direct reconstruction and (b) SPIRiT.

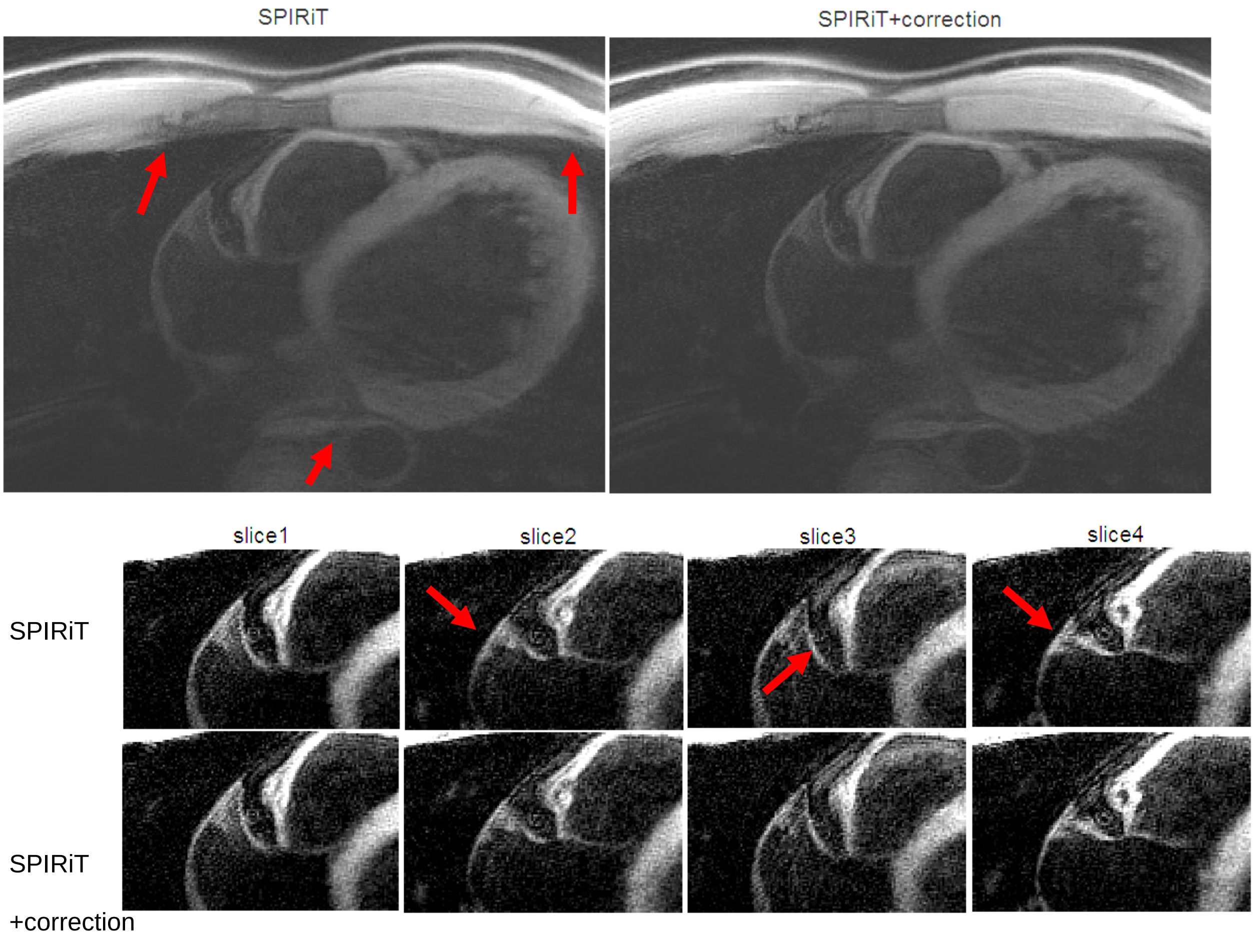

Fig. 6.8. Comparison between SPIRiT only and SPIRiT with off-resonance correction for zoomed heart (top) and RCA wall (bottom) regions.

We also implemented spiral PILS in our on-line reconstruction to increase efficiency. The results are showed in Fig. 6.9. As in Fig. 6.7, the original image has significant artifacts. By applying a mask to each aliased coil image, the artifacts were suppressed and the resulting image has an increased quality, as shown in (b). The total reconstruction takes about 10 seconds on the image reconstruction computer of the Siemens scanner, which is much faster than the SPIRiT reconstruction. However, the performance of PILS depends on the size of the mask. A smaller mask will help to remove the aliasing, but it will also suppress desired signal. When a larger mask is applied, some artifacts remain, as seen in the area of the left ventricle in Fig. 6.9 (b). Also, the window size is patient-dependent, which further decreases the robustness of

PILS reconstruction.

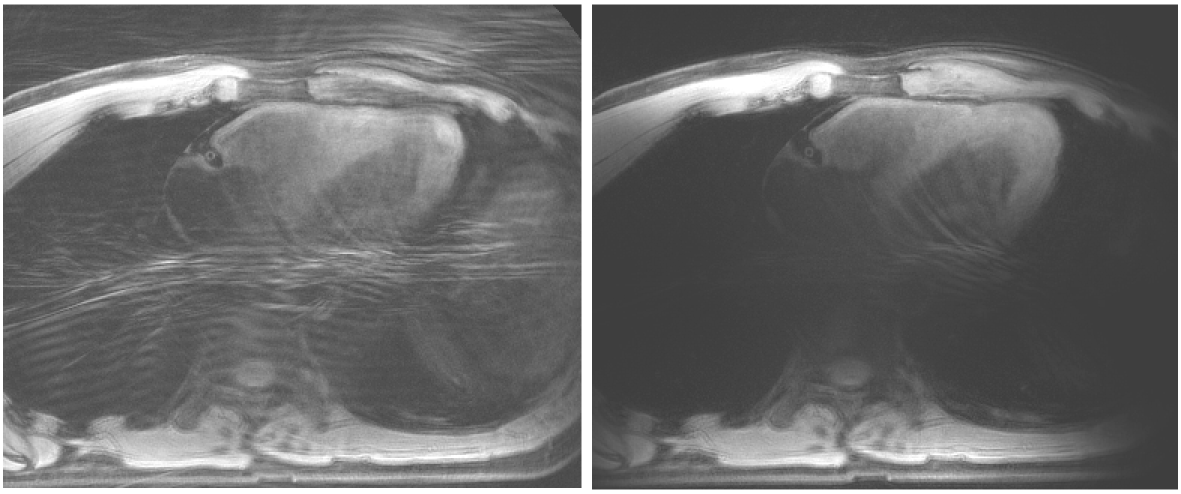

(a) (b)

Fig.6.9. RCA results with (a) direct reconstruction (b) on-line PILS reconstruction.

Two comparisons between 2D single-slice, DIR prepared and 3D DANTE prepared results are shown in Fig. 6.10. The imaging protocol was specified so that the two images have the same resolution and signal intensity level. The in-plane resolution was 0.9 mm. The flip angle of the 2D sequence was set to 30 degrees to match the 3D sequence. In the 2D single-slice images, the coronary wall appears dark, while the chest wall and left ventricle have higher signal levels. In the 3D images, the signal intensity is more uniform and the coronary wall is easier to see, as shown in the zoomed region. The SNR and CNR analysis in Table 2 shows similar results. The mean SNR of myocardium in the 2D images are higher than 3D. The contrast in the LV is similar for the two. In the coronary regions, there is less contrast for the 2D images, since the SNR in coronary wall is significant lower than 3D. One possible explanation for this is that through-plane motion may have led to misregistration between the slice-selective re-inversion in the DIR module and the imaging slice excitation in data acquisition. The selection of a thick slab in 3D could decrease the influence of through-plane motion, and thus the image tends to have higher signal in the wall area. This comparison study supports our hypothesis that parallel imaging causes no significant signal loss in our studies, and so it is an effective method to reduce the scan time in our 3D spiral coronary wall imaging studies.

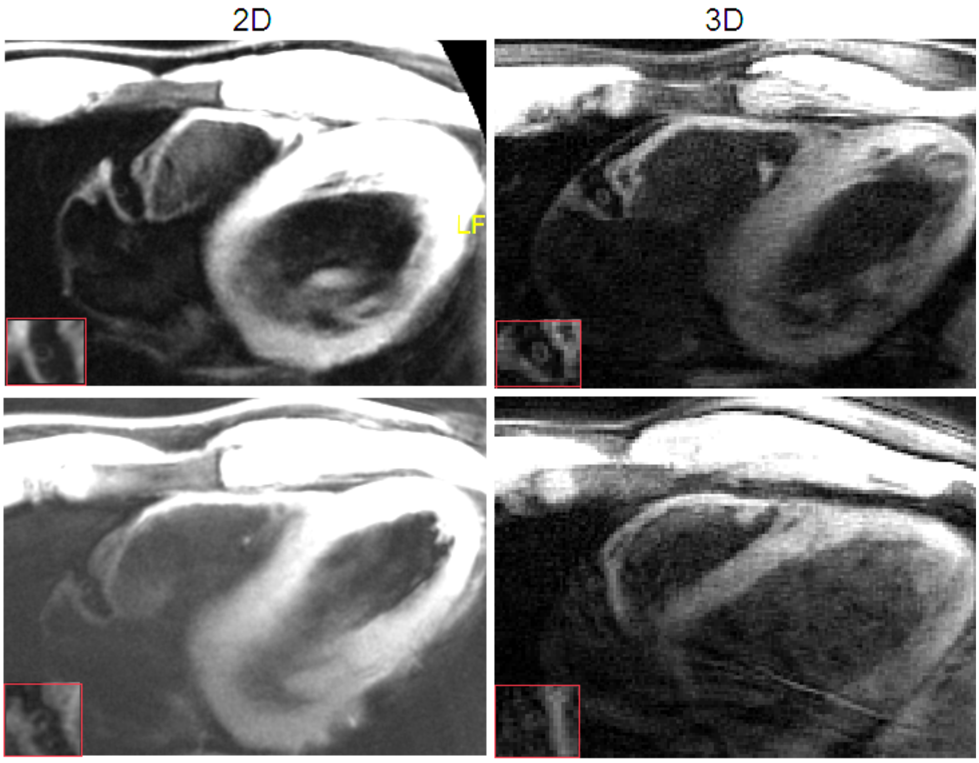

Fig. 6.10. Two sets of RCA wall images acquired by 2D single-slice GRE sequence and 3D stack of spirals sequence.

	SNR_myo	CNR_LV	SNR_wall	CNR_RCA
2D DIR	52.1/7.8	32.9/14.0	15.7/5.3	3.8/1.5
3D DANTE	47.7/16.6	32.7/14.4	24.0/6.7	4.1/1.6

Table 6.2. SNR and CNR of RCA and LAD images. Values are mean/SD.

6.5.3 Breath-hold performance

With the aid of parallel imaging and spiral acquisition, we were able to shorten our scan time to around 20s. The whole 3D dataset could then be collected within one breath-holding interval. The scan time efficiency is thus much higher than with navigator-gated techniques. The image quality of results from the two methods was also studied. Results from this comparison are shown in Fig. 6.11, including the center slice of a breath-held, 3D spiral dataset and a single-slice 2D navigator-gated image. The in-plane resolution and slice thickness were chosen to be similar in the two datasets. The navigator efficiency was about 38% and the total scan time for the navigator image was about 5 minutes. The navigator-gated image has some motion artifacts, including some blurring of the RCA. This reduces the contrast, making it difficult to see the coronary artery wall. The noise level of breath-held image is higher, probably because of reduced scan time, noise amplification from the parallel image reconstruction, and residual undersampling artifacts.

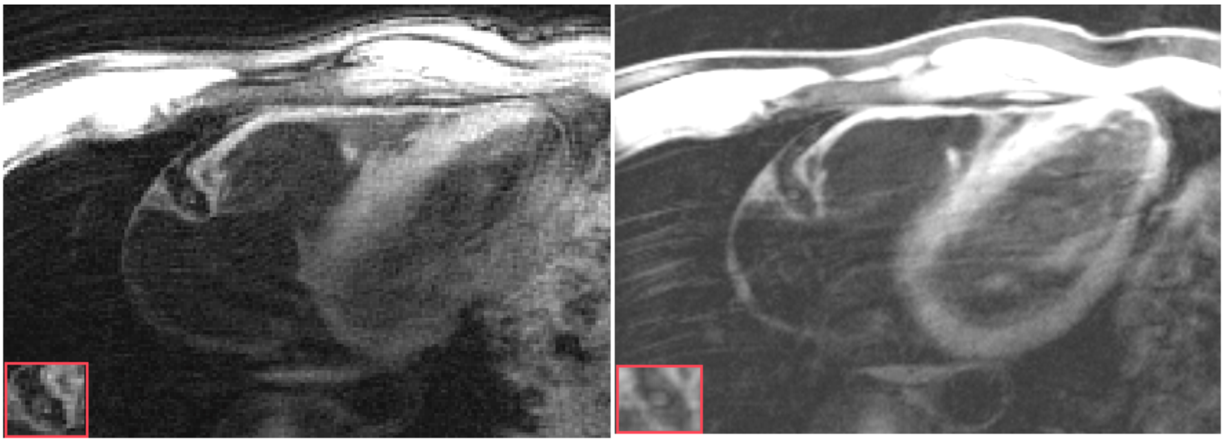

Fig. 6.11. Breath-held spiral 3D (left) and navigator-gated Cartesian 2D (right) RCA wall images.

6.6 Discussion

We have shown that a DANTE prepared, 3D gradient-echo sequence can generate motion-artifact-free coronary wall images with good contrast and resolution. With the help of parallel imaging and spiral acquisition, we could reach up to 0.5mm in-plane resolution as in 2D single-slice imaging, but covering a slab that is eight times thicker during the same amount of time [1]. Other 3D coronary artery wall studies have used navigator gating to eliminate motion artifacts. In [77], it took 6-9 minutes to complete a scan with a 50% efficiency of navigator gating with a resolution equal to 0.66 mm. In [82], the total scan took 600 cardiac cycles to reach 0.7 mm in-plane resolution, even assuming 100% efficiency. Our strategy can generate higher resolution and the same thickness of coverage in z direction, but with much less scan time compared to navigator-gated studies. Hence the efficiency was greatly increased.

Another novelty of our study is that the 3D vessel wall study was conducted at 3T with spiral acquisition. Earlier 2D single-slice and 3D coronary artery wall studies were conducted at 1.5T [32, 1, 85]. Initial 2D studies at 3T were published in [86], showing the feasibility of performing coronary artery wall imaging at higher magnetic field. Theoretically, higher magnetic field will lead to an increased SNR. However, combining spiral acquisition with higher field strength is difficult, since the off-resonance blur will be more severe and the B1-inhomogeneity will also cause signal variation to some extent. In our studies, we used off-resonance correction and low flip angle pulses to reduce the influence of B0 and B1field inhomogeneity, respectively.

Our 3D breath-held coronary wall imaging method could be improved. First, the SNR of the coronary wall could be increased. We used a set of low flip angle pulses for excitation in our segmented GRE sequence; as a result, the potential signal intensity that we achieved was not very high. The low SNR level may affect the detection of atherosclerotic plaque, since the coronary region is already hard to visualize. A spiral turbo spin echo (TSE) sequence is one potential solution to this problem [87]. The 90-degree excitation and longer signal integration time would likely yield higher SNR than the GRE sequence. However, the sequence would be more sensitive to unsuppressed flow and motion.

The choice of parallel imaging reconstruction technique is another issue for the study. Although a number of spiral parallel imaging reconstruction techniques have been proposed recently [40, 62, 63], there is no standard method for the problem. SPIRiT is known for its robustness and ability to handle various trajectories. However, in our results we could see that SPIRiT may increase the noise in certain regions. Lustig et al. stated that using a noise correlation matrix could improve the performance of SPIRiT and result in a better image [8]. SPIRiT reconstruction also suffers from long computation time, especially when combined with Chebyshev off-resonance correction. The 40-iteration reconstruction for a 500 × 500 image typically takes 450 s; with Chebyshev off-resonance correction, it takes 10 minutes, even with array-compression. PILS could overcome the computation time problem, but its performance cannot be ensured for each study. The problem could be addressed by developing an on-line version of SPIRiT implemented in C++ rather than Matlab. Another alternative is a non-iterative reconstruction algorithm with comparable performance to SPIRiT, such as through-time GRAPPA [88].

6.7 Conclusion

With the aid of dual-density spiral acquisition and parallel imaging, we were able to perform 3D stack-of-spiral GRE coronary artery wall imaging within one breath-hold. DANTE preparation was also implemented to achieve a higher contrast than traditional DIR preparation. The results are shown to have comparable SNR and CNR to 2D single-slice studies. The breath-held images also have fewer motion artifacts than images acquired using navigator gating. Future studies will focus on increasing SNR and building more efficient reconstruction tools. Compressed sensing may also be implemented to further accelerate the scan [61].

Chapter 7

Conclusion

In this thesis, we studied the synthetic target algorithm, a novel parallel imaging technique developed to accelerate image reconstruction. We developed and tested this technique for Cartesian, radial and spiral trajectories. Improvements were made to increase the reconstructed image quality. We implemented and tested the performance of DANTE black blood imaging with gating for coronary artery wall imaging. With the help of DANTE and parallel imaging, we were able to acquire high-contrast, high-resolution 3D coronary wall images within one breath-hold to reduce motion artifacts. The contributions of the dissertation are summarized as follows:

1) We validated that the synthetic target algorithm could successfully reduce the computation time with a small reduction in image quality compared to GRAPPA. Phantom and in vivo data were used for validation.
2) We added array compression and parallel computing to the original synthetic target method to increase reconstruction speed. The relationship between compression rate and the resultant error was also studied. The computation time of accelerated synthetic target and GRAPPA were compared.
3) We modified the synthetic target algorithm with synthetic target-PILS to reduce the noise for spiral parallel image reconstruction. Similarly, the phase-constrained synthetic target algorithm was developed for radial trajectories.
4) We tested the performance of DANTE with a 2D spiral GRE sequence for imaging the RCA and LAD. Both simulation and in-vivo results were presented. We demonstrated the possibility of combining DANTE with gating in cardiac imaging for the first time.

5) We demonstrated that breath-held 3D spiral coronary artery wall imaging is feasible with DANTE preparation and parallel imaging. Off-resonance correction was combined with parallel image reconstruction to deblur the image. Results were shown to evaluate the performance of our imaging strategy.

7.1 Future Directions

Future improvement of the synthetic target method could be focused on non-Cartesian trajectories. The criteria for the original algorithm do not fit well for variable-density spiral and radial trajectories. Although we made an effort to reduce artifacts in Chapter 4, the results were not that robust. Iterations and new constraints could be implemented in the training process to calculate a better convolution kernel, such as in SPIRiT. There should be a good balance between iteration number and image quality. More in-vivo data should be tested to further validate the performance of the synthetic target method.

DANTE preparation could be implemented into other cardiovascular studies, such as delayed-enhancement imaging and whole heart imaging. The signal drop-off for static tissues should be studied, especially for cardiac imaging. The current version DANTE is direction-dependent; the current strategy could be modified to interactively place DANTE along a user-defined direction.

Although we have shortened the scan time for 3D coronary artery wall studies to about 20 heartbeats, the time could be further decreased if a more powerful image reconstruction algorithm is implemented. Compressed sensing has been shown to be able to achieve an undersampling factor higher than 4. The acquisition time could then be shortened, which will lead to fewer motion artifacts and make patient studies more practical.

Bibliography

[1] ZA Fayad, V Fuster, JT Fallon, T Jayasundera, SG Worthley, G Helft, JG Aguinaldo, JJ Badimon, and SK Sharma. "Noninvasive in vivo human coronary artery lumen and wall imaging using black-blood magnetic resonance imaging", *Circulation*, vol. 102, no. 5, pp. 506-510, 2000.

[2] KP Pruessmann, M Weiger, MB Scheidegger, and P Boesiger. "SENSE: sensitivity encoding for fast MRI", *Magn Reson Med*, vol. 42, no. 5, pp. 952-962, 1999.

[3] MA Griswold, PM Jakob, RM Heidemann, M Nittka, V Jellus, J Wang, B Kiefer, and A Haase. "Generalized autocalibrating partially parallel acquisitions (GRAPPA)", *Magn Reson Med*, vol. 47, no. 6, pp. 1202-1210, 2002.

[4] W Chen. "Image reconstruction for spiral scanning in magnetic resonance imaging", Ph.D dissertation, Dept. Biomedical Engineering, University of Virginia at Charlottesville, VA, 2008.

[5] L Li, KL Miller, and P Jezzard. "DANTE‐prepared pulse trains: A novel approach to motion‐sensitized and motion‐suppressed quantitative magnetic resonance imaging", *Magn Reson Med*, vol. 68, no. 5, pp. 1423-1438, 2012.

[6] CH Meyer, BS Hu, DG Nishimura, and A Macovski. "Fast spiral coronary artery imaging", *Magn Reson Med*, vol. 28, no. 2, pp. 202-213, 1992.

[7] PC Yang, CH Meyer, M Terashima, S Kaji, MV McConnell, Al Macovski, JM Pauly, DG Nishimura, BS Hu. "Spiral magnetic resonance coronary angiography with rapid real-time localization", J *Am Coll Cardiol*, vol. 41no. 7, pp. 1134-1141, 2003.

[8] M Lustig, and John M. Pauly. "SPIRiT: Iterative self‐consistent parallel imaging reconstruction from arbitrary k‐space", *Magn Reson Med*, vol. 64, no. 2, pp. 457-471,

2010.

[9] M Buehrer, KP Pruessmann, P Boesiger, and S Kozerke. "Array compression for MRI with large coil arrays", *Magn Reson Med*, vol. 57, no. 6, pp. 1131-1139, 2007.

[10] JL Fleckenstein, BT Archer, BA Barker, JT Vaughan, RW Parkey, and RW Peshock. "Fast short-tau inversion-recovery MR imaging", Radiology, vol. 179, no. 2, pp. 499-504, 1991.

[11] J Wang, VL Yarnykh, T Hatsukami, B Chu, N Balu, and C Yuan. "Improved suppression of plaque‐mimicking artifacts in black‐blood carotid atherosclerosis imaging using a multislice motion‐sensitized driven‐equilibrium (MSDE) turbo spin‐echo (TSE) sequence", *Magn Reson Med*, vol. 58, no. 5, pp. 973-981, 2007.

[12] Y Wang, E Vidan, and GW Bergman. "Cardiac Motion of Coronary Arteries: Variability in the Rest Period and Implications for Coronary MR Angiography", *Radiology*, vol. 213, no. 3, pp. 751-758, 1999.

[13] WY Kim, M Stuber, KV Kissinger, NT Andersen, WJ Manning, and RM Botnar. "Impact of bulk cardiac motion on right coronary MR angiography and vessel wall imaging", *J Magn Reson Imaging*, vol. 14, no. 4, pp. 383-390, 2001.

[14] J Bogaert, S Dymarkowski, and A Taylor. "Coronary Artery Disease", *Clinical Cardiac MRI*, pp. 381-437, 2005.

[15] AS Go, D Mozaffarian, V L Roger, EJ Benjamin, JD Berry, WB Borden, DM Bravata et al. "Heart disease and stroke statistics—2013 update: a report from the American Heart Association", *Circulation*, vol. 127, no. 1, pp. 6-245, 2013.

[16] GK Hansson, AK Roberson and C Soderberg-Naucler. "Inflammation and atherosclerosis". *Annu. Rev. Pathol*, vol. 1, pp. 297-329, 2006.

[17] P Libby, PM Ridker and A Maseri. "Inflammation and atherosclerosis", *Circulation*, vol. 105, no. 9, pp. 1135-1143, 2002.

[18] SE Nissen, EM Tuzcu, P Schoenhagen, T Crowe, WJ Sasiela, J Tsai, J Orazem, RD Magorien, C O'Shaughnessy and P Granz. "Statin therapy, LDL cholesterol, C-reactive protein and coronary artery disease ", *N Engl J Med*, vol. 352, no. 1, pp. 29-38, 2005.

[19] SE Nissen, and P Yock. "Intravascular ultrasound novel pathophysiological insights and current clinical applications", *Circulation*, vol. 103, no. 4, pp. 604-616, 2001.

[20] GS Mintz, JJ Popma, AD Pichard, KM Kent, LF Satler, YC Chuang, CJ Ditrano, and MB Leon. "Patterns of calcification in coronary artery disease: a statistical analysis of intravascular ultrasound and coronary angiography in 1155 lesions", Circulation, vol. 91, no. 7, pp. 1959-1965, 1995

[21] DB Simons, RS Schwartz, WD Edwards, PF Sheedy, JF Breen, and JA Rumberger. "Noninvasive definition of anatomic coronary artery disease by ultrafast computed tomographic scanning: a quantitative pathologic comparison study", *J Am Coll Cardiol*, vol. 20, no. 5, pp. 1118-1126, 1992.

[22] L Wexler, B Brundage, J Crouse, R Detrano, V Fuster, J Maddahi, J Rumberger, W Stanford, R White, and K Taubert. "Coronary artery calcification: pathophysiology, epidemiology, imaging methods, and clinical implications: a statement for health professionals from the American Heart Association", *Circulation*, vol. 94, no. 5, pp. 1175-1192, 1996.

[23] RL Morin, TC Gerber, and CH McCollough. "Radiation dose in computed

tomography of the heart", *Circulation*, vol. 107, no. 6, pp. 917-922, 2003.

[24] AF Kopp, S Schroeder, A Baumbach, A Kuettner, C Georg, B Ohnesorge, M Heuschmid, R Kuzo and CD Claussen. "Non-invasive characterization of coronary lesion morphology and composition by multislice CT: first results in comparison with intracoronary ultrasound", *Eur Radiol*, vol. 11, no. 9, pp. 1607-1611, 2001.

[25] S Schroeder, A F Kopp, A Baumbach, C Meisner, A Kuettner, C Georg, B Ohnesorge, C Herdeg, CD Claussen and KT Karsch. "Noninvasive detection and evaluation of atherosclerotic coronary plaques with multislice computed tomography", *J Am Coll Cardiol*, vol. 37, no. 5, pp. 1430-1435, 2003.

[26] RR Edelman, WJ Manning, D Burstein, and S Paulin. "Coronary arteries: breath-hold MR angiography", *Radiology*, vol. 181, no. 3, pp.641-643, 1991.

[27] WJ Manning, L Wei, and RR Edelman. "A preliminary report comparing magnetic resonance coronary angiography with conventional angiography", *N Engl J Med* 328, no. 12, pp. 828-832, 1993.

[28] DJ Pennell, J Keegan, DN Firmin, PD Gatehouse, SR Underwood, and DB Longmore. "Magnetic resonance imaging of coronary arteries: technique and preliminary results", *Br Heart J*, vol. 70, no. 4, pp. 315-326, 1993.

[29] PA Wielopolski, RJ Van Geuns, PJ De Feyter, and M Oudkerk. "Breath-hold coronary MR angiography with volume-targeted imaging", *Radiology*, vol. 209, no. 1, 209-219, 1998.

[30] JN Oshinski, L Hofland, S Mukundan, WT Dixon, WJ Parks, and RI Pettigrew. "Two-dimensional coronary MR angiography without breath holding", *Radiology*, vol. 201, no. 3, pp. 737-743, 1996.

[31] CH Meyer, BS Bob, A Macovski, and DG Nishimura. "Coronary vessel wall imaging", in *Proc. 6th Meeting of ISMRM, Sydney, Australia*, p.15, 1998.

[32] RM Botnar, M Stuber, KV Kissinger, WY Kim, E Spuentrup, and WJ Manning. "Noninvasive coronary vessel wall and plaque imaging with magnetic resonance imaging", *Circulation*, vol. 102, no. 21, pp. 2582-2587, 2000.

[33] BA Wasserman, WI Smith, HH Trout, RO Cannon, RS Balaban, and AE Arai. "Carotid Artery Atherosclerosis: In Vivo Morphologic Characterization with Gadolinium-enhanced Double-oblique MR Imaging—Initial Results1", *Radiology*, vol. 223, no. 2, pp. 566-573, 2002.

[34] KZ Abd-Elmoniem, RG Weiss and M Stuber. "Phase-sensitive black-blood coronary vessel wall imaging", *Magn Reson Med*, vol. 63, no. 4, pp. 1021-1030, 2010.

[35] R Krishnamurthy, A Pednekar, J Smink, B Cheong, and R Muthupillai. "Arrhythmia insensitive inversion recovery preparation (IR-prep) with real-time adaptive inversion delay (TI): phantom validation", *J Cardiovasc Magn Reson*, vol. 12, Suppl. 1, P168, 2010.

[36] PG Danias, MV McConnell, VC Khasgiwala, ML Chuang, RR Edelman, and WJ Manning. "Prospective navigator correction of image position for coronary MR angiography", *Radiology*, vol. 203, no. 3, pp. 733-736, 1997.

[37] M Stuber, RM Botnar, PG Danias, KV Kissinger, and WJ Manning. "Submillimeter Three-dimensional Coronary MR Angiography with Real-time Navigator Correction: Comparison of Navigator Locations1", *Radiology*, vol. 212, no. 2, pp. 579-587, 1999.

[38] Y Du, ER McVeigh, DA Bluemke, HA Silber, and T KF Foo. "A comparison of

prospective and retrospective respiratory navigator gating in 3D MR coronary angiography", *The international journal of cardiovascular imaging,* vol. 17, no. 4, pp. 287-294, 2001.

[39] MV McConell, VC Khasgiwala, BJ Savord, MH Chen, ML Chuang, RR Edelman, WJ Manning. "Prospective adaptive navigator correction for breath-hold MR coronary angiography", *Magn Reson Med,* vol. 37, no. 1, pp. 148-152, 2005.

[40] KP Pruessmann , M Weiger, P Börnert, and P Boesiger. "Advances in sensitivity encoding with arbitrary k‐space trajectories", *Magn Reson Med,* vol. 46, no. 4, pp. 638-651, 2001.

[41] DK Sodickson, and WJ Manning. "Simultaneous acquisition of spatial harmonics (SMASH): fast imaging with radiofrequency coil arrays", *Magn Reson Med,* vol. 8, no. 4, pp. 591-603, 1997.

[42] EN Yeh, CA McKenzie, MA Ohliger, and DK Sodickson. "3Parallel magnetic resonance imaging with adaptive radius in k‐space (PARS): Constrained image reconstruction using k‐space locality in radiofrequency coil encoded data", *Magn Reson Med,* vol. 53, no. 6, pp. 1383-1392, 2005.

[43] PM Jakob, MA Grisowld, RR Edelman, and DK Sodickson. "AUTO-SMASH: a self-calibrating technique for SMASH imaging", *MAGMA,* vol. 7, no. 1, pp. 42-54, 1998.

[44] MA Griswold, PM Jakob, M Nittka, JW Goldfarb, and A Haase. "Partially parallel imaging with localized sensitivities (PILS)", *Magn Reson Med,* vol. 44, no. 4, 602-609, 2000.

[45] W Chen, P Hu, and CH Meyer. "Rapid auto-calibrated parallel reconstruction

using synthetic target coil." U.S. Patent 8,026,720, issued September 27, 2011.

[46] MA Griswold, F Breuer, M Blaimer, S Kannengiesser, RM Herdemann, M Mueller, M Nittka, V Jellus, B Kiefer and PM Jakob, "Autocalibrated coil sensitivity estimation for parallel imaging", *NMR Biomed*, vol. 19, no. 3, pp. 316-324, 2006

[47] JA Bankson, SM Wright. "Generealized partially parallel imaging with spatial filters", in *Proc. 9th Meeting of ISMRM, Glasgow*, p. 1794, 2001

[48] PB Roemer, WA Edelstein, CE Hayes, SP Souza, and OM Mueller. "The NMR phased array", *Magn Reson Med*, vol. 16, no. 2, pp. 192-225, 1990.

[49] GH Golub, PC Hansen, and DP O'Leary. "Tikhonov regularization and total least squares." *SIAM J Matrix Anal and Appl*, vol. 21, no. 1, pp. 185-194, 1999.

[50] DO Walsh, AF Gmitro, and MW Marcellin. "Adaptive reconstruction of phased array MR imagery", *Magn Reson Med*, vol. 43, no. 5, pp. 682-690, 2000.

[51] T Zhang, JM Pauly, SS Vasanawala, and M Lustig. "Coil compression for accelerated imaging with Cartesian sampling", *Magn Reson Med*, vol. 69, no. 2, pp. 571-582, 2012.

[52] F Huang, S Vijayakumar, Y Li, S Hertel, and GR Duensing. "A software channel compression technique for faster reconstruction with many channels." *Magn Reson Imaging*, vol. 26, no. 1, pp. 133-141, 2008.

[53] PJ Beatty, W Sun, and AC Brau. "Direct virtual coil (DVC) reconstruction for data-driven parallel imaging", in *Proc. 16th Ann. Meeting of ISMRM, Toronto, Canada*, p. 8, 2008.

[54] PJ Beatty, AC Brau, S Chang, SM Joshi, CR Michelich, E Bayram, TE Nelson, RJ Herfkens, and JH Brittain. "A method for autocalibrating 2-D accelerated volumetric

parallel imaging with clinically practical reconstruction times", in *Proc. 15th Ann. Meeting of ISMRM, Berlin, Germany*, p.1749, 2007.

[55] PJ Beatty, JY Cheng, A Shankaranarayanan, A Madhuranthakam, H Yu, E Bayram, S Chang, JH Brattain. "Feasibility of direct virtual coil (DVC) reconstruction for 3-D imaging", in *Proc. 17th Ann. Meeting of ISMRM, Honolulu, USA*, p.2727, 2009.

[56] K Wang, PJ Beatty, SK Nagle, SB Reeder, JH Holmes, MS Rahimi, LC Bell, FR Korosec, and JH Brittain. "Application of direct virtual coil to dynamic contrast‐enhanced MRI and MR angiography with data‐driven parallel imaging", *Magn Reson Med*, 2013(early review).

[57] PJ Beatty, S Chang, E Bayram, A Madhuranthakam, H Yu, S.B Reeder, JH Brittain, "Virtual Coil Phase Determination using Region Growing: Description and Application to Direct Virtual Coil Parallel Imaging Reconstruction", In *Proc. 18th Ann. Meeting of ISMRM, Stockholm, Sweden.* p.7048, 2010.

[58] T Schiwietz , T Chang, P Speier, and R Westermann. "MR image reconstruction using the GPU", *Proc. SPIE* 6142, pp. 1279-1290, 2006.

[59] DS Smith, JC Gore, EB Welch. "Accelerating Compressed Sensing MRI Reconstruction with GPU Computing", in *Proc. 19th Ann. Meeting of ISMRM, Montreal, Canada*, p.2546, 2011.

[60] S Roujol, B Denis de Senneville, E Vahala, T Sangild Sørensen, C Moonen, and M Ries. "Online real‐time reconstruction of adaptive TSENSE with commodity CPU/GPU hardware", *Magn Reson Med*, vol. 62, no. 6, pp. 1658-1664, 2009.

[61] M Lustig, D Donoho, and JM Pauly. "Sparse MRI: The application of compressed

sensing for rapid MR imaging", *Magn Reson Med*, vol. 58, no. 6, 1182-1195, 2007.

[62] RM Heidemann, MA Griswold, N Seiberlich, G Krüger, SAR Kannengiesser, B Kiefer, G Wiggins, LL Wald, and PM Jakob. "Direct parallel image reconstructions for spiral trajectories using GRAPPA", *Magn Reson Med*, vol. 56, no. 2, pp. 317-326, 2006.

[63] N Seiberlich, FA Breuer, M Blaimer, K Barkauskas, PM Jakob, and MA Griswold. "Non‐Cartesian data reconstruction using GRAPPA operator gridding (GROG)", *Magn Reson Med*, vol. 58, no. 6, pp. 1257-1265, 2007.

[64] P Hu, CH Meyer. "Spiral PILS Coronary Artery Imaging", in *Proc. 15th Ann. Meeting of ISMRM, Seattle, USA*, p.371, 2006.

[65] P Hu, CH Meyer. "BOSCO: Parallel image reconstruction based on successive convolution operations", in *Proc.15th Ann. Meeting of ISMRM, Seattle, USA*, p.10, 2006.

[66] M Bydder, and MD Robson. "Partial Fourier partially parallel imaging", *Magn Reson Med*, vol. 53, no. 6, pp. 1393-1401, 2005.

[67] JD Willig-Onwuachi, EN Yeh, AKGrant, MA Ohliger, CA McKenzie, and DK Sodickson. "Phase-constrained parallel MR image reconstruction using symmetry to increase acceleration and improve image quality", in *Proc.11th Ann. Meeting of ISMRM, Toronto, Canada*, p. 19, 2003.

[68] VL Yarnykh, and C Yuan. "Multislice double inversion‐recovery black‐blood imaging with simultaneous slice reinversion", *J Magn Reson Imaging*, vol. 17, no. 4, pp. 478-483, 2003.

[69] J Wang, VL Yarnykh, and C Yuan. "Enhanced image quality in black‐blood MRI

using the improved motion‐sensitized driven‐equilibrium (iMSDE) sequence", *J Magn Reson Imaging,* vol. 31, no. 5, pp. 1256-1263, 2010.

[70] S Gerretsen, J Wang, JH Maki, C Jaarsma, D Herzka, B Chu, VV Yarnykh, C Yuan, and TV Leiner. "Reproducible coronary vessel wall imaging at 3T using improved motion sensitized driven equilibrium (IMSDE)", in *Proc.18th Ann. Meeting of ISMRM, Stockholm, Sweden*, p.3848, 2010.

[71] L Li, K Miller, J Near and P Jezzard. "Steady-State Motion-Induced Contrast Using DANTE Pulse Trains: A Novel Approach to Black Blood Imaging", in *Proc. 20th Ann. Meeting of ISMRM, Melbourne, Australia*, p.323, 2012.

[72] GJ Stanisz, EE Odrobina, J Pun, M Escaravage, SJ Graham, MJ Bronskill, and R M Henkelman. "T1, T2 relaxation and magnetization transfer in tissue at 3T", *Magn Reson Med*, vol. 54, no. 3, pp. 507-512, 2005.

[73] W Chen, CT Sica, and CH Meyer. "Fast conjugate phase image reconstruction based on a Chebyshev approximation to correct for B0 field inhomogeneity and concomitant gradients", *Magn Reson Med*, vol. 60, no. 5, pp. 1104-1111, 2008.

[74] D Elad, S Einav. "Standard Handbook of Biomedical Engineering and Design" Chapter3. Fig.3.15.

[75] DL Parker, KC Goodrich, M Masiker, JS Tsuruda, and GL Katzman. "Improved efficiency in double‐inversion fast spin‐echo imaging", *Magn Reson Med*, vol. 47, no. 5, pp. 1017-1021, 2002.

[76] HK Song, AC Wright, RL Wolf, and FW Wehrli. "Multislice double inversion pulse sequence for efficient black‐blood MRI", *Magn Reson Med*, vol. 47, no. 3, pp. 616-620, 2002.

[77] RM Botnar, WY Kim, P Börnert, M Stuber, E Spuentrup, and WJ Manning. "3D coronary vessel wall imaging utilizing a local inversion technique with spiral image acquisition", *Magn Reson Med*, vol. 46, no. 5, pp. 848-854, 2001.

[78] AM Taylor, P Jhooti, F Wiesmann, J Keegan, DN Firmin, and DJ Pennell. "MR navigator‐echo monitoring of temporal changes in diaphragm position: Implications for MR coronary angiography", *J Magn Reson Imaging*, vol. 7, no. 4, pp. 629-636, 1997.

[79] Y He, Z Zhang, Q Dai, J An, I Jin, R Jerecic, and D Li, "Accuracy of maginteic resonance imaging to identify the coronary artery plaque: a comparative with intravascular ultrasound", in *Proc.19th Ann. Meeting of ISMRM, Montreal, Canada,* p.1275, 2011.

[80] AN Priest, PM Bansmann, MG Kaul, A Stork, and G Adam. "Magnetic resonance imaging of the coronary vessel wall at 3 T using an obliquely oriented reinversion slab with adiabatic pulses", *Magn Reson Med*, vol. 54, no. 5, pp. 1115-1122, 2005.

[81] SA Peel, T Hussain, T Schaeffter, GF Greil, MW Lagemaat, and RM Botnar. "Cross‐sectional and In‐plane coronary vessel wall imaging using a local inversion prepulse and spiral read‐out: A comparison between 1.5 and 3 tesla", *J Magn Reson Imaging*, vol. 35, no. 4, pp. 969-975, 2012.

[82] AD Scott, J Keegan, and DN Firmin. "High‐resolution 3D coronary vessel wall imaging with near 100% respiratory efficiency using epicardial fat tracking: Reproducibility and comparison with standard methods", *J Magn Reson Imaging,* vol. 33, no. 1, pp. 77-86, 2011.

[83] T Niendorf, CJ Hardy, RO Giaquinto, P Gross, HE Cline, Y Zhu, G Kenwood et al.

"Toward single breath‐hold whole‐heart coverage coronary MRA using highly accelerated parallel imaging with a 32‐channel MR system." *Magn Reson Med,* vol. 56, no. 1, pp. 167-176, 2006.

[84] A Macovski. "Volumetric NMR imaging with time‐varying gradients", *Magn Reson Med*, vol. 2, no. 1, pp. 29-40, 1985.

[85] WY Kim, M Stuber, P Börnert, KV Kissinger, WJ Manning, and RM Botnar. "Three-dimensional black-blood cardiac magnetic resonance coronary vessel wall imaging detects positive arterial remodeling in patients with nonsignificant coronary artery disease", *Circulation*, vol. 106, no. 3, pp. 296-299, 2002.

[86] RM Botnar, M Stuber, R Lamerichs, J Smink, SE Fischer, P Harvey, and WJ Manning. "Initial experiences with in vivo right coronary artery human MR vessel wall imaging at 3 tesla", *J Cardiovas Magn Reson*, vol. 5, no. 4, pp. 589-594, 2003.

[87] S Fielden, CH Meyer, JP Mugler. "Variable flip angle turbo spin echo sequence utilizing spiral acquisitions", in *Proc.19th Ann. Meeting of ISMRM, Montreal, Canada*, p.2820, 2011.

[88] N Seiberlich, G Lee, P Ehses, JL Duerk, R Gilkeson, M Griswold, "Improved temporal resolution in cardiac imaging using through-time spiral GRAPPA", *Magn Reson Med*, vol. 66, no. 6, pp. 1682-1688, 2011.